

Alma Mater Studiorum – Università di Bologna

DOTTORATO DI RICERCA IN

Scienze Chimiche

Ciclo XXIII

Settore scientifico-disciplinare di afferenza: CHIM/02

**Advanced lithium and lithium-ion
rechargeable batteries for automotive
applications**

Presentata da **Libero Damen**

Coordinatore Dottorato

Prof. Giuliano Longoni

Relatore

Prof. Marina Mastragostino

Esame finale anno 2011

Abstract

The worldwide demand for a clean and low-fuel-consuming transport promotes the development of safe, high energy and power electrochemical storage and conversion systems. Lithium-ion batteries (LIBs) are considered today the best technology for this application as demonstrated by the recent interest of automotive industry in hybrid (HEV) and electric vehicles (EV) based on LIBs. This thesis work, starting from the synthesis and characterization of electrode materials and the use of non-conventional electrolytes, demonstrates that LIBs with novel and safe electrolytes and electrode materials meet the targets of specific energy and power established by U.S.A. Department of Energy (DOE) for automotive application in HEV and EV.

In chapter 2 is reported the origin of all chemicals used, the description of the instruments used for synthesis and chemical-physical characterizations, the electrodes preparation, the batteries configuration and the electrochemical characterization procedure of electrodes and batteries.

Since the electrolyte is the main critical point of a battery, in particular in large-format modules, in chapter 3 we focused on the characterization of innovative and safe electrolytes based on ionic liquids (characterized by high boiling/decomposition points, thermal and electrochemical stability and appreciable conductivity) and mixtures of ionic liquid with conventional electrolyte.

In chapter 4 is discussed the microwave accelerated sol-gel synthesis of the carbon-coated lithium iron phosphate ($\text{LiFePO}_4\text{-C}$), an excellent cathode material for LIBs thanks to its intrinsic safety and tolerance to abusive conditions, which showed excellent electrochemical performance in terms of specific capacity and stability.

In chapter 5 are presented the chemical-physical and electrochemical characterizations of graphite and titanium-based anode materials in different electrolytes. We also characterized a new anodic material, amorphous SnCo alloy, synthesized with a nanowire morphology that showed to strongly enhance the electrochemical stability of the material during galvanostatic full charge/discharge cycling.

Finally, in chapter 6, are reported different types of batteries, assembled using the $\text{LiFePO}_4\text{-C}$ cathode material, different anode materials and electrolytes, characterized by deep galvanostatic charge/discharge cycles at different C-rates and by test procedures of

the DOE protocol for evaluating pulse power capability and available energy. First, we tested a battery with the innovative cathode material $\text{LiFePO}_4\text{-C}$ and conventional graphite anode and carbonate-based electrolyte (EC DMC LiPF_6 1M) that demonstrated to surpass easily the target for power-assist HEV application. Given that the big concern of conventional lithium-ion batteries is the flammability of highly volatile organic carbonate-based electrolytes, we made safe batteries with electrolytes based on ionic liquid (IL). In order to use graphite anode in IL electrolyte we added to the IL 10% w/w of vinylene carbonate (VC) that produces a stable SEI (solid electrolyte interphase) and prevents the graphite exfoliation phenomenon. Then we assembled batteries with $\text{LiFePO}_4\text{-C}$ cathode, graphite anode and $\text{PYR}_{14}\text{TFSI}$ 0.4m LiTFSI with 10% w/w of VC that overcame the DOE targets for HEV application and were stable for over 275 cycles. We also assembled and characterized “high safety” batteries with electrolytes based on pure IL, $\text{PYR}_{14}\text{TFSI}$ with 0.4m LiTFSI as lithium salt, and on mixture of this IL and standard electrolyte ($\text{PYR}_{14}\text{TFSI}$ 50% w/w and EC DMC LiPF_6 50% w/w), using titanium-based anodes (TiO_2 and $\text{Li}_4\text{Ti}_5\text{O}_{12}$) that are commonly considered safer than graphite in abusive conditions. The batteries bearing the pure ionic liquid did not satisfy the targets for HEV application, but the batteries with $\text{Li}_4\text{Ti}_5\text{O}_{12}$ anode and 50-50 mixture electrolyte were able to surpass the targets. We also assembled and characterized a lithium battery (with lithium metal anode) with a polymeric electrolyte based on poly-ethylenoxide ($\text{PEO}_{20}\text{-LiCF}_3\text{SO}_3\text{+10\%ZrO}_2$), which satisfied the targets for EV application and showed a very impressive cycling stability.

In conclusion, we developed three lithium-ion batteries of different chemistries that demonstrated to be suitable for application in power-assist hybrid vehicles: graphite/EC DMC LiPF_6 / $\text{LiFePO}_4\text{-C}$, graphite/ $\text{PYR}_{14}\text{TFSI}$ 0.4m LiTFSI with 10% VC/ $\text{LiFePO}_4\text{-C}$ and $\text{Li}_4\text{Ti}_5\text{O}_{12}$ / $\text{PYR}_{14}\text{TFSI}$ 50%-EC DMC LiPF_6 50%/LiFePO₄-C. We also demonstrated that an all solid-state polymer lithium battery as $\text{Li/PEO}_{20}\text{-LiCF}_3\text{SO}_3\text{+10\%ZrO}_2$ / $\text{LiFePO}_4\text{-C}$ is suitable for application on electric vehicles. Furthermore we developed a promising anodic material alternative to the graphite, based on SnCo amorphous alloy.

Table of Contents

Chapter 1. Introduction

1.1	Lithium and lithium-ion batteries	p. 1
1.2	Active materials for the positive electrode	p. 5
1.3	Active materials for the negative electrode	p. 8
1.4	Electrolytes	p. 13
1.5	Safety issues	p. 16
1.6	Electric and hybrid electric vehicles	p. 18
1.7	Objective of the thesis	p. 20
1.8	References	p. 21

Chapter 2. Chemicals, Techniques and Analyses

2.1.	Chemicals	p. 23
2.2.	Instruments for synthesis and chemical-physical characterizations	p. 24
2.3.	Electrode preparation and cell configuration	p. 24
2.4.	Electrochemical characterization of electrodes and batteries	p. 27
2.5.	References	p. 29

Chapter 3. Electrolytes

3.1	Chemical, physical and electrochemical properties of EC DMC-LiPF ₆ 1M	p. 31
3.2	Chemical, physical and electrochemical properties of the ionic liquid-based electrolyte PYR ₁₄ TFSI-LiTFSI 0.4m	p. 32
3.3	Chemical, physical and Electrochemical properties of PYR ₁₄ TFSI/ EC DMC-LiPF ₆ 50%/50 wt.% mixture	p. 34
3.4	Electrochemical properties of PYR ₁₄ TFSI 0.4m LiTFSI with 10% VC	p. 35
3.5	Electrochemical properties of PEO ₂₀ -LiCF ₃ SO ₃ +10%ZrO ₂ polymer electrolyte	p. 36
3.6	Conclusions	p. 36
3.7	References	p. 37

Chapter 4. Cathode material

4.1	LiFePO ₄	p. 39
4.2	Synthesis	p. 39
4.3	Chemical-physical properties	p. 40
4.4	Electrochemical characterization	p. 41
4.5	Conclusions	p. 44
4.6	References	p. 45

Chapter 5. Anode materials

5.1	Graphite	p. 47
5.1.1	Chemical-physical properties	p. 47
5.1.2	Electrochemical characterization	p. 48
5.2	Titanium-based materials	p. 53
5.2.1	TiO ₂	p. 53
5.2.2	Chemical-physical properties	p. 53
5.2.3	Electrochemical characterization	p. 53
5.2.4	Li ₄ Ti ₅ O ₁₂	p. 57
5.2.5	Chemical-physical properties	p. 57
5.2.6	Electrochemical characterization	p. 58
5.3	SnCo	p. 63
5.3.1	Synthesis	p. 63
5.3.2	Chemical-physical properties	p. 64
5.3.3	Electrochemical characterization	p. 66
5.4	Conclusions	p. 69
5.5	References	p. 70

Chapter 6. Battery tests for HEV and EV application

6.1	Lithium-ion batteries for application in HEV	p. 73+2
6.1.1	Graphite/EC DMC-LiPF ₆ /LiFePO ₄ -C	p. 73
6.1.2	Graphite/PYR ₁₄ TFSI 0.4m LiTFSI with 10% VC/LiFePO ₄ -C	p. 79
6.1.3	TiO ₂ /PYR ₁₄ TFSI 0.4m LiTFSI/LiFePO ₄ -C	p. 86
6.1.4	Li ₄ Ti ₅ O ₁₂ / PYR ₁₄ TFSI 0.4m LiTFSI/LiFePO ₄ -C	p. 90

6.1.5	TiO ₂ / PYR ₁₄ TFSI-EC DMC LiPF ₆ 50:50/ LiFePO ₄ -C	p. 94
6.1.6	Li ₄ Ti ₅ O ₁₂ / PYR ₁₄ TFSI-EC DMC LiPF ₆ 50:50w/ LiFePO ₄ -C	p. 97
6.2	Lithium battery for application in EV	p. 102
6.2.1	Li/PEO ₂₀ -LiCF ₃ SO ₃ +10%ZrO ₂ /LiFePO ₄ /C lithium polymer battery	p. 102
6.3	Conclusions	p. 108
6.4	References	p. 108
Chapter 7. Conclusions		p. 109
Acknowledgements		p. 111
List of Presentation to Conferences		p. 113
List of Publications		p. 115

Chapter 1

Introduction

1.1. Lithium and lithium-ion batteries

The modern world would not be the same without the development of lithium batteries and their evolution in lithium-ion batteries. It is easy to understand if we consider that they are the power source of choice for portable electronic devices, especially, implantable medical devices, wireless telephones and laptop computers.

The reason for using a battery technology based on lithium metal as anode depends initially on the fact that Li is the most electropositive (-3.04 V vs. SHE) as well as the lightest (density=0.53 g cm⁻³) metal, delivering the impressive theoretical specific capacity of 3860 mAh g⁻¹, thus facilitating the production of storage systems with high energy density (Figure 1.1). Commercial primary lithium batteries, formerly developed under the auspices of NASA and the Department of Defense in the USA, were introduced in the early 1970s. Ten years after batteries with capacities ranging from 5 mAh to many thousands of Ah were widely available. The first commercial primary battery, fabricated by Panasonic (Matsushita Electric Ind. Corp.), was based on a carbon mono-fluoride cathode material. Today the most common type of primary lithium cell for consumer applications uses metallic lithium as anode and manganese dioxide as cathode, with a salt of lithium dissolved in an organic solvent as electrolyte. Depending on the design and chemical compounds used, lithium cells can produce voltages from 1.5 V to about 3.7 V, twice the voltage of an ordinary zinc-carbon battery or alkaline cell. Long-life implantable electronic medical devices utilize lithium batteries, in particular lithium-iodide technology (designed to last 15 or more years) for artificial pacemakers, and Li/Ag₂V₄O₁₁ technology for implantable defibrillators^{1,2}. Primary cells technologies also include lithium/thionyl chloride (Li/SOCl₂), lithium/sulfuryl chloride (Li/SO₂Cl₂) and lithium/sulphur dioxide (Li/SO₂) chemistries which are based on liquid cathodes to obtain higher energy densities, long-life and low temperature operation. Lithium batteries can be used in place of ordinary alkaline cells in many devices, such as clocks and cameras and although they are more

expensive, lithium cells provide much longer life, thereby minimizing battery replacement.

By far the most important development in the field of lithium batteries in the past 25 years has been the successful realization and commercialization of rechargeable (secondary) cells.

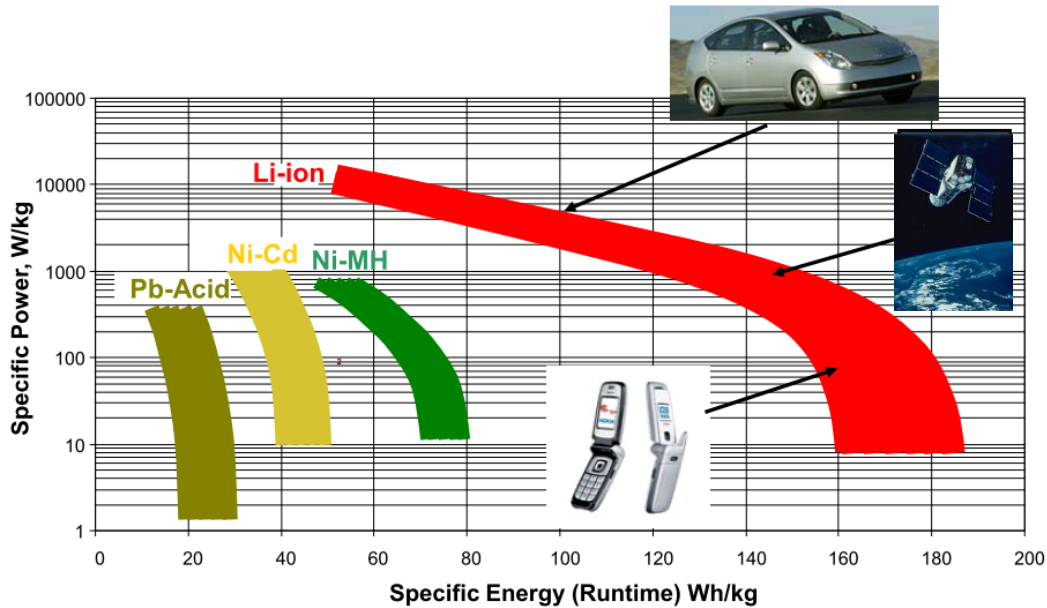


Figure 1.1. Comparison of the different battery technologies in terms of specific power and specific energy.

Initially, materials such as layered TiS or MoS₂ were developed as positive materials for practical secondary cells by Exxon, Moli Energy and others. While lithium can be plated with high efficiency, there are significant problems in producing practical secondary cells with lithium metal anode, because of the very high reactivity of the newly plated lithium with components of the electrolyte. This phenomenon, which is responsible for the passivation and excellent shelf life of primary lithium anodes, causes a number of undesirable effects in rechargeable cell. First of all, some of the plated lithium grains may be lost due to the electronic insulation from the rest of the electrode, thus reducing capacity. The uniformity of the deposit may become poor, leading to dendrite formation and short circuits. Finally, since the passivation reaction is highly exothermic, the cell may overheat and in extreme cases, given the low melting point of lithium, thermal runaway

may occur. To circumvent the safety issues surrounding the use of Li metal, several alternative approaches were pursued in which either the electrolyte or the negative electrode were modified.

The first approach^{1,3} involved replacing the liquid electrolyte by a dry polymer electrolyte, leading to the so-called lithium solid polymer electrolyte batteries, where the electrolyte consists of a coordinating macromolecular host such as poly-ethyleneoxide (PEO) in which an appropriate salt had been dissolved. These “immobile solvents” became the basis of the lithium polymer battery development in the late ’70s with the lithium-vanadium oxide cell by Hydro-Quebec (HQ) and then by 3M/HQ (Figure 1.2). Unfortunately, this technology is restricted to large systems (electric traction or backup power) and not to portable devices, as it requires temperatures up to 80°C to achieve an appreciable electrolyte conductivity.

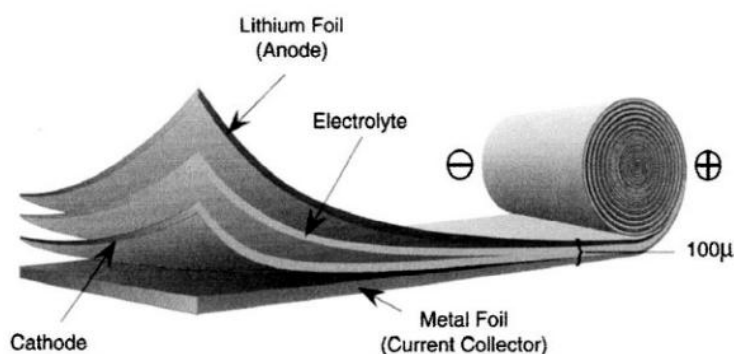


Figure 1.2. Construction of the 3M/Hydroquebec lithium polymer battery cell

The second approach involved replacing lithium by a lithium insertion host, with a significantly lower standard reduction potential than that of the hosts used for the positive electrode, which can undergo many deep charge/discharge cycles with stable capacity. The basic function of lithium-ion batteries is given by the combination of two lithium insertion materials. More specifically, lithium ions are inserted into/extracted from a solid matrix without the destruction of core structures (so called topotactic reactions) in positive and negative electrodes during charge and discharge. Electrons are simultaneously extracted from one electrode and injected into another electrode during which materials are oxidized or reduced in negative and positive electrodes, while lithium ions shuttle between negative and positive electrodes. The concept was first demonstrated in the laboratory by Murphy et

al.^{1.4} and then by Scrosati et al.^{1.5} and led, at the end of the 1980s and early 1990s, to the so-called lithium-ion technology.

Many materials were proposed as anodes, including transition metal dichalcogenides and lithium alloys, but the most successful practical electrodes which have emerged so far are based on carbon, either graphite or non-graphitic disordered phases. Lithium intercalation occurs between carbon planes up to a maximum ratio of one lithium to six carbon atoms, giving a maximum theoretical capacity of 372 mAh g⁻¹. It is found that excess charge is always consumed in the first charge due to a corrosion process which results in the formation of an SEI (Solid Electrolyte Interface) layer. Because of the presence of lithium in its ionic rather than metallic state, Li-ion cells resolve the dendrite problem and are, theoretically, inherently safer than Li-metal cells.

To compensate for the increase in potential of the negative electrode, high-potential insertion compounds are needed for the positive electrode, and emphasis shifted from the layered-type transition-metal disulphides to layered-or three-dimensional-type transition-metal oxides^{1.6}: metal oxides are more oxidizing than disulphides (they have higher insertion potential) owing to the more pronounced ionic character of 'M–O' bonds compared with 'M–S' bonds.

Finally, in 1991 Sony^{1.7} started the commercialization of new C/LiCoO₂ batteries, called lithium-ion batteries. This type of Li-ion cell (Figure 1.3), having a potential exceeding 3.6 V (three times that of alkaline systems), gravimetric energy densities as high as 120-150 Wh kg⁻¹ (two to three times those of usual Ni–Cd batteries) and an energy density of over 500 Wh dm⁻³, is found in most of today's high-performance portable electronic devices.

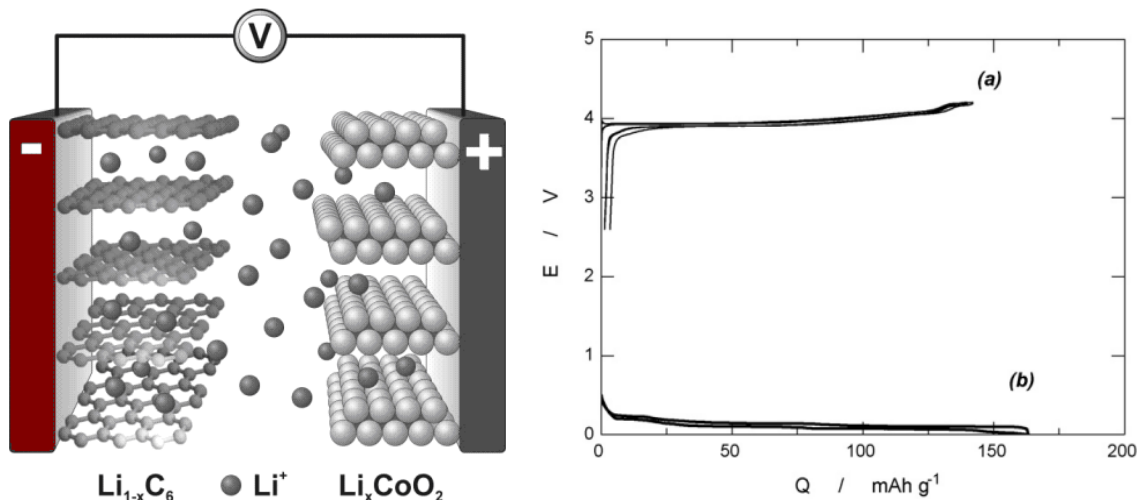


Figure 1.3. Left: scheme of a common lithium ion battery. Right: charge and discharge curves of (a) LiCoO_2 and (b) graphite single electrodes vs. lithium. Combination of LiCoO_2 and graphite gives a lithium-ion battery. Specific capacity of graphite is given in 1/2 reduction.

1.2 Active materials for the positive electrode

The selection of the positive electrode active material depends on whether we are dealing with rechargeable Li metal or Li-ion batteries. For rechargeable Li batteries, owing to the use of metallic lithium as the negative electrode, the positive electrode does not need to be lithiated before cell assembly. On the contrary, for Li-ion batteries, because the carbon negative electrode has no lithium inserted, the positive one must act as a source of lithium ions, thus requiring use of air-stable Li-based intercalation compounds to make possible the cell assembly. Li rechargeable batteries generally utilize vanadium oxide cathode while LiCoO_2 is the most widely used cathode in commercial Li-ion batteries, but many alternative candidates have been proposed.

LiCoO_2 assumes the $\alpha\text{-NaFeO}_2$ structure^{1,8} (Figure 1.4a) with consecutive alternating CoO_2 and Li layers, accordingly Co^{3+} stay in the 3a site, and Li^+ in the 3b site in the R3m ccp packed O^{2-} lattice. Both Co and Li have octahedral coordination. The Li extraction of Li_xCoO_2 starts with an expansion of the interlayer c axis as a result of electrostatic repulsion of the oxygen layers when $x \geq 0.5$; then, at $x \approx 0.5$ there is a hexagonal-monoclinic transformation that represents an order-disorder transition; finally, a transformation of the O3 LiCoO_2 phase (close-packed oxygen layers with an ABCABC

stacking sequence) into the O1 Li_xCoO_2 phase (ABAB stacking sequence) occurs at $x \approx 0.05$. Even if almost all of the Li can be extracted to give a theoretical capacity of 274 mAh g^{-1} , only half of the capacity is practically reversible for insertion/deinsertion ($\leq 4.2 \text{ V vs. Li/Li}^+$). Capacity fading is severe upon extraction of more than 0.7 Li because of loss of oxygen (resulting from decreased stability of lithium poor phases), electrolyte decomposition, and the problem of cobalt dissolution in typical electrolytes.

The spinel LiMn_2O_4 (Figure 1.4b) is an interesting cathode material, because the more chemically stable $\text{Mn}^{3+}/\text{Mn}^{4+}$ couple offers excellent safety and high power capability owing to the 3D lattice. Furthermore, Mn is inexpensive and environmentally benign. LiMn_2O_4 exhibits an operating voltage of 4.1 V (Figure 1.5a). The Li^+ ion occupies the tetrahedral 8d site in the cubic-closed packed O^{2-} lattice, and Mn^{3+} resides in the 16c octahedral site. Spinel structures have been the subject of exhaustive studies from the 1990s which have highlighted the unusually facile Li^+ ion mobility in the framework, and the ability of the lattice to undergo substitution to enhance electrochemical properties. Like LiCoO_2 , LiMn_2O_4 is now well-established commercial lithium-ion battery cathode material. Spinel LiMn_2O_4 cathodes have the drawback of a significant capacity fade, especially at temperatures $\geq 50^\circ\text{C}$: several mechanisms such as Jahn-Teller distortion of Mn^{3+} , manganese dissolution into the electrolyte, loss of crystallinity, oxygen loss upon cycling have all been suggested to be the source of capacity fade. Among them, Mn^{2+} dissolution is almost universally considered to be the predominant cause.

$\text{LiCo}_{1/3}\text{Ni}_{1/3}\text{Mn}_{1/3}\text{O}_2$ is another very promising alternative cathode. The metals Co, Ni, and Mn can all be accommodated in the layered metal oxide structure giving different compositions $\text{Li}[\text{Co}_x\text{Ni}_y\text{Mn}_z]\text{O}_2$ ($x+y+z=1$) but the most intriguing possesses the same structure as LiCoO_2 , with Ni, Co, and Mn assuming oxidation states of 2+, 3+ and 4+ respectively^{1,9}, with only 1-6% of cation disorder. In addition, $\text{Li}_{1-x}\text{Co}_{1/3}\text{Ni}_{1/3}\text{Mn}_{1/3}\text{O}_2$ exhibits only a 1-2% volume change in the range of $0 < x < 0.7$. The low amount of cation disorder combined with the small volume change contribute to its excellent electrochemical performance (Figure 1.5b).

LiFePO_4 is the cathode material that is attracting much attention at present. The structure of LiFePO_4 (Figure 1.4c) which belongs to the family of olivines, consists of a distorted hexagonal close-packed (hcp) oxygen framework with 1/8 of the tetrahedral holes occupied by P, and 1/2 of the octahedral holes occupied by Li and Fe. LiFePO_4 crystallizes

in space group Pnma. Layers of FeO_6 octahedra are corner-shared in the bc plane and linear chains of LiO_6 octahedra are edge-shared in a direction parallel to the b-axis. These chains are connected by edge and corner shared phosphate tetrahedra, building a stable three-dimensional structure. It can reversibly intercalate Li at the voltage of 3.45 V (Figure 1.5c) gravimetric capacity of 170 mAh g^{-1} . Unlike the conductive metal oxides, the electronic conductivity of LiFePO_4 is only $1 \cdot 10^{-9} \text{ S cm}^{-1}$ at room temperature, limiting electrochemical performance because electrons cannot easily transport through the material. Coating LiFePO_4 particles with carbon seems to be the most promising route to improve the conductivity.

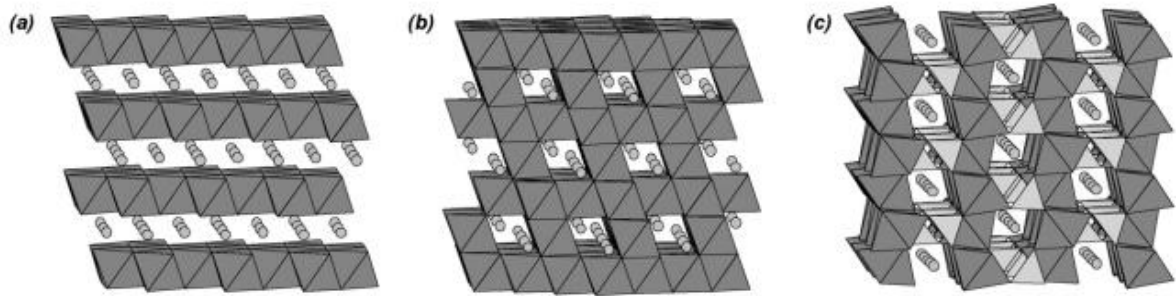


Figure 1.4. Schematic illustrations of the crystal structures of (a) LiCoO_2 (layered structure), (b) LiMn_2O_4 (spinel structure) and (c) LiFePO_4 (olivine structure). Structures are illustrated with MO_6 -octahedra (M:transition metal) and PO_4 -tetrahedra.

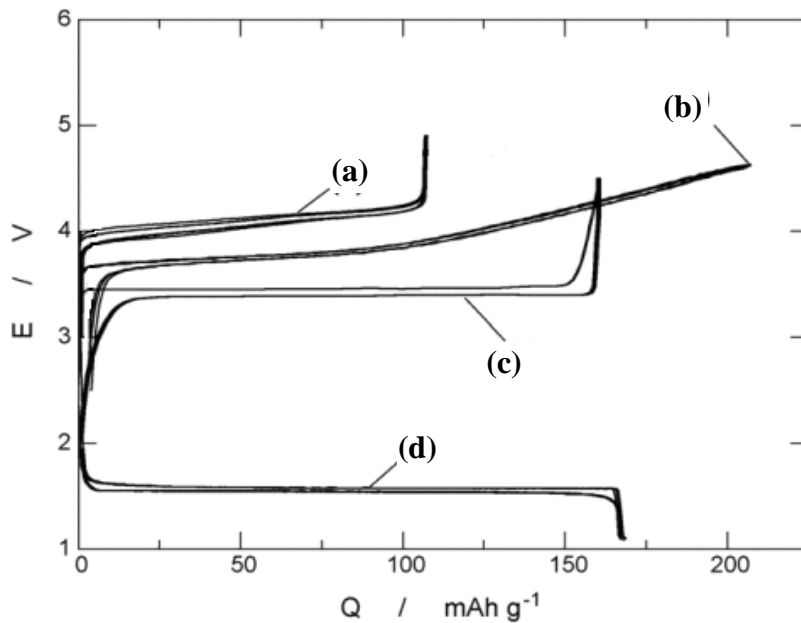


Figure 1.5. Charge and discharge curves of (a) LiMn_2O_4 , (b) $\text{LiCo}_{1/3}\text{Ni}_{1/3}\text{Mn}_{1/3}\text{O}_2$, (c) LiFePO_4 , and (d) $\text{Li}_4\text{Ti}_5\text{O}_{12}$ examined in lithium cells.

1.3 Active Materials for the negative electrode

Graphite is the most used active material for the anode production, due to its unique characteristics in terms of capacity, cyclability and low voltage of the lithium insertion/deinsertion process. Graphite is a layered compound formed by graphene sheets^{1,10}: during charge lithium ions are progressively inserted between single graphite layers up to LiC_6 , which corresponds to the maximum theoretical specific charge of 372 mAh g^{-1} , according with the following reversible reaction:



Carbons that can intercalate lithium reversibly are catalogued as graphitic and non-graphitic (disordered). Graphitic carbons are carbonaceous materials with the layered structure of the graphite, but usually with a number of structural defects. Graphite has a layered lattice structure with a stacking order of graphene layers, either the prevalent AB (hexagonal graphite) or the less common ABC (rhombohedral graphite). Due to the small transformation energy of AB into ABC stacking (and vice versa), perfectly stacked graphite crystals are not readily available. The carbon atoms adopt a C-C distance of 1.421 \AA and the layer planes are stacked parallel to each other at a distance of 3.354 \AA (Figure 1.6).

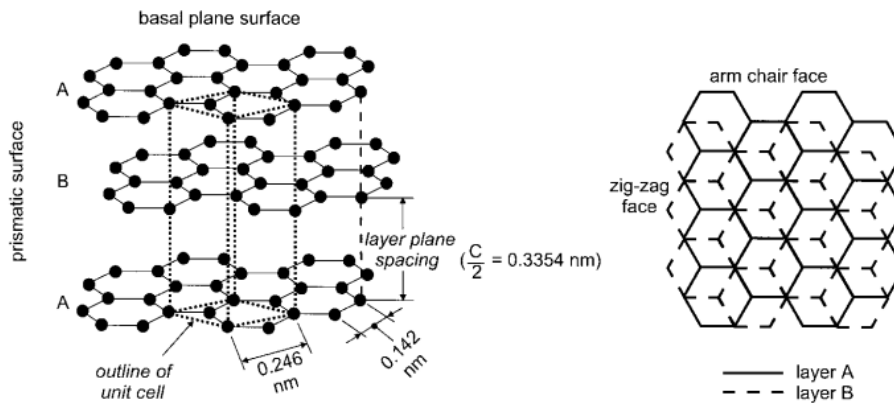


Figure 1.6. Left: schematic drawing of the crystal structure of hexagonal graphite, showing the AB layer stacking sequence and the unit cell. Right: view perpendicular to the basal plane of hexagonal graphite; prismatic surfaces can be subdivided into arm-chair and zig-zag faces.

Non-graphitic carbonaceous materials consist of carbon atoms that are mainly arranged in a planar hexagonal network but without far-reaching crystallographic order in the c-

direction. The structure of those carbons is characterized by amorphous areas embedding and crosslinking more graphitic ones.

The anisotropy of the graphite crystal is reflected in its chemical behavior: the intercalation reaction occurs only at the end of basal planes of the crystal which are arm-chair and zig-zag faces, while through the basal planes, intercalation is possible at defect sites only. During intercalation into graphite the stacking order of the graphene layers shifts to AA. Thus, two neighboring graphene layers in LiC_6 directly face each other (Figure 1.7a). As a result of lithium intercalation the interlayer distance between the graphene layers increases moderately (10% has been calculated for LiC_6). In LiC_6 the lithium is distributed in-plane in such a manner that it avoids the occupation of the nearest neighbor sites (Figure 1.7b).

In theory, Li^+ intercalation into carbons is fully reversible but in practice the charge consumed in the first cycle significantly exceeds the theoretical specific capacity and in the subsequent deintercalation of Li^+ recovers only about 80–95% of this capacity. In the following cycles, however, the discharge/charge efficiency is close to 100%. The excess charge consumed in the first cycle is attributed to SEI formation. Like metallic lithium, lithium/carbon intercalation compounds are thermodynamically unstable in all known electrolytes, and therefore the surfaces, which are exposed to the electrolyte, have to be kinetically protected by SEI films. In contrast to the spontaneous film formation on metallic Li upon contact with electrolyte, the film formation on Li_xC_6 surfaces takes place as a charge-consuming side reaction in the first reduction of the carbon host material.

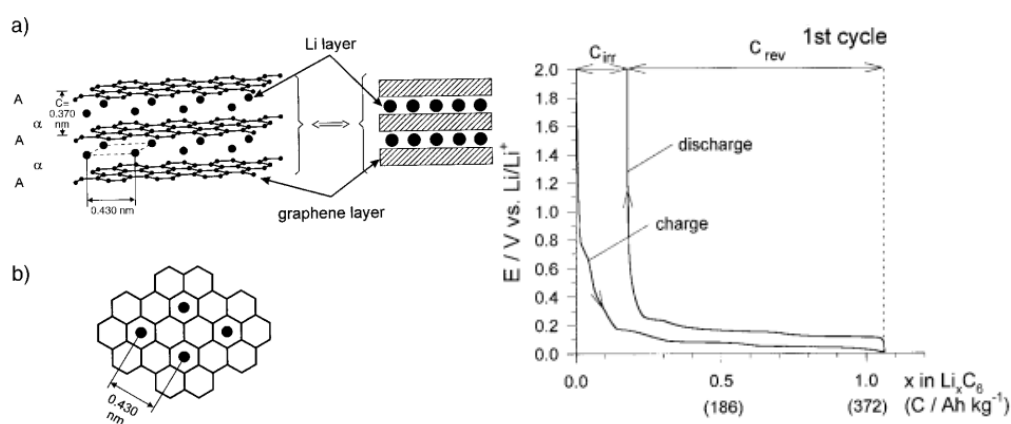


Figure 1.7. Left: (a) schematic drawing showing the AA layer stacking sequence and the $\alpha\alpha$ interlayer ordering of the intercalated lithium; (b) view perpendicular to the basal plane of LiC_6 . Right: constant current charge/discharge curve of the first cycle of a commercial graphite in organic electrolyte (C_{irr} is the irreversible specific charge, C_{rev} the reversible specific charge).

Anodic materials based on titanium oxides are promising candidates as alternative materials to carbonaceous anodes due to their advantages in terms of safety, cheapness and toxicity. The relatively high potential of Li intercalation/deintercalation (>1 V) makes the Ti-based electrodes intrinsically safer compared to graphite, which has an operating voltage close to Li electroplating potential and thus raises concerns over its safety. Two materials have been widely investigated: TiO_2 ^{1,11} and its derivative $\text{Li}_4\text{Ti}_5\text{O}_{12}$ ^{1,12}.

TiO_2 has a theoretical specific capacity of 335 mAh g^{-1} relative to full lithiated form LiTiO_2 and a voltage of Li intercalation in the range of 1.5-1.8 V vs. Li^+/Li . The most thermodynamically stable polymorph of TiO_2 , rutile (Figure 1.8a), in its bulk crystalline form can only accommodate negligible Li^+ (<0.1 Li per TiO_2 unit) at room temperature. Increased Li^+ reactivity (up to >0.5 Li per TiO_2 unit) was reported at 120°C . It is commonly agreed that Li^+ diffusion in rutile is highly anisotropic, which proceeds through rapid diffusion along c-axis channels. Therefore, transport is very slow in the ab-planes, limiting Li ions from reaching the thermodynamically favorable octahedral sites and restricting Li^+ in the c-channels. Furthermore, repulsive Li–Li interactions in c-channels together with trapped Li-ion pairs in the ab-planes may block the c-channels and restrict insertion well below its theoretical limit. Interestingly, however, the Li-reactivity increases with decreasing the particle size.

In comparison with the rutile structure, in the anatase lattice the uptake of Li^+ appears more facile. It has a tetragonal body-centered space group $I4_1/amd$, and is comprised of TiO_6 octahedra sharing two adjacent edges with two other octahedra so that planar double chains are formed (Figure 1.8b). Diffusion of Li ions in the anatase framework occurs along a reaction path connecting the octahedral interstitial sites. With Li-insertion the symmetry of the anatase unit cell decreases and, when $x = 0.5$ ($\text{Li}_{0.5}\text{TiO}_2$), its original $I4_1/amd$ symmetry transforms into the orthorhombic $Pmn2_1$ space group due to loss of symmetry in the y direction. The change in symmetry is accompanied by a decrease of the unit cell along the c-axis and an increase along the b-axis, resulting in a net increase of 4% of the unit cell volume and a rapid capacity fade. As thus, for bulk anatase, $x = 0.5$ is most consistently reported as the maximum electrochemical insertion of Li.

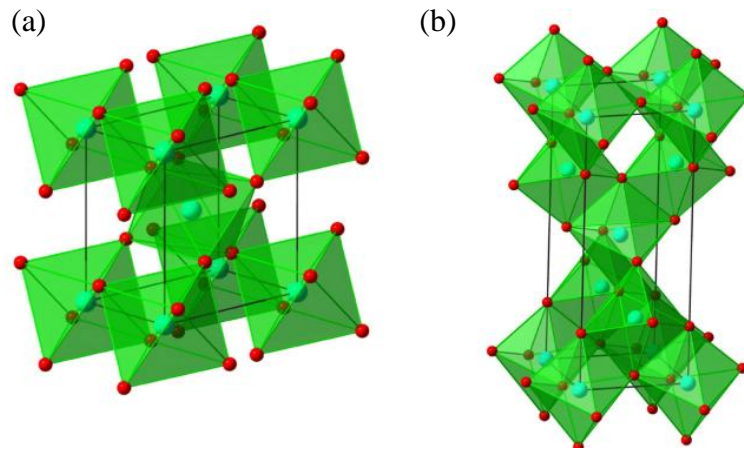
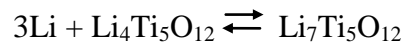


Figure 1.8. Schematic illustrations of the crystal structures of TiO₂ rutile (a) and anatase (b).

Li₄Ti₅O₁₂ accommodates Li with a theoretical capacity of 175 mAh g⁻¹, based on the mass of the starting host material, according to the equation:



The Li₄Ti₅O₁₂ possess a spinel structure that consists of a cubic close packed oxygen array in which Li occupies tetrahedral (8a) and octahedral (16c, 16d) sites, while Ti is located with part of Li ions at the 16d octahedral sites of a cubic unit cell (Fd3m) (Figure 1.9).

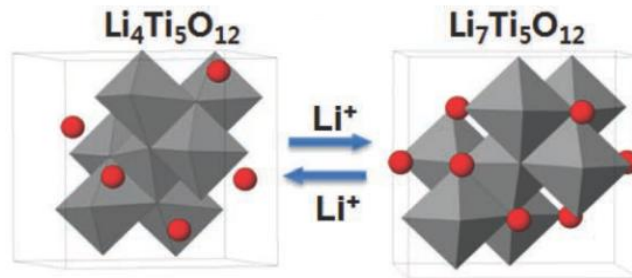


Figure 1.9 Structure of Li₄Ti₅O₁₂ and Li₇Ti₅O₁₂, showing no volume change after charge and discharge.

The total Li-insertion capacity is limited by the number of free octahedral sites. The Li₄Ti₅O₁₂ spinel framework provides a three-dimensional network of channels for facile Li⁺ diffusion. During the insertion process, the phase structure of the oxide changes from a spinel-type (Li₄Ti₅O₁₂) to a rock-salt type (Li₇Ti₅O₁₂), both structures have the same cubic lattice symmetry and a cell volume difference less than 0.1%. Thus, Li₄Ti₅O₁₂ is also named as a zero-strain lithium insertion material: this is a beneficial feature ensuring a long cycling life. Similar to LiFePO₄ cathode, the two-phase mechanism for the lithium

intercalation/deintercalation in $\text{Li}_4\text{Ti}_5\text{O}_{12}$ results in an flat discharge plateau at around 1.55 V (Figure 1.5d).

Lithium forms well-defined intermetallic phases (Li_xM) with numerous metals^{1,13} at room temperature if the metal is polarized to a sufficiently negative potential in a Li^+ cation containing liquid organic electrolyte. As the formation of the so-called ‘lithium alloys’ according to:



is usually quite reversible, metals which can alloy with lithium have found considerable interest for use as anode materials in rechargeable lithium batteries because both the theoretic specific capacity and capacity densities of lithium alloys are generally higher than those of the commonly used lithiated graphites (Figure 1.10).

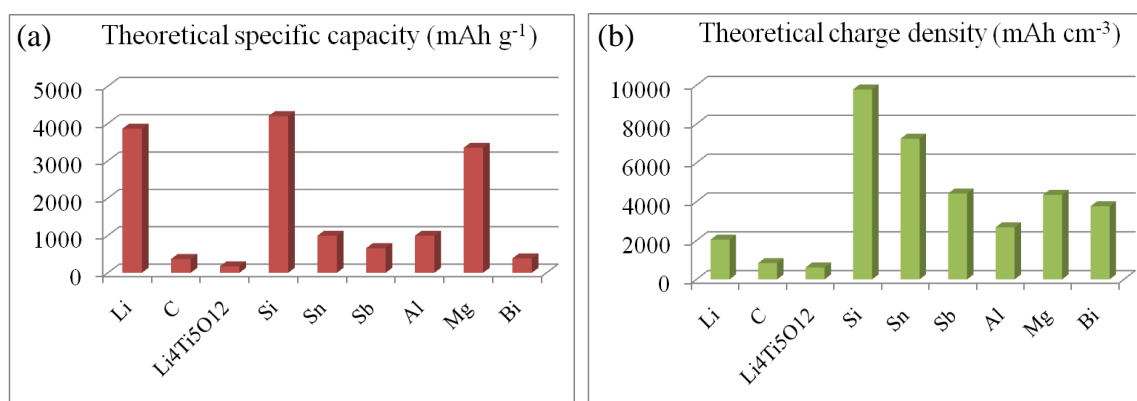


Figure 1.10. (a) Theoretical specific capacity (mAh g⁻¹) and (b) theoretical charge density (mAh cm⁻³) of lithiated anode materials for rechargeable lithium batteries.

A further striking feature of lithium alloys in comparison to lithiated graphite is that the operating potential may be well-above the potential of metallic lithium (1.0–0.3 V vs. Li/Li^+) avoiding the problems related to lithium plating. Despite these appreciable advantages, lithium alloys show some key limits that prevent their application as anode materials. The first one is that the metals undergo major changes in structure and in volume while alloying with lithium. The formation of $\text{Li}_x^+ \text{M}^{x-}$ require that the host metal does not only accommodate several mols of lithium ions per metal but also that accept the corresponding negative charges. The M^{x-} ions formed by the charge transfer reaction $\text{M}^0 + xe^- \leftrightarrow \text{M}^{x-}$ are noticeably larger than the neutral M^0 atoms and so the volume increase from the lithium-free to the full lithiated host is typically in the order of 100-

300%. Furthermore, in contrast to the metal hosts, lithium alloys are highly ionic and therefore they are generally quite brittle. In conclusion, mechanical stresses, related with the volume changes, induce a rapid decay in mechanical stability. The electrode suffers from cracking and crumbling (“pulverization”) as well as from consequent loss of electronic interparticle contact. Thus, without appropriate design of the metal host the lithium alloy electrode typically fails after only a few charge/discharge cycles.

Tin has been widely investigated because of its high theoretical energy density (993 mAh g⁻¹ corresponding to a Li/Sn atomic ratio of 4.4), low-cost, low toxicity and availability. As for the other lithium metal alloys, tin suffer from a drastic volume change of about 300% between Sn and Li_{4.4}Sn that causes the typical poor electrode cycle life. Nanometric materials and intermetallic compounds have been the main strategies pursued to reduce this drawback and, recently, tin or tin oxide/carbon composites have aroused much attention. It has also been reported that all-metal structured electrodes manufactured using three-dimensional current collectors and nanowire technology^{1,14} display enhanced performance with respect to conventional electrodes even in terms of cycling stability. Furthermore, the commercialization of Sony Nexelion™ lithium-ion battery bearing a composite anode based on an SnCo amorphous alloy has attracted much attention in regard to the production of a tin-based anode with low crystallinity.

1.4 Electrolytes

The electrolyte is usually a solution comprising the salts and solvents and constitutes the third fundamental component of a battery.

One of the most important discovery that allowed the development of primary lithium batteries was the practical stability of lithium metal in contact with electrolytes based on solvents such as propylene carbonate or butyrolactone, due to the passivation of the metal by an electronically insulating film which protected it from further attack. Regarding rechargeable lithium batteries, the historically earlier breakthrough in making lithium usable derived from the discovery of a new class of polymer electrolytes based on poly(ethyleneoxide) (PEO) made conducting through dissolution of lithium salts in the polymer. PEO with high molecular weight of about 5·10⁶ and 80% crystallinity was

usually employed as the polymer host to form complexes with lithium salts (Figure 1.11). The lithium salt complexed-poly(ethyleneoxide) PEO and -poly(propyleneoxide) PPO are the most extensively investigated “dry solid polymer” electrolyte systems in all solid state lithium batteries because they form more stable complexes and possess higher ionic conductivities than any other group of solvating polymers without the addition of organic solvents. PEO forms complex with many lithium salts and, in particular, PEO-LiCF₃SO₃ and PEO-LiClO₄ have been the most widely studied. Since the ion mobility in the polymer electrolytes was found to be accompanied by polymer chain mobilities, conductivity and ion transport were restricted to the amorphous phase of the polymer electrolyte . At about 100°C, above the melting point of PEO-lithium salt complexes, conductivities were three orders of magnitude higher than those at room temperature. This limited the applications of PEO-based electrolytes in lithium batteries at temperatures near 100°C. Some progress has been achieved by dispersing ceramic additives at the nanoparticle size in the polymer bulk^{1,15}, widening the useful range of temperature but not yet to a level to make the these electrolytes suitable for ambient-temperature batteries. On the other hand, the high temperature of operation may not be a critical factor in the automobile sector, so the lithium metal polymer rechargeable battery is still very appealing and is presently being studied in industrial laboratories involved in electric transportation.

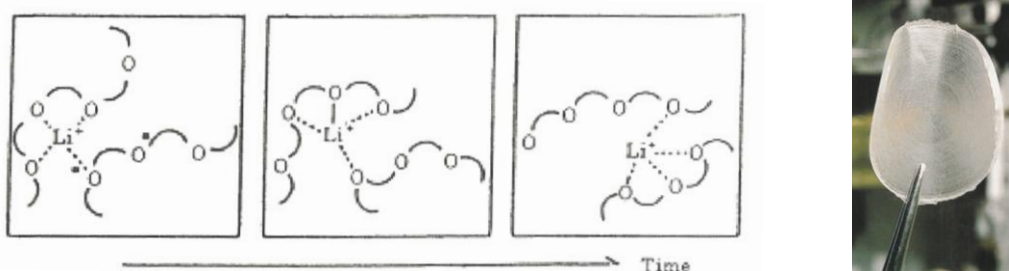


Figure 1.11. (a) Lithium conduction mechanism through the polymer; (b) PEO-LiClO₄ membrane.

In Li-ion batteries, the choice of electrolyte components become even more complex, since to the optimization of lithium transport in the electrolyte phase was added the requirement of formation of an optimum SEI morphology. Furthermore, the development of cathodes with very positive reduction potentials brought about the need for stability to oxidation, which as with reduction, must generally rely on kinetic inhibition. By using a mixed solvent system it become possible to obtain the best compromise between

electrolyte and electrode performance. Typical electrolytes contain organic carbonates (Figure 1.12). An optimized solvent contains a high dielectric component as ethylene carbonate (EC), the only one which can provide the suitable protective layer on the surface of graphite, and a dialkylcarbonate as dimethylcarbonate (DMC) to control the film formation and to lower the melting point of the mixture. Sometimes, also a low viscosity component as 1,2-dimethoxyethane (DME) is added to improve the conductivity.

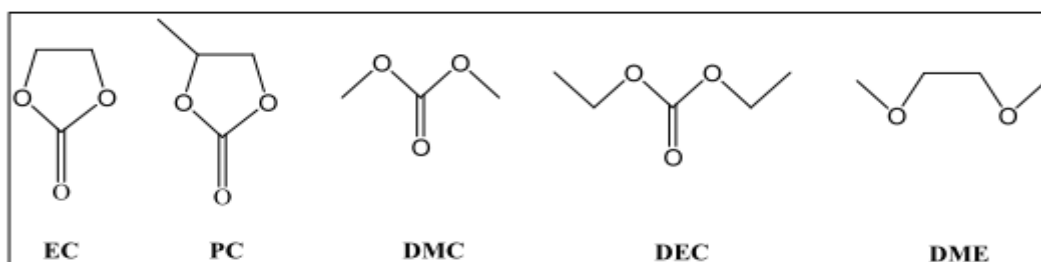


Figure 1.12. Structural formulas of the most used organic solvents.

The salts traditionally used in lithium and lithium-ion battery electrolytes are LiClO_4 (which is not used commercially owing to safety risks), LiPF_6 , LiBF_4 and LiAsF_6 . All three latter salts are resistant to oxidation and reduction but have also some drawbacks: all can initiate polymerization of cyclic esters, LiAsF_6 is environmentally unfriendly, conductivity of LiBF_4 -based solutions is relatively low and LiPF_6 is thermally unstable (but only moderately in solution). Furthermore, a range of stable salts based on the sulphonate group, $-\text{SO}_3^-$ have been developed, which include lithium triflate (LiCF_3SO_3) and lithium imide ($\text{LiN}(\text{SO}_2\text{CF}_3)$), but the first gives electrolyte solutions of too low conductivities and the latter do not effectively passivate the aluminum current collector at the positive electrode, leading to its corrosion. Nowadays, the most used electrolyte salt in commercial lithium-ion batteries is LiPF_6 .

Another, promising class of electrolytes is that based on ionic liquids (ILs), namely, low temperature molten salts having important specific chemical, electrochemical and physical properties that are determined by the nature of cations and anions. ILs are characterized by high boiling/decomposition points (even higher than 400°C) and, given their low melting points, they have a large liquidus range; they are also thermally and electrochemically stable, with appreciable conductivity above RT and considered green solvents. This unique combination of favorable properties make ILs very appealing as stable and safe electrolyte media in lithium-ion batteries. Typically, ILs are formed by the

combination of a weakly interacting, large cation, e.g. of the imidazole type, and a flexible anion, e.g. N,N-bis(trifluoromethanesulfonyl)imide (TFSI) (Figure 1.13).

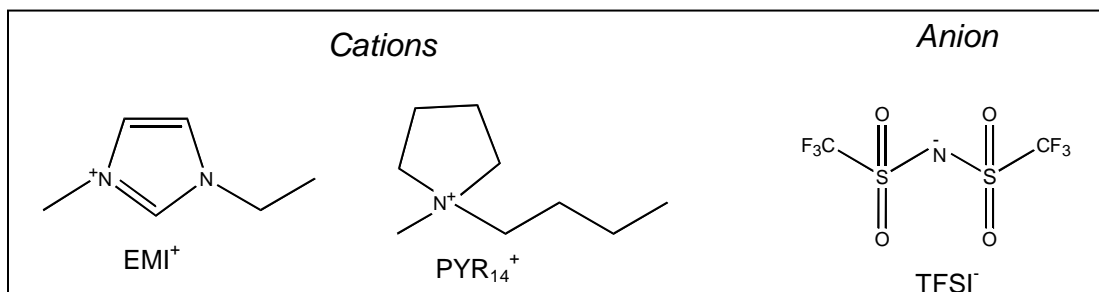


Figure 1.13. Structures of cations and anion of some ILs.

Most commonly these solutions have a poor cathodic stability limit associated with the tendency of imidazolium-based cations to be reduced by electrochemical deprotonation around 1.5 V vs. Li. This apparently prevents the use of IL-based solutions with common low voltage anode materials. The use of aliphatic quaternary ammonium cations having no acidic protons extends the stability domain to low voltages. A good example is the IL formed by combining N-n-butyl-N-ethyl-pyrrolidinium cation (PYR₁₄⁺) with N,N-bis(trifluoromethanesulfonyl) imide anion (TFSI) having lithium N,N-bis(trifluoromethanesulfonyl) imide (LiTFSI) as the dissolved lithium salt.

1.5 Safety issues

Lithium-ion batteries combine highly energetic materials in contact with a flammable electrolyte based on organic solvents. They can suffer premature failure due to spontaneous heat-evolving reactions, if subjected to abuse conditions (overheating, overcharging, external short circuiting or crushing) which can lead to fire and explosion (Figure 1.14). Moreover their safety is compounded by the fact that the design of these cells has an intrinsic drawback of poor heat dissipation.



Figure 1.14. Example of laptop and car incidents caused by battery catching on fire.

In lithium-ion batteries (as in lithium batteries) there are many sources of spontaneous exothermic reactions^{1,16}. For example, the potential ranges used in common 4V lithium-ion cells are beyond the thermodynamic stability windows of the electrolytes. Therefore, electrolytes have a tendency to decompose upon contact with the charged active materials of both negative and positive electrodes, in particular at the end of charging and at elevated temperatures, conditions under which electrolyte oxidation can proceed at accelerated rates. If the heat generated is more than that can be dissipated, the exothermic processes would proceed under adiabatic-like conditions and the cell's temperature will increase quickly. The rise in temperature will further accelerate the chemical reactions, rather than the desired galvanic reactions, causing even more heat to be produced, eventually resulting in thermal runaway. Possible exothermic reactions that trigger thermal runaway include: (i) thermal decomposition of the electrolyte, (ii) reduction of the electrolyte by the anode, (iii) oxidation of the electrolyte by the cathode, (iv) thermal decomposition of the electrodes and (v) melting of the separator and the resulting internal short. Furthermore, high-voltage metal-oxide cathodes are known to release oxygen at high temperatures. Typical abuse conditions that often cause thermal runaway can have many sources: thermal (overheating), electrical (overcharge, high pulse power) or mechanical (crushing, internal or external short circuit). Lithium-ion battery electrolytes based on alkyl carbonate solvents are known to react vigorously at elevated temperatures with lithiated graphite and delithiated cathodes (e.g., Li_xCoO_2 with $x < 0.5$). The high temperatures cause the destruction of SEI on the graphite anode, allowing rapid and direct reaction of electrolyte with the lithiated graphite underneath the passivating layer. Moreover, in their delithiated forms, cathodes based on oxides are highly oxidizing and

start exothermic reactions with alkyl carbonates, especially at elevated temperatures. Thermal studies on lithium batteries have been performed with anodes in their lithiated state and cathodes in the delithiated state recognizing that the cell temperatures during abuse reactions can melt the aluminum current collector but not the copper current collector and concluding that cell temperatures should reach between 659°C (mp of Al) and 1083°C (mp of Cu).

There are a lot of mechanisms by which lithium-ion batteries are rendered safe (control devices, electrolyte additives, shutdown separators) but the most effective involves the elimination of the primary sources of unwanted reactions, which means a change of the chemistry of active materials and electrolytes. Anodes and cathodes working in the stability window of electrolytes avoid problems related to SEI destruction at elevated temperatures. For example the most promising alternative to LiCoO_2 for large-size lithium-ion cells is LiFePO_4 . It is thermally stable, its reactivity with electrolytes is very low (no SEI formation) and no heat evolution is observed below 200°C. Finally, the use of non-flammable electrolytes, or even “low flammability” or “flame retarding” electrolytes that do not support continued combustion when the source of heat, spark or flame is withdrawn, remove the main safety issue. Further improvements in safety are fundamental, especially with large lithium-ion battery packs as for electric cars.

1.6 Electric and hybrid electric vehicles

An electric vehicle (EV) uses electric motor for propulsion. Electric propulsion is today the most used in some application (e.g. trains, submarines, spacecrafts) but not in others (e.g. cars), however, during the last few decades, the petroleum price raising and increased concern over the environmental impact of the fossil fuel combustion have led to renewed interest in an electric transportation infrastructure. Electric vehicles differ from fossil fuel-powered vehicles in that the electricity they consume can be generated from a wide range of sources, including fossil fuels, nuclear power and renewable sources. The electricity is stored onboard the vehicle using a battery or supercapacitors. The key advantages of electric vehicles are: i) electric motors often achieve 90% energy conversion efficiency (while internal combustion engine in a conventional car have a energy

conversion efficiency of only 25%); ii) regenerative braking system, which convert movement energy back into stored electricity; iii) EVs release almost no air pollutants; iv) low recharge cost. The main disadvantages of electric vehicle is the limited range, due to the low energy density of batteries, and the long recharge time compared to the relatively fast process of refueling a conventional car.

A battery electric vehicle (BEV) is a type of electric vehicle that uses chemical energy stored in rechargeable battery packs charged using the electric grid. Battery electric cars are becoming more and more attractive with the advancement of lithium-ion battery technology that have higher power and energy density.

Hybrid electric vehicles (HEVs) are the bridge between conventional vehicles and electric vehicles. In fact, even if electric vehicles are considered the best technology of transportation in terms of efficiency and low emissions their performance are still far from that of a combustion-engine vehicle. Thus, today the automobile large-scale production is focused on HEVs rather than EVs, as showed by the planetary success of some HEV models (Toyota Prius, Honda Insight).

Technological complexity related to a HEV is higher than EV as a consequence of the need of the optimal synergy between conventional engine and electric motor. HEVs have a conventional engine (gasoline or diesel) as well as a large battery and an electric motor, so that the wheels of the car are driven by both an internal combustion engine and an electric motor (Figure 1.15). The presence of the electric powertrain is intended to achieve either better fuel economy than a conventional vehicle, or better performance, because of the high efficiency of electric motor compared to internal combustion one. There are various arrangements for these two motors: parallel hybrid car (the most common at present), where both the conventional engine and the electric motor are attached to the driveshaft and the wheels of the car; series hybrid car where the conventional engine is used only to generate electricity that then goes to an electric motor that drives the wheels. In particular, in a parallel HEV the electric motor assists in acceleration, which allows for a smaller and more efficient internal combustion engine. At low speeds, the car can use only the electric motor for a limited time, while at medium or high speeds, the electric motor provides power during accelerations while the internal combustion engine operate at its most energy efficient point. In a series hybrid vehicle, the internal combustion engine is not connected to the wheels of the car and it is used only to

generate electricity, which powers the electric motor and is also fed into the battery at times when the car does not need all the energy produced. This internal combustion engine needs only to produce the average amount of power required by the car; it is much smaller than those in conventional cars, and it usually operates at its most efficient point and at constant speed. All HEV types have regenerative braking systems. Hybrids commercialized today are called "charge-sustaining": all the electricity that goes into the battery is produced by the internal combustion engine. Another class of hybrids, called "charge-depleting" or "plug-in," have batteries that can be charged from the electricity net, but are not yet commercialized.

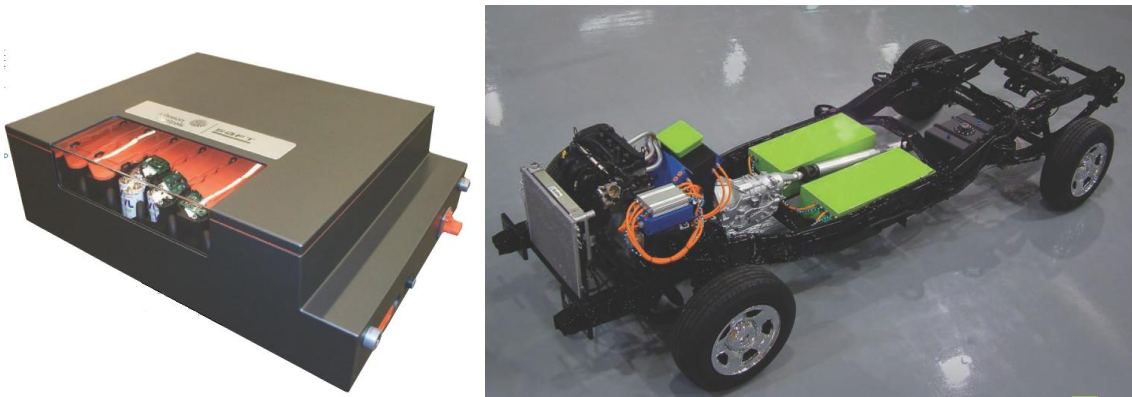


Figure 1.15 HEV battery pack and HEV chassis in which are visible the two battery packs (green central boxes)

1.7 Objective of the thesis

This thesis work is focused on the development of innovative safe lithium-ion and lithium batteries for application on hybrid electric vehicle and electric vehicle. One strategy was to utilize electrode materials intrinsically safe, such as LiFePO_4 as cathode and titanium-based high voltage anodes. Another strategy was to use novel electrolytes based on ionic liquid, whose unique favourable properties in terms of non-flammability, thermal and electrochemical stability and appreciable conductivity, make very appealing materials as stable and safe electrolyte media in lithium-ion batteries. The various typology of batteries assembled were tested following the protocol of Department of Energy USA

for application on power assist HEV. Furthermore a polymeric lithium battery Li/PEO/LiFePO₄ battery was tested for application in electric vehicle.

We also investigated the synthesis and the electrochemical performance of an anode for lithium-ion batteries based on SnCo amorphous alloy.

1.8 References

- [1.1] Ikeda, H., Saito, T. & Tamura, H. in Proc. Manganese Dioxide Symp. Vol. 1 (eds Kozawa, A. & Brodd, R.H.) (IC sample Office, Cleveland, OH, 1975)
- [1.2] C. Arbizzani, S. Beninati, L. Damen, M. Mastragostino, Solid State Ionics 178 (2007) 393–398
- [1.3] Armand, M., Chabagno, J. M. & Duclot, M. J. in Fast Ion Transport in Solids Electrodes and Electrolytes (eds Vashishta, P., Mundy, J.-N. & Shenoy, G. K.) 131–136 (North-Holland, Amsterdam, 1979).
- [1.4] D. W. Murphy, F. J Di Salvo, J. N. Carides and J. V. Waszczak, Topochemical reactions of rutile related structures with lithium. Mat. Res. Bull. 13, 1395–1402 (1978)
- [1.5] M. Lazzari and B. Scrosati, A cyclable lithium organic electrolyte cell based on two intercalation electrodes. J. Electrochem. Soc. 127, 773–774 (1980)
- [1.6] K. Mizushima, P.C. Jones, P.J. Wiseman and J.B. Goodenough, Li_xCoO₂ (0<x<1): a new cathode material for batteries of high energy density. Mat. Res. Bull. 15, 783–789 (1980)]
- [1.7] T. Nagaura, Prog. Batteries Solar Cells 10 (1991) 209–226
- [1.8] B. L. Ellis, K. Tae Lee and L. F. Nazar, Chem. Mater. 22 (2010) 691-714
- [1.9] Y. Koyama, N. Yabuuchi, I. Tanaka, H. Adachi, T. Ohzuku, J. Electrochem. Soc. 151 (2004) A1545–A1551.
- [1.10] M. Winter, J. O. Besenhard, M. E. Spahr, and Petr Novak, Adv. Mater. 1998, 10, No. 10
- [1.11] Da Deng, Min Gyu Kim, Jim Yang Lee and Jaephil Cho, Energy Environ. Sci., 2009, 2, 818–837
- [1.12] T. Ohzuku, A. Ueda, N. Yamamoto, J. Electrochem. Soc. 142 (1995) 1431–1435.
- [1.13] M. Winter, J.O. Besenhard, Electrochimica Acta 45 (1999) 31–50

- [1.14] G. Ferrara, L. Damen, C. Arbizzani, R. Inguanta, S. Piazza, C. Sunseri, M. Mastragostino, *Journal of Power Sources* 196 (2011) 1469–1473
- [1.15] F. Croce, G.B. Appetecchi, L. Persi, B. Scrosati, *Nature* 394 (1998) 456
- [1.16] P.G. Balakrishnan, R. Ramesh, T. Prem Kumar, *Journal of Power Sources* 155 (2006) 401–414.

Chapter 2

Chemicals, Techniques and Analyses

2.1. Chemicals

The carbon-coated LiFePO_4 cathode material was synthesized by microwave accelerated sol-gel synthesis. The precursors of the synthesis were Fe(III)-citrate (home-made, from commercial citric acid and $\text{Fe}(\text{OH})_3$ from Fluka, H_3PO_4 and Li_3PO_4 from Sigma-Aldrich. The details of this preparation are in Section 4.2. The purity of the product was measured with potassium thiocyanate (Sigma-Aldrich) and Fe(III)-nitrate (Merck) by spectrophotometric measurements.

Anode powders were all commercial: graphite Timrex KS-15 (TIMCAL), TiO_2 anatase (nanocrystalline <10nm, Hombifine N, Sachtleben), $\text{Li}_4\text{Ti}_5\text{O}_{12}$ (nanoparticles <100nm, Sigma-Aldrich, purity grade >99%); the powders were dried in Büchi Glass Oven B-580 over night at 80°C under dynamic vacuum before use. SnCo alloy anodes were prepared by Dipartimento di Ingegneria Chimica dei Processi e dei Materiali, University of Palermo, in the frame of a scientific collaboration, as in Section 5.3.1.

Binders used for electrode preparations were polyvinylidene fluoride (PVDF, Fluka) and polytetrafluoroethylene (PTFE, Du Pont, 60 wt.% water dispersion); solvents were N-methyl-2-pyrrolidone (NMP, Fluka, purity grade >99%) and absolute ethanol (EtOH, Carlo Erba); carbon conducting additive was SuperP (MMM Carbon Co.).

Electrolytes used in electrochemical cells were: ethylene carbonate (EC): dimethylcarbonate (DMC) 1:1-1 M LiPF_6 (Ferro Corp.), ionic liquid N-n-butyl-N-ethylpyrrolidinium-N,N-bis(trifluoromethanesulfonyl) imide (Solvent Innovations, purity grade 98%) with 0.4m of N,N-bis(trifluoromethanesulfonyl) imide (3M) as the dissolved lithium salt ($\text{PYR}_{14}\text{TFSI-LiTFSI}$) and a $\text{PEO}_{20}\text{-LiCF}_3\text{SO}_3 + 10\% \text{ZrO}_2$ polymer electrolyte (prepared by Department of Chemistry, University “La Sapienza”, Rome, partner of national project PRIN).

Vinylene carbonate additive for ionic liquid was a commercial product (97%, Fluka).

2.2. Instruments for synthesis and chemical-physical characterizations

The MW oven used for LiFePO₄-C synthesis was a single-mode CEM Discover scientific oven (2.45 GHz)^{2,1}. The XRD analyses were performed by a Philips PW1710 diffractometer, a Cu K α ($\lambda=1.5406\text{\AA}$) radiation source and Ni filter with continuous acquisition in 10-80° 2 θ range, 0.05° 2 θ s⁻¹ scan rate. The TGA analysis of the LiFePO₄-C powder, was carried out by Mettler Toledo TGA/SDTA A851 from room temperature (RT) to 700°C (heating rate 5°C min⁻¹) in O₂ flux. The potentiometric titration analyses of LiFePO₄-C were performed by a 794 Basic Titrino (Metrohm).

2.3. Electrode preparation and cell configuration

The LiFePO₄-C electrodes were prepared by lamination on carbon-coated aluminum grid (Lamart) of a paste obtained by mixing 80 wt.% LiFePO₄-C, 15 wt.% carbon conducting additive SuperP and 5 wt.% PTFE binder in a small amount of ethanol; the electrodes were dried at 80°C under vacuum over night before use. The geometric electrode area was 0.61 cm².

The graphite electrodes were prepared by lamination or by “doctor-blade” technique. Lamination was performed on copper grid (Lamart) of a paste obtained by mixing 88 wt.% graphite (dried at 200°C under vacuum over night), 5 wt.% carbon SuperP and 7 wt.% PTFE in ethanol, and the electrodes were further dried overnight at 100°C under vacuum before battery assembly. The geometric electrode area was 0.61 cm². The “doctor-blade” technique started preparing slurries with the following compositions: graphite:SuperP:PVDF = 88:5:7, 85.2:5:9.8 and 70:10:20 wt.%. The slurries were coated onto a copper porous foil (Schlenk, thickness 0.01 mm) as current collector using the doctor blade and dried at 120°C under vacuum overnight. Circular electrodes were cut from the foil with a geometric area of 0.61 cm².

The TiO₂ electrodes were manufactured by preparing slurries with the following compositions: TiO₂:SuperP:PVDF =70:10:20 and 76:12:12 wt %. The slurries were coated onto a copper porous foil (Schlenk, thickness 0.01 mm) as current collector using “doctor blade” technique and dried at 120°C under vacuum overnight. Circular electrodes were cut

from the foil with a geometric area of 0.64 cm^2 . Electrodes derived from the composition 76:12:12 were pressed at 4 ton for 5 minutes for better contact between particles and current collector. Lamination technique for TiO_2 electrodes production did not give acceptable results.

The $\text{Li}_4\text{Ti}_5\text{O}_{12}$ electrodes were prepared using both the two techniques above-mentioned. The paste had the composition of $\text{Li}_4\text{Ti}_5\text{O}_{12}$:SuperP:PTFE=80:10:10 wt.% (geometric electrode area of 0.61 cm^2). Three slurries with different compositions were prepared with $\text{Li}_4\text{Ti}_5\text{O}_{12}$:SuperP:PVDF = 70:10:20 or 76:12:12 or 80:10:10 wt.% (geometric electrode area of 0.64 cm^2). The slurry was coated onto a aluminium foil as current collector using “doctor blade” technique and dried at 120°C under vacuum overnight. Furthermore, electrodes derived from the last two were pressed at 4 ton for 5 minutes for better contact between particles and current collector.

SnCo electrodes were cut with a geometric electrode area of 0.61 cm^2 and dried over night at 80°C under dynamic vacuum before use.

Three-electrode Swagelok-type cells with Li reference electrode were used for electrodes characterization both in cell vs. Li and in lithium-ion batteries (figures 2.1 and 2.2). While Li in excess was the counter for the former, a LiFePO_4 -C cathode and different anodes with balanced capacity were used for the lithium-ion batteries. A dried and degassed glass separator (Whatman GF/D 400- μm thick) or fiberglass separator (Durieux, 200 μm thick when pressed) were used after soaking in the same electrolyte of the electrochemical cell.

For the lithium polymer battery, the geometric LiFePO_4 -C based cathode area was 0.38 cm^2 and the composite mass loading was 3.7 mg cm^{-2} . The PEO_{20} - LiCF_3SO_3 + 10% ZrO_2 polymer electrolyte separator (thickness of 250 μm , density of 0.95 g cm^{-3}) was cut into the proper shape. Li metal in excess was used as anode. The cell components were placed inside a Teflon container having two stainless-steel current collectors (figure 2.3).

Cells assembly and sealing was performed in an argon atmosphere MBraun Labmaster 130 dry box (H_2O and $\text{O}_2 < 1 \text{ ppm}$).

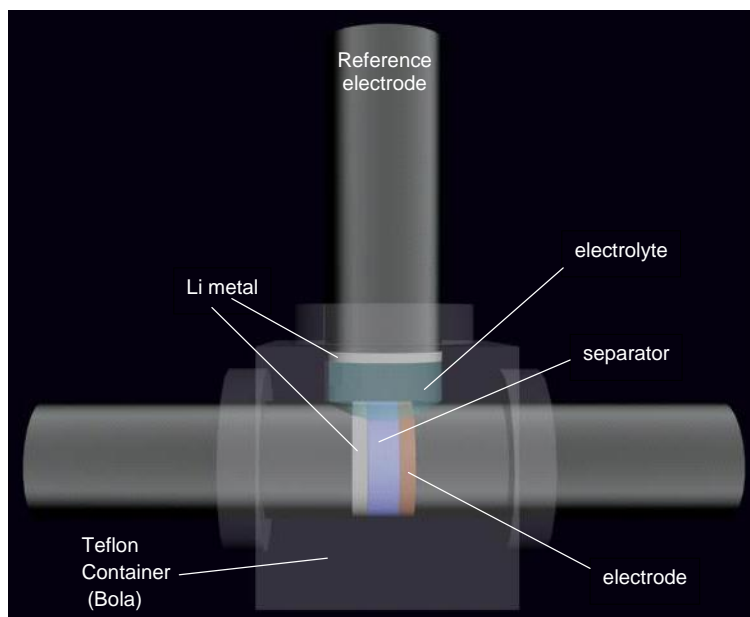


Figure 2.1 Schematic representation of the used three-electrode Swagelok-type cells with Li counter and reference electrodes

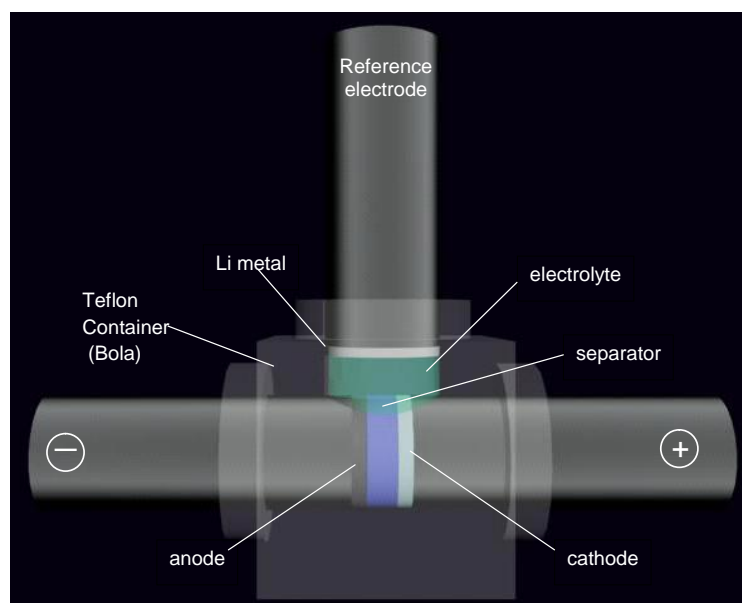


Figure 2.2 Schematic representation of the used three-electrode Swagelok-type lithium-ion batteries.

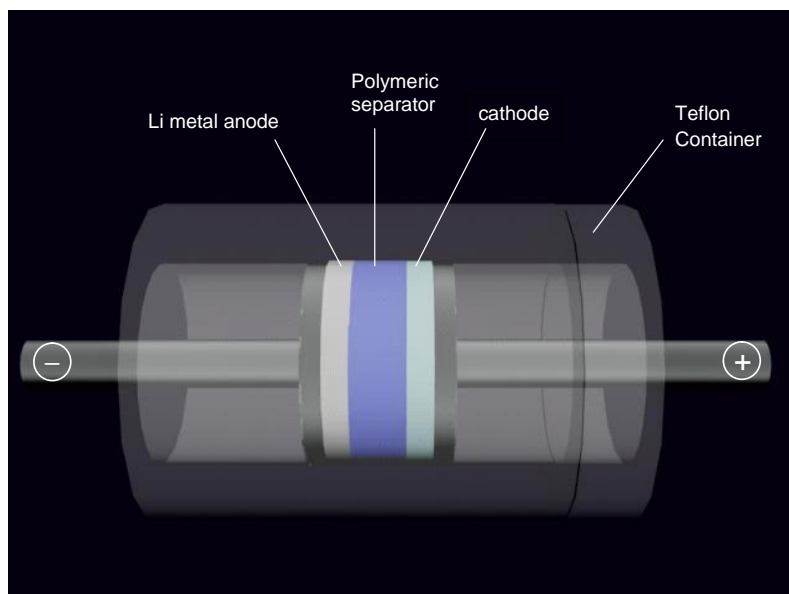


Figure 2.3 Schematic representation of the used two-electrode lithium batteries.

2.4. Electrochemical characterization of electrodes and batteries

The electrochemical characterization of the electrodes was carried out in cell configuration vs. Li by conventional deep galvanostatic charge-discharge cycles at different C-rates, set on the basis of the theoretic specific capacity of the active materials. The efficiency (η) of the electrodes is referred to the discharge/charge capacity ratio (in percentage) on a specific cycle. During the electrochemical tests the cells were kept at controlled temperatures by a Thermoblock (FALC). Galvanostatic charge-discharge cycles were performed with a Perkin–Elmer VMP multichannel potentiostat/galvanostat.

We characterized the lithium-ion batteries by USABC–DOE benchmark tests to simulate dynamic battery functioning in power-assist full HEV, where the battery is used during acceleration for a short time and kept within a DOD range (never approaching the fully charged or fully discharged state) by the regenerative braking or the engine. As reported in the “FreedomCAR battery Test Manual for Power-Assist Hybrid Electric Vehicle”^{2,2}, the USABC–DOE tests include a static capacity test (SCT) at 1C discharge rate and a hybrid pulse power characterization (HPPC) tests at 30°C, which provide the battery dynamic-power capability over usable charge and voltage ranges. A lower voltage limit (V_{MIN}) for battery discharge of 55% of the maximum (V_{MAX}) is recommended as well

as HPPC tests at low and at high current. Each test incorporates both discharge and regenerative pulses: the battery is first pulse discharged for 10s at the stated C-rate, then allowed to relax to the OCV for 40s, and finally charged for 10s with a regenerative pulse at 75% current of the discharge pulse. This sequence is repeated, from 10% to 90% DOD, with 10% increment through discharge steps at 1C-rate, each followed by a 1-h rest period before applying the next sequence. The HPPC test begins with a fully 1-C charged battery after 1h OCV rest and ends before 90% DOD if the battery voltage exceeds the V_{\max} in regenerative or V_{\min} in discharge pulse. The results of the SCT and HPPC tests are used to plot the available energy vs. pulse power capability and evaluate whether the battery matches the target for power-assist full HEV (Table 2.1).

Table 2.1. USABC-DOE targets for power-assist HEV

Pulse discharge power	25 kW for 10s; (625 W kg ⁻¹)
Pulse regenerative power	20 kW for 10s; (500 W kg ⁻¹)
Total available energy	0.3 kWh; (7.5 Wh kg ⁻¹)
Efficiency	> 90% (25Wh-cycle)
Cycle life	3·10 ⁵ cycles (25Wh-cycle)
Calendar life	15 years
Maximum weight	40 kg

The lithium polymer battery was characterized for specific energy and power after the EV protocol set by the USABC-DOE, as reported in “Electric vehicle battery test procedures manual”^{2,3}, focusing on “Constant Current Discharge Test” and “Peak Power Tests” to simulate battery functioning in EV. The purpose of constant current tests is to estimate the effective capacity of the cell at different C-rates. Accordingly, charge/discharge cycles at C/10, C/5, C/3 and C/2 were carried out, including C/1 discharges after C/10 charges. As stated in the manual, the specific energy of the LPB is evaluated from the C/3 discharge. The Peak Power Test (PPT) is designed to determine the sustained (30s) discharge power capability of the battery at various depths of discharge (DOD). The value calculated at 80% DOD is of key importance because it provides the point at which the battery performance have to be compared with the USABC-DOE power target (Table 2.2).

Table 2.2 USABC Goals for Advanced Batteries for EVs.

	USABC goal
Specific power, discharge at 80% DOD/30s (W kg^{-1})	400
Specific energy, C/3 discharge rate (Wh kg^{-1})	200

2.5 References

- 2.1) C. Arbizzani S. Beninati, L. Damen, M. Mastragostino, *Solid State Ionics* 178 (2007) 393–398
- 2.2) INEEL, *FreedomCAR Battery Test Manual For Power-Assist Hybrid Electric Vehicles*, Prepared for the U.S. Department of Energy (2003).
- 2.3) United States Advanced Battery Consortium (USABC), *Electric Vehicle Battery Test Procedure Manual*, 1996.

Chapter 3

Electrolytes

3.1. Chemical, physical and electrochemical properties of EC DMC-LiPF₆ 1M

Conventional electrolyte EC DMC - LiPF₆ 1M used was a commercial product (LP30 Merck). Physical properties of the electrolyte solvents are reported in Table 3.1. Physical and chemical properties of the electrolyte are reported in Table 3.2 and Figure 3.1.

Table 3.1. Physical properties of conventional electrolyte solvents (from Merck datasheet).

Solvent	Melting point (°C, 1 atm)	Boiling point (°C, 1 atm)	Density (at 20°C) (g cm ⁻³)	Permittivity	Viscosity (cP)	Dielectric constant (at 25°C)	Flash point (°C)
Ethylene carbonate (EC)	35-38	247-249	1.41	95.3	2.53	95	~150
Dimethyl carbonate (DMC)	2-4	90	1.07	3.12	0.6	3	~15

Table 3.2. Physical and chemical properties of EC DMC-LiPF₆ 1M electrolyte (from Merck datasheet) .

Density (at 20°C)	1.28 g cm ⁻³
Composition	LiPF ₆ 11.8 wt.% EC 44.1wt.% DMC 44.1wt.%
HF content	max 50 ppm
H₂O content	max 20 ppm

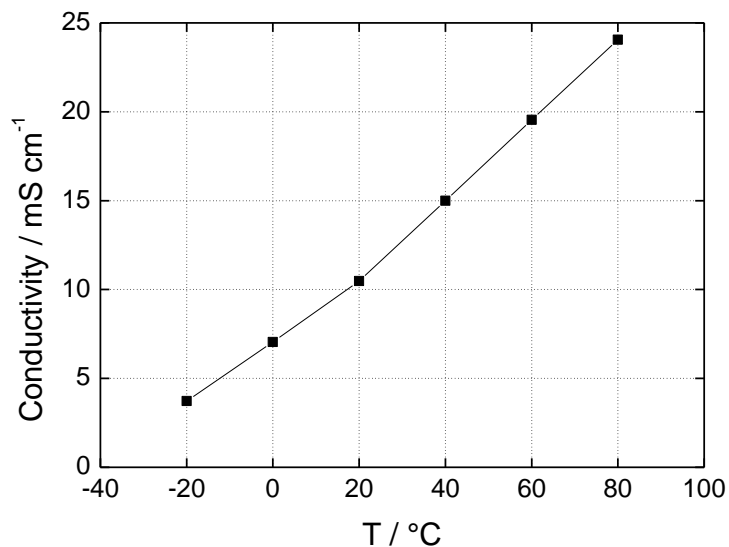


Figure 3.1 Conductivity at different temperatures of EC:DMC (50:50 wt.%) LiPF₆ 1M (from Merck datasheet).

3.2 Chemical, physical and electrochemical properties of the ionic liquid-based electrolyte PYR₁₄TFSI-LiTFSI 0.4m

The ionic liquid PYR₁₄TFSI (Solvent Innovations, molecular weight 422.41, density 1.41 g ml⁻¹), used as solvent for ionic liquid-based electrolyte, was dried at 100°C under dynamic vacuum before use. The thermal stability of the ionic liquid was investigated by TGA in O₂ and N₂ (Figure 3.2).

The electrochemical stability window of PYR₁₄TFSI was evaluated by linear sweep voltammetry (LSV) on a glassy carbon electrode (GC, 0.07 cm²) with an Ag/AgTFSI-PYR₁₄TFSI (+3.50 V vs. Li/Li⁺) reference electrode at 30° and 60°C (Figure 3.3). PYR₁₄TFSI displays a wide potential range of electrochemical stability useful for many lithium-ion battery chemistries.

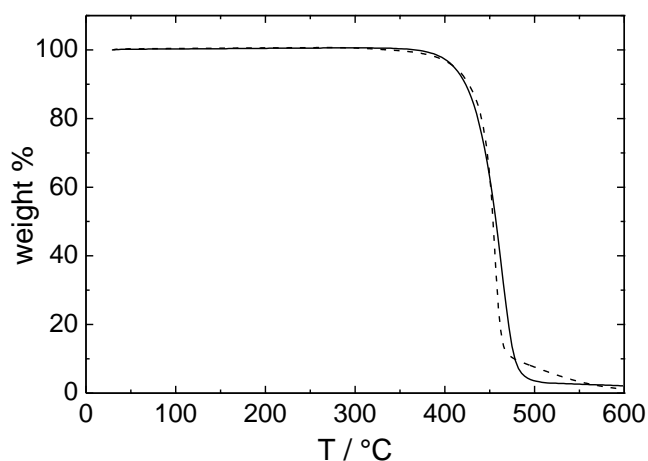


Figure 3.2. TGA of the ionic liquid PYR₁₄TFSI in nitrogen^{3,1} (solid line) and oxygen (dashed line) atmosphere

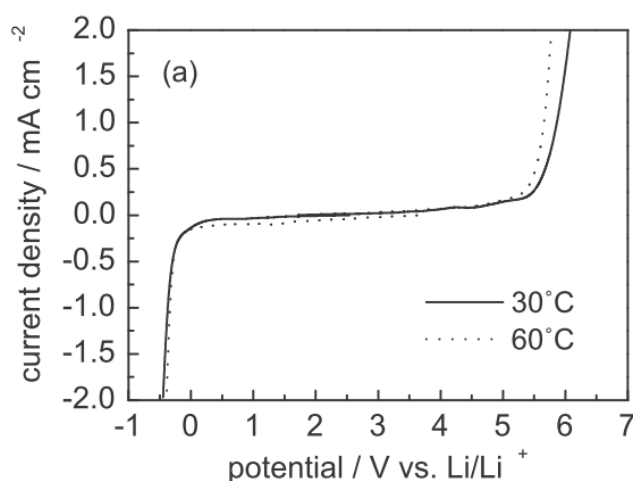


Figure 3.3 LSVs at 20 mV/s of PYR₁₄TFSI at 30 and 60°C with the potential reported vs.Li/Li⁺

The added lithium salt was lithium N,N-bis(trifluoromethanesulfonyl) imide (LiN(CF₃SO₂)₂) LiTFSI (molecular weight 287.09). In Figure 3.4 are shown the conductivities at different temperatures of pure ionic liquid and of ionic liquid with added lithium salt (0.4m and 1.0m). The conductivity decrease with the addition of lithium salt is related to the increase of viscosity of the liquid. As the best conductivity measured was that with 0.4 m lithium salt, this formulation was selected for electrode and complete battery tests.

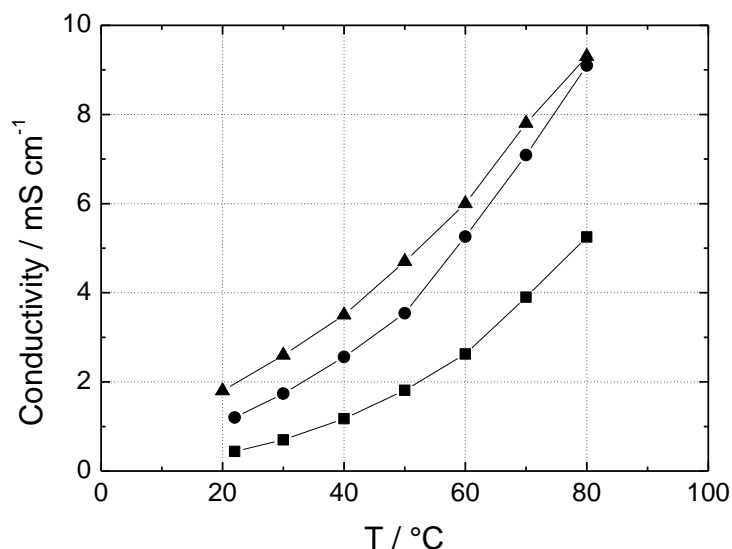


Figure 3.4 Conductivity at different temperatures of (▲)PYR₁₄TFSI, (●) PYR₁₄TFSI-LiTFSI 0.4m and (■)PYR₁₄TFSI-LiTFSI 1m

3.3 Chemical, physical and electrochemical properties of PYR₁₄TFSI/EC DMC-LiPF₆ 50%/50 wt.% mixture

The use of a mixture of ionic liquid and conventional organic electrolyte may be a good compromise to have an electrolyte with high conductivity and low flammability^{3.2}. We prepare an electrolyte mixing PYR₁₄TFSI and conventional organic electrolyte EC DMC-LiPF₆. TGA analyses of different electrolyte mixtures are reported in Figure 3.5^{3.3}. In Figure 3.6 is shown the conductivity of the mixture 50/50 wt.% compared with other used electrolytes.

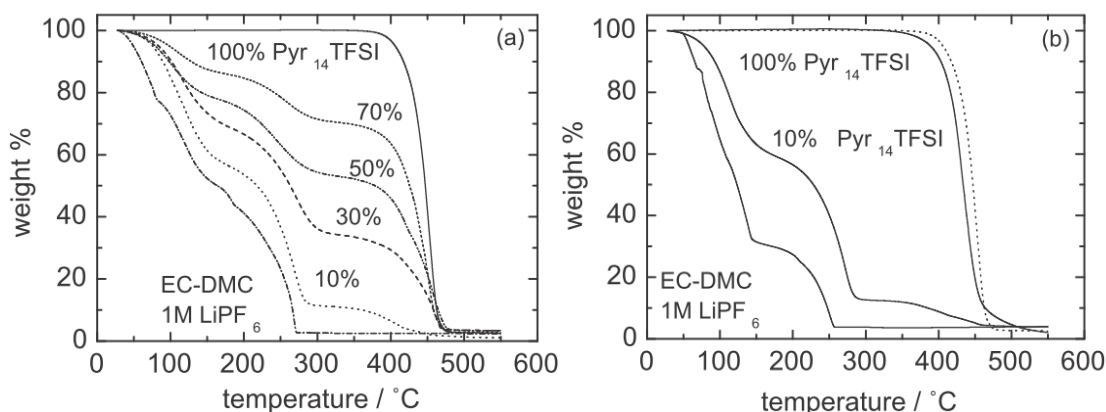


Figure 3.5 TGA curves of (a) EC DMC-LiPF₆ 1M, PYR₁₄TFSI and solutions with different wt% of PYR₁₄TFSI in N₂ flux and (b) EC-DMC LiPF₆ 1M, PYR₁₄TFSI and a solution with 10% PYR₁₄TFSI in N₂/O₂; for comparison the curve of PYR₁₄TFSI in N₂ flux (dotted line) is also reported.

Flammability tests of mixed electrolytes showed that the mixtures with 50 wt.% contents of ionic liquid is more difficult to ignite, so this formulation was selected for electrodes and complete batteries tests. However, it is worth noting that it burn for a longer time, once it is ignited.

3.4 Electrochemical properties of $\text{PYR}_{14}\text{TFSI}$ 0.4m LiTFSI with 10% VC

Given that SEI-forming additives, such as vinylene carbonate (VC), demonstrated to improve graphite anode performance in ionic liquid (as reported in details in the following pages 49-51), we prepared a new electrolyte adding 10 wt.% VC to 90 wt.% $\text{PYR}_{14}\text{TFSI}$ -LiTFSI 0.4 m. In Figure 3.6 is shown the conductivity at different temperatures of this electrolyte, compared with electrolytes discussed above.

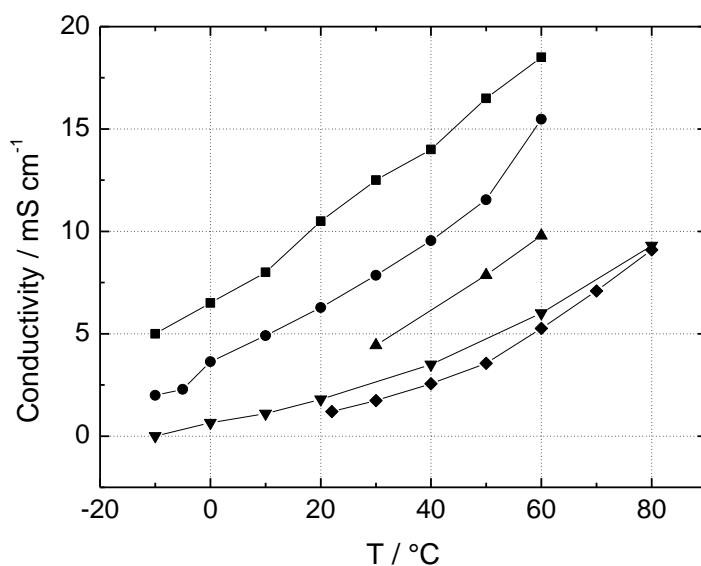


Figure 3.6 Conductivity data of EC DMC-LiPF₆ 1M (■), of $\text{PYR}_{14}\text{TFSI}$ /EC DMC-LiPF₆ 50%/50 wt.% mixture (●), of $\text{PYR}_{14}\text{TFSI}$ 0.4m LiTFSI with 10% VC (▲), of $\text{PYR}_{14}\text{TFSI}$ (▼) and of $\text{PYR}_{14}\text{TFSI}$ -LiTFSI 0.4 m (◆).

3.5 Electrochemical properties of PEO₂₀-LiCF₃SO₃+10%ZrO₂ polymer electrolyte

The polymer electrolyte was prepared by casting technique by mixing PEO with lithium salt LiCF₃SO₃ and ZrO₂ nanometric powder, as in Ref. 3.4. The Arrhenius plot of the PEO-based electrolyte added with ZrO₂ is shown in Figure 3.7 together with that of a PEO₂₀-LiCF₃SO₃ ceramic-free sample. It is evident that the addition of the filler causes an enhancement of about one order of magnitude in conductivity values above 60°C (around the crystallization temperature of the sample).

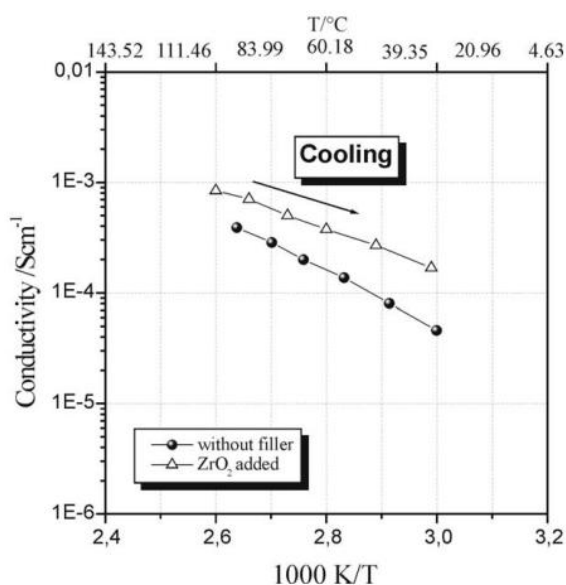


Figure 3.7 Arrhenius plot of conductivity of PEO₂₀-LiCF₃SO₃+10%ZrO₂ composite polymer electrolyte. The conductivity of a PEO₂₀-LiCF₃SO₃ ceramic-free sample is also reported for comparison purposes. Data obtained impedance measurements^{3,4}

3.6 Conclusions

Among ionic liquid-based electrolytes, PYR₁₄TFSI-LiTFSI 0.4m was selected for electrode and battery tests thanks to its acceptable conductivity, electrochemical and thermal stability. The mixture of ionic liquid and conventional organic electrolyte at 50 wt.% was chosen because showed good conductivity and low flammability. PYR₁₄TFSI 0.4m LiTFSI with 10% VC was investigated in view of the use in lithium-ion battery with graphite anode. The polymer electrolyte PEO₂₀-LiCF₃SO₃+10%ZrO₂ was chose as lithium battery electrolyte because of its relatively good conductivity.

3.7 References

- 3.1) D. Cericola, *Materiali carboniosi e liquidi ionici per supercapacitori a doppio strato*. Graduate Thesis, SMETEC Department, University of Bologna, Italy, October 2007.
- 3.2) A. Guerfi, M. Dontigny, P. Charest, M. Petitclerc, M. Lagacé, A. Vijn, K. Zaghbi, *Journal of Power Sources* 195 (2010) 845–852.
- 3.3) C. Arbizzani, G. Gabrielli, M. Mastragostino, *Journal of Power Sources* 2011, doi:10.1016/j.jpowsour.2011.01.068
- 3.4) F.S. Fiory, F. Croce, A. D'Epifanio, S. Licoccia, B. Scrosati, E. Traversa, *Journal of the European Ceramic Society* 24 (2004) 1385–1387.

Chapter 4

Cathode material

4.1 LiFePO₄-C

In this PhD research work much effort was focused on the development and characterization of electrode materials in view of the application in complete lithium-ion and lithium batteries. In particular, carbon-coated lithium iron phosphate (LiFePO₄-C) was selected because it is the most promising cathode material for safe, high power lithium-ion batteries in large format modules that are required for power-assist in hybrid electric vehicles and electric vehicles. The advantages of this nontoxic insertion material featuring a theoretical specific capacity of 170 mAh g⁻¹ are lithium insertion/extraction at less positive potentials than those of transition metal (Ni, Co and Mn) oxides and greater thermal stability against oxygen release, which makes it safer and more tolerant to abusive conditions.

4.2 Synthesis

The chemicals for LiFePO₄-C synthesis were Fe(III)-citrate (C₆H₅FeO₇) and commercial H₃PO₄ and Li₃PO₄. The C₆H₅FeO₇ was prepared after ref. 4.1 by adding a citric acid solution to one of Fe(OH)₃ and heating at 90°C for 2 h under stirring and then separating the product by precipitation with acetone. The purity grade of the C₆H₅FeO₇ was 96.5% as estimated by spectrophotometric measurements as follows: a few mg of Fe(III)-citrate were dissolved in 0.2 M HNO₃ and mixed with a solution, of potassium thiocyanate to form a complex with, maximum absorbance at 480 nm; the molar absorption coefficient at this wavelength as evaluated by a standard solution of Fe(III)-nitrate in 0.5 M HNO₃ was $\epsilon = 9.73 \cdot 10^3 \text{ l mol}^{-1} \text{ cm}^{-1}$. The precursors of sol-gel synthesis of carbon-coated lithium iron phosphate were Fe (III)-citrate, H₃PO₄ and Li₃PO₄, dissolved in water in exact stoichiometric molar ratio (Li:Fe:P = 1:1:1) as in ref. 4.2 and without any additional source of carbon than the citrate anion. After precursor dissolution in water, we accelerated the gel

formation step by MW processing that in a few minutes, instead of the several hours needed in a conventional sol-gel synthesis, provided an efficient water removal. As an example, 50 ml of solution containing 2 g of Fe(III)-citrate and stoichiometric amounts of H_3PO_4 and Li_3PO_4 was completely dried after 12 min of MW processing under stirring in the CEM Discover oven set at the 300 W maximum power; as the temperature started to increase rapidly above 100°C , the MW radiation automatically stopped. The dry gel was ground with a mortar and pestle and then pyrolyzed in furnace under reductive atmosphere (5% hydrogen in argon, 300 ml min^{-1}) for 1 h at 700°C (heating rate $20^\circ\text{C min}^{-1}$). The product, a black powder, was further ground in a mortar and chemically and structurally characterized before electrode preparation.

4.3 Chemical-physical properties

Figure 4.1 shows the X-ray pattern of the $\text{LiFePO}_4\text{-C}$ powder: the peaks are all related to LiFePO_4 , thereby demonstrating the efficacy of the fast synthesis procedure, and the crystallite size of the LiFePO_4 was 45 nm, as evaluated by Scherrer's equation from the 200 peak of XRD. To test the effectiveness of synthesis for yielding $\text{LiFePO}_4\text{-C}$ free from Fe(III) we performed the following analyses. We evaluated the amount of Fe(II) in the synthesized powder by potentiometric titration with potassium dichromate: ca. 50 mg of powder were dissolved in 10 ml of oxygen free $\text{HCl}/\text{H}_2\text{O}$ 1:1 and titrated under Ar. The amount of Fe(II) was then compared to that of total iron, estimated by spectrophotometric measurements as for the $\text{C}_6\text{H}_5\text{FeO}_7$ analysis, after $\text{LiFePO}_4\text{-C}$ dissolution in hot concentrated HNO_3 . Given that the amount of bivalent iron and total iron was the same (33.0 wt.%), we concluded that the $\text{LiFePO}_4\text{-C}$ did not contain Fe(III) impurities. The content of carbon in $\text{LiFePO}_4\text{-C}$ was evaluated from the difference between the amount of LiFePO_4 in the powder, as estimated by titration analysis, and the total weight of the powder, assuming that the only components of the synthesized product were LiFePO_4 and carbon. We found the amount of carbon to be 6.8% (w/w), which was confirmed by TGA analysis performed by heating $\text{LiFePO}_4\text{-C}$ powder samples in O_2 flux from RT up to 700°C . The oxygen burns off the carbon and causes the complete oxidation of LiFePO_4 to $\text{Li}_3\text{Fe}_2(\text{PO}_4)_3$ and Fe_2O_3 ^{4,3}.

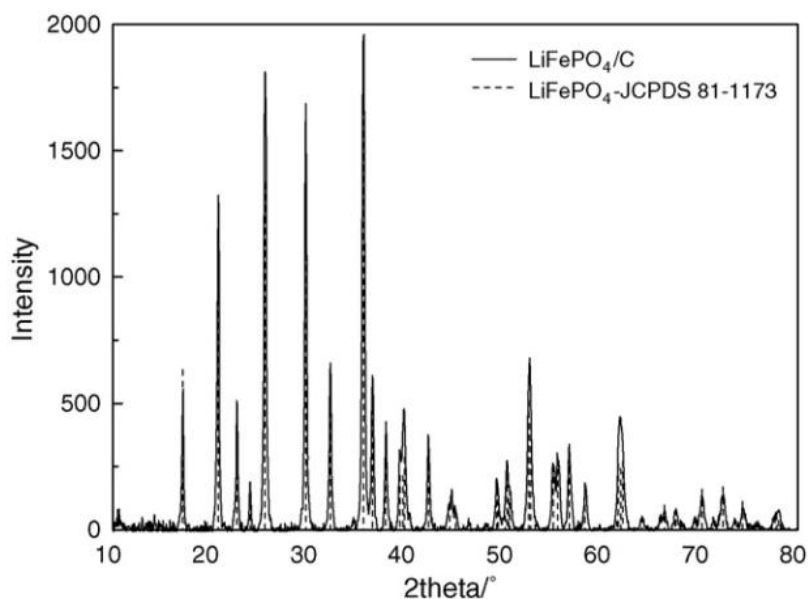


Figure 4.1. XRD pattern of LiFePO₄-C powder and standard LiFePO₄.

4.4 Electrochemical characterization

Characteristics and testing conditions of LiFePO₄-C electrodes are reported in Table 4.1. The electrochemical characterization of the LiFePO₄-C composite electrodes was first carried out in cell configuration vs. Li in standard electrolyte EC DMC LiPF₆ by conventional deep galvanostatic charge-discharge cycles; the electrode discharge rates and cyclability performance are shown in Figures. 4.2 and 4.3. Figure 4.2 shows deep discharge curves at different C-rate from 0.1C to 20C, at 30°C of fully charged electrode L2. At the lowest current density the delivered capacity is 150 mAh g⁻¹ and at 20C it approaches 80 mAh g⁻¹, the latter being one of the best capacity values delivered at such a high C-rate by nanostructured carbon-coated lithium iron phosphate^{4.4-4.6}. Figure 4.3 displays the reversible capacity of electrode L1 over 50 deep galvanostatic cycles at 0.1C and of electrode L3 over 600 cycles at 1C-rate, at 30°C, thereby demonstrating the high cycling stability of these LiFePO₄-C composite electrodes.

Table 4.1. LiFePO₄-C electrodes characteristics and testing conditions.

Electrode	LiFePO ₄	Binder (Teflon)	Conductive carbon*	C-rate	Current	Current density	Electrolyte	Temperature
	mg	mg	mg		mA	mA cm ⁻²		°C
L1	2.27 (74.6%)	0.15 (5%)	0.62 (20.4%)	C/10	0.039	0.064	EC DMC LiPF ₆	30
L2	3.26 (74.6%)	0.22 (5%)	0.89 (20.4%)	C/10- 20C	0.055- 11.08	0.09- 18.17	EC DMC LiPF ₆	30
L3	2.24 (74.6%)	0.15 (5%)	0.61 (20.4%)	1C	0.38	0.624	EC DMC LiPF ₆	30
L13	1.38 (74.6%)	0.10 (5%)	0.38 (20.4%)	C/10 C/5	0.023 0.047	0.038 0.077	PYR ₁₄ TFSI/EC DMC-LiPF ₆ 50/50 wt. %	30
L14	1.28 (74.6%)	0.09 (5%)	0.35 (20.4%)	C/10	0.022	0.036	PYR ₁₄ TFSI-LiTFSI 0.4m	60

* Sum of carbon coating derived from synthesis and SuperP.

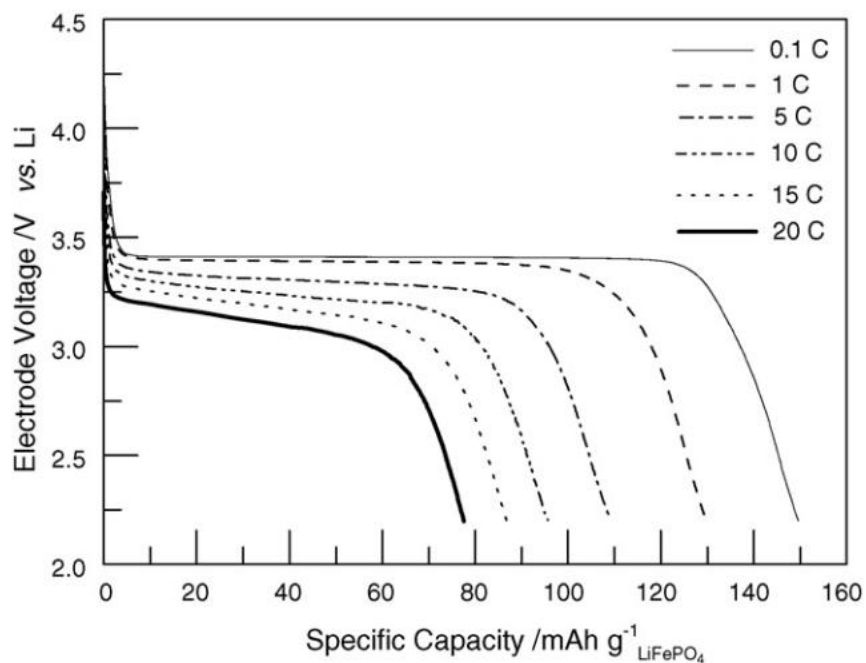


Figure 4.2. Discharge profiles of LiFePO₄-C electrode L2 at different C-rates in conventional electrolyte. Cut-off 4.3-2.2 V vs. Li.

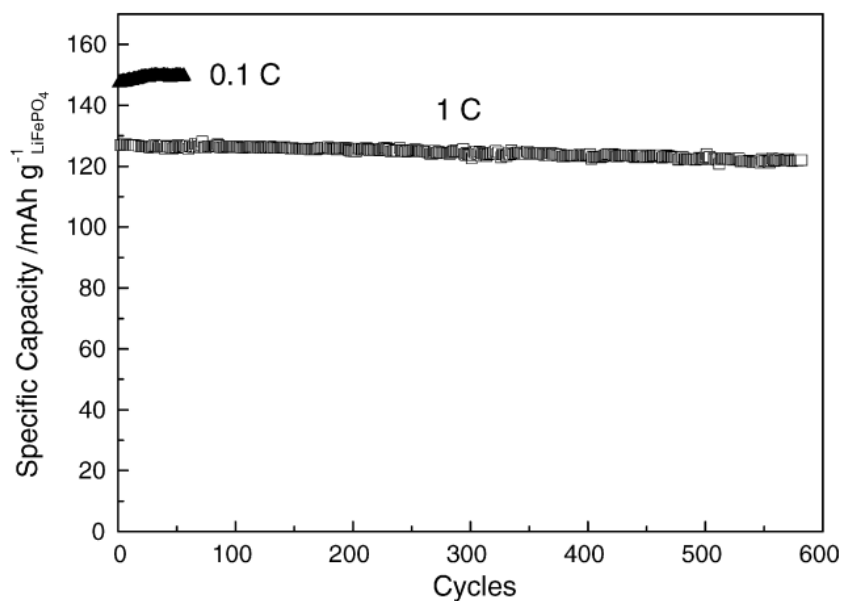


Figure 4.3. Specific discharge capacity over cycle number of the $\text{LiFePO}_4\text{-C}$ at 0.1C (electrode L1) and 1C (electrode L3) in conventional electrolyte. Cut-off 4.3-2.2 V vs. Li.

$\text{LiFePO}_4\text{-C}$ electrode L14 was tested in ionic liquid-based electrolyte $\text{PYR}_{14}\text{TFSI-LiTFSI}$ 0.4 m by galvanostatic charge/discharge cycles at $C/10$ at 60°C (Figure 4.4). The discharge capacity was stably about 130 mAh per gram of active material.

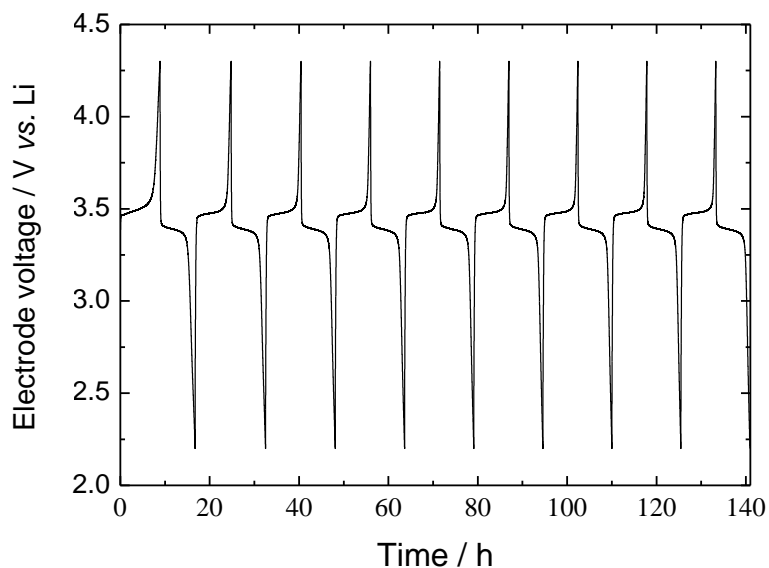


Figure 4.4. Voltage profile of $\text{LiFePO}_4\text{-C}$ L14 electrode at $C/10$ in $\text{PYR}_{14}\text{TFSI-LiTFSI}$ 0.4 m. Cut-off 4.3-2.2 V vs. Li.

Finally, $\text{LiFePO}_4\text{-C}$ electrode L13 was characterized in $\text{PYR}_{14}\text{TFSI/EC DMC-LiPF}_6$ 50%/50 wt.% mixture by deep charge/discharge galvanostatic cycles at C/5 at 30°C (Figure 4.5) after a first cycle at C/10. The discharge capacity at C/10 was 120 mAh g^{-1} LiFePO_4 and was stably about 111 mAh g^{-1} at C/5.

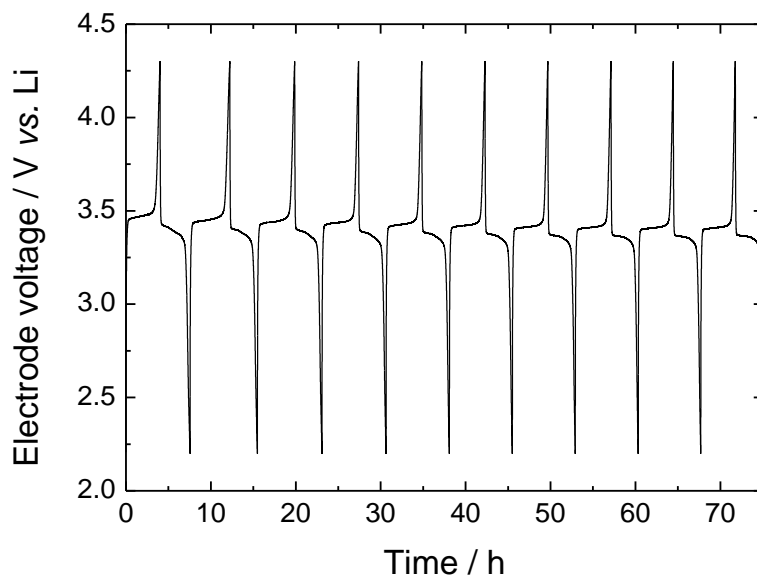


Figure 4.5. Voltage profile of $\text{LiFePO}_4\text{-C}$ electrode L13 at C/5 in $\text{PYR}_{14}\text{TFSI/EC DMC-LiPF}_6$ 50%/50 wt.%. Cut-off 4.3-2.2 V vs. Li.

4.5 Conclusions

$\text{LiFePO}_4\text{-C}$ of high purity grade was successfully synthesized by microwave accelerated sol-gel synthesis and showed excellent electrochemical performance in terms of specific capacity (up to 150 mAh g^{-1} at C-rate 0.1C) and stability (confirmed up to 600 deep charge-discharge cycles at 1C) in conventional electrolyte at 30°C . The electrode cycled stably also in $\text{PYR}_{14}\text{TFSI-LiTFSI}$ 0.4 m electrolyte with a capacity of 130 mAh g^{-1} at C/10 at 60°C . In $\text{PYR}_{14}\text{TFSI/EC DMC-LiPF}_6$ 50%/50 wt.% at 30°C the discharge capacity was 111 mAh g^{-1} .

4.6 References

- 4.1) K. Chan, W. Town. Pharmaceutical-grade ferric organic compounds, uses thereof and methods of making same, World Intellectual Property Organization Patent No WO 2007/02/2435 (2007).
- 4.2) R. Dominko, et al., *J. Electrochem. Soc.* 152 (3) (2005) A607.
- 4.3) I. Belharouack, C. Johnson, K. Amine, *Electrochem. Comm.* 7 (2005) 983.
- 4.4) Y. Zhang, et al., *Electrochim. Acta* 54 (2009) 3206–3210.
- 4.5) G.T. Kuo Fey, et al., *J. Power Sources* 189 (2009) 69–178.
- 4.6) X.-F. Guo, et al., *Solid State Ionics* (2009), doi:10.1016/j.ssi.2008.11.021.

Chapter 5

Anode materials

5.1 Graphite

Graphite is the most used active material for the anode production, due to its unique characteristics in terms of capacity, cyclability, low voltage of the lithium insertion/deinsertion process and cheapness.

5.1.1 Chemical-physical properties

Table 5.1 shows some physical and chemical properties of graphite Timrex KS-15 (from TIMCAL datasheet). Figure 5.1 shows XRD pattern of the graphite KS-15. All the peaks are related to graphite.

Table 5.1. Physical and chemical properties of graphite Timrex KS-15 (from TIMCAL datasheet) .

Ash	0.1% max
Moisture	0.5% max
Crystallite size	80 nm min
Interlayer distance	0.3354-0.3359 nm

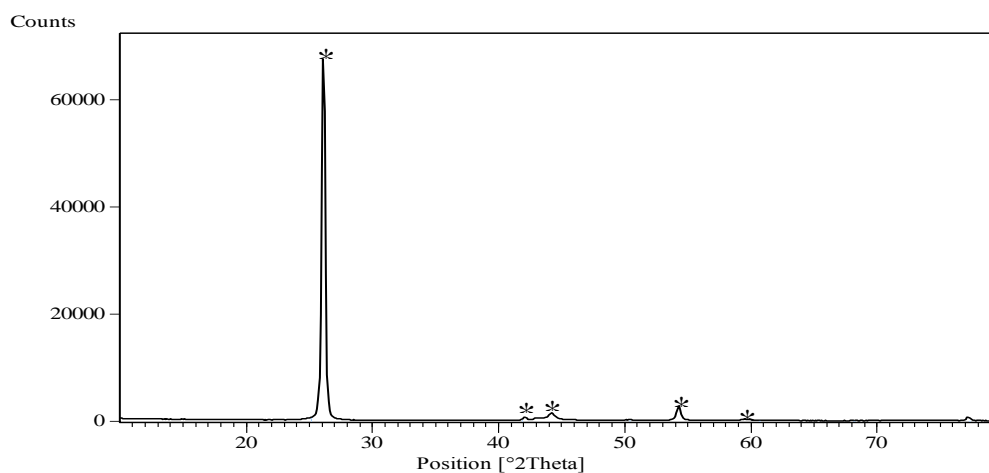


Figure 5.1. XRD pattern of graphite KS-15; (*) peaks related to graphite

5.1.2 Electrochemical characterization

Characteristics and testing conditions of the graphite electrodes are reported in Table 5.1. The electrochemical characterization of the graphite composite electrodes was first carried out in cell configuration vs. Li in standard electrolyte EC DMC LiPF₆ by conventional deep galvanostatic charge-discharge cycles at C/3; the electrode voltage profiles are shown in Figure 5.2 and rate performance are shown in Table 5.2.

Table 5.1. Graphite electrodes characteristics and testing conditions

Electrode	Graphite	Binder	Conductive carbon	C-rate	Current	Current density	Electrolyte	Temperature
	mg	mg	mg		mA	mA cm ⁻²		°C
A6	5.07 (88%)	0.40* (7%)	0.29 (5%)	C/3	0.629	1.03	EC DMC LiPF ₆	30
E5	1.88 (85.2%)	0.22** (9.8%)	0.11 (5%)	C/3	0.230	0.38	PYR ₁₄ TFSI- LiTFSI 0.4m	60
G1	1.35 (88%)	0.11** (7%)	0.08 (5%)	C/3	0.169	0.28	PYR ₁₄ TFSI/EC DMC-LiPF ₆ 50%/50 wt.%	30
TIM11	2.53 (70%)	0.72** (20%)	0.36 (10%)	C/3	0.330	0.54	90% PYR ₁₄ TFSI- LiTFSI 0.4 m + 10% VC	60
TIM12	2.32 (70%)	0.66** (20%)	0.33 (10%)	C/33 C/3	0.026 0.288	0.043 0.495	90% PYR ₁₄ TFSI- LiTFSI 0.4 m + 10% VC	60

*Teflon; **PVDF.

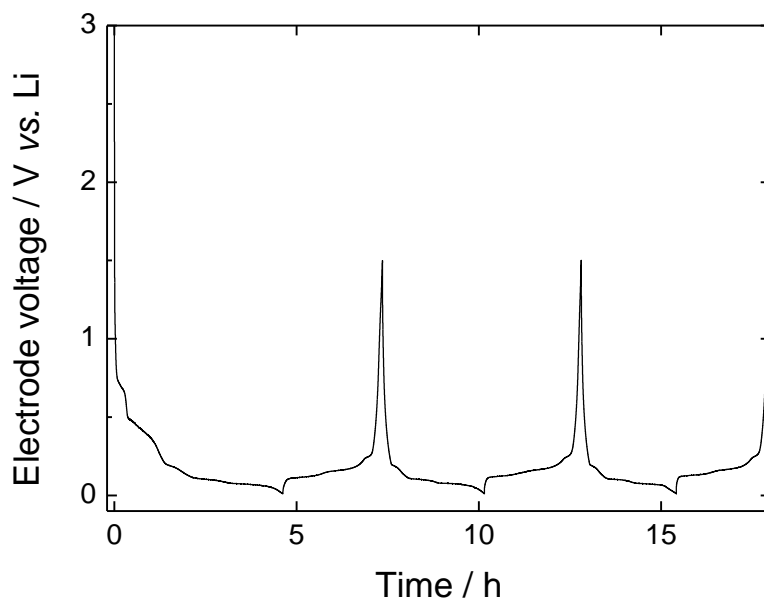


Figure 5.2. Voltage profile of graphite electrode A6 at C/3 in conventional electrolyte at 30°C. Cut-off 1.50-0.01 V vs. Li.

Table 5.2 Specific capacity and efficiency of graphite electrode A6 at C/3 in conventional electrolyte at 30°C

Cycle	Specific capacity (mAh g ⁻¹ _{graphite})		Efficiency (%)
	Charge	Discharge	
1	573	337	59
2	346	328	96
3	323	313	98
6	302	297	98
12	304	300	99
18	306	304	99
24	300	298	99

Graphite was also characterized by galvanostatic charge/discharge cycles at C/3 in electrolyte based on ionic liquid PYR₁₄TFSI-LiTFSI 0.4 m at 60°C (Figure 5.3). It is clear that the electrode had poor capacity and cycling performance in this electrolyte, in particular it had an enormous irreversible capacity in the first cycle. This behavior, reported in literature^{5.1-5.3}, is due to the cointercalation and reduction of the electrolyte (perhaps of the cation PYR₁₄⁺) without intercalation of lithium into the graphite: this phenomenon is related to lack of a stable SEI layer. Thus, it is not possible to use a graphite anode in a lithium-ion battery with this electrolyte.

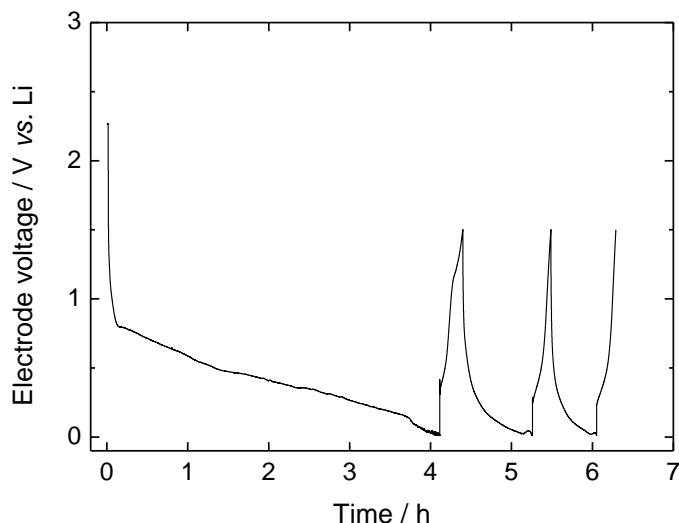


Figure 5.3. Voltage profile of graphite electrode E5 at C/3 in PYR₁₄TFSI-LiTFSI 0.4 m electrolyte at 30°C. Cut-off 1.50-0.01 V vs. Li.

Furthermore, graphite was characterized by galvanostatic charge/discharge cycles at C/3 in the ionic liquid-conventional electrolyte mixture (PYR₁₄TFSI/EC DMC-LiPF₆ 50%/50 wt.%) at 30°C in order to evaluate if the organic carbonates was sufficient to form a stable SEI layer on the graphite (Figure 5.4). Even if the performance of the graphite electrode in this electrolyte was better than PYR₁₄TFSI-LiTFSI 0.4m electrolyte, the specific capacity was low (about 100 mAh g⁻¹ in the first discharge) with a high capacity fade over cycling. The irreversible capacity in the first cycle was very big (85%). Thus, protective film is not produced and graphite electrode did not work properly in this electrolyte.

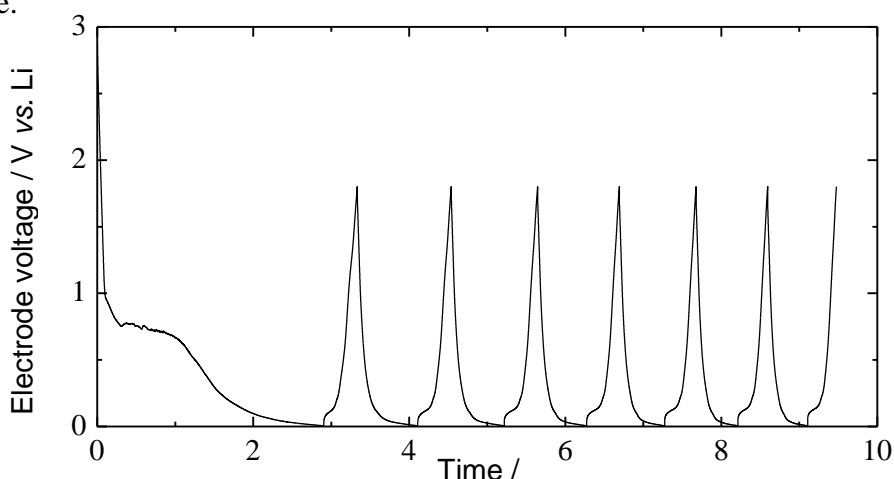


Figure 5.4. Voltage profile of graphite electrode G1 at C/3 in PYR₁₄TFSI/ EC DMC-LiPF₆ 50%/50 wt.% electrolyte at 30°C. Cut-off 1.80-0.005 V vs. Li.

Given that vinylene carbonate (VC) has been applied successfully as a SEI forming compound in the case of some ionic liquids^{5.1,5.2,5.4,5.5}, we prepared a new electrolyte adding 10 wt.% VC to 90 wt.% PYR₁₄TFSI-LiTFSI 0.4 m. We then characterized graphite-based electrodes in this electrolyte by galvanostatic charge/discharge cycles at different C-rates at 60°C. Cycling stability of graphite was confirmed by electrode T11 that performed more than 200 cycles at C/3 with an nearly stable specific capacity and efficiency (Figure 5.5 and Table 5.3). Furthermore, electrode T12 was first cycled at C/33 for 4 cycles (Figure 5.6) and then at C/3 (Figure 5.7): the use of very slow charge/discharge rates (C/33) allow to obtain the theoretic specific capacity of the graphite and also improve the performance in the next cycles at C/3 where the specific capacity rise to 150 mAh g⁻¹_{graphite}.

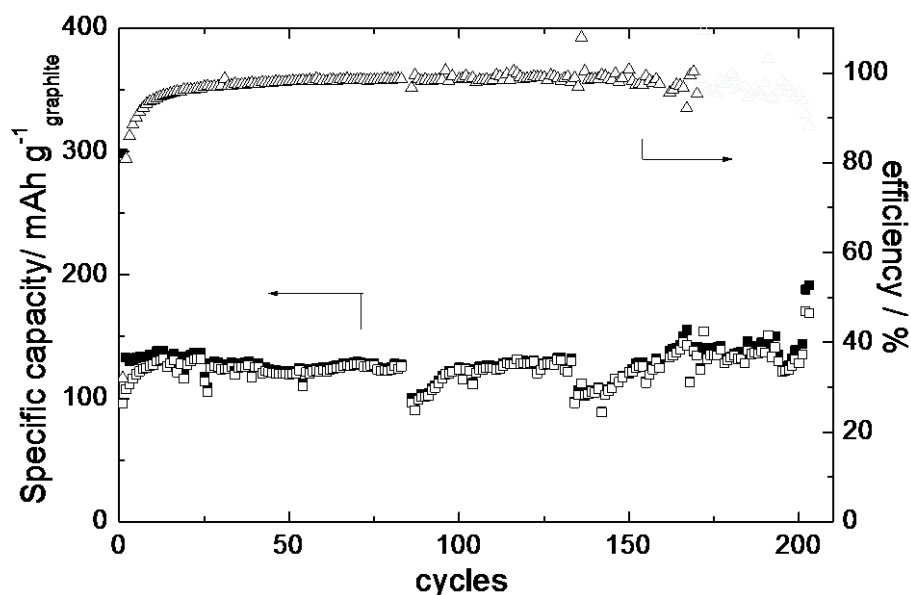


Figure 5.5. Specific discharge capacity over cycle number of graphite electrode TIM11 at C/3 in 90% PYR₁₄TFSI-LiTFSI 0.4 m + 10% VC electrolyte at 60°C. Cut-off 1.8-0.01 V vs. Li.

Table 5.3. Specific capacity and efficiency at specified cycle numbers of graphite electrode TIM11 characterized in 90% PYR₁₄TFSI-LiTFSI 0.4 m + 10% VC electrolyte at 60°C.

cycle number	Specific capacity mAh g ⁻¹ _{active}	η %
1	96	32.0
40	125	97.6
80	123	98.4
120	128	98.8
160	125	97.5
200	128	95.4

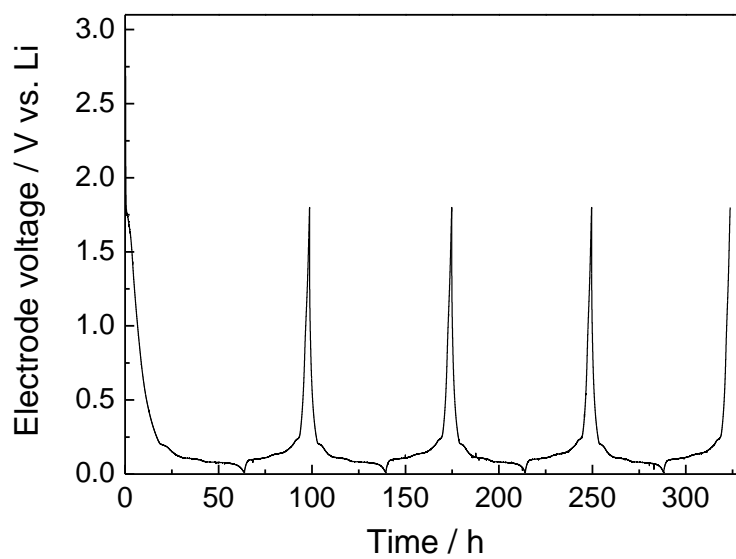


Figure 5.6. Voltage profile of graphite electrode TIM12 at C/33 in 90% PYR₁₄TFSI-LiTFSI 0.4 m + 10% VC electrolyte at 60°C. Cut-off 1.80-0.01 V vs. Li.

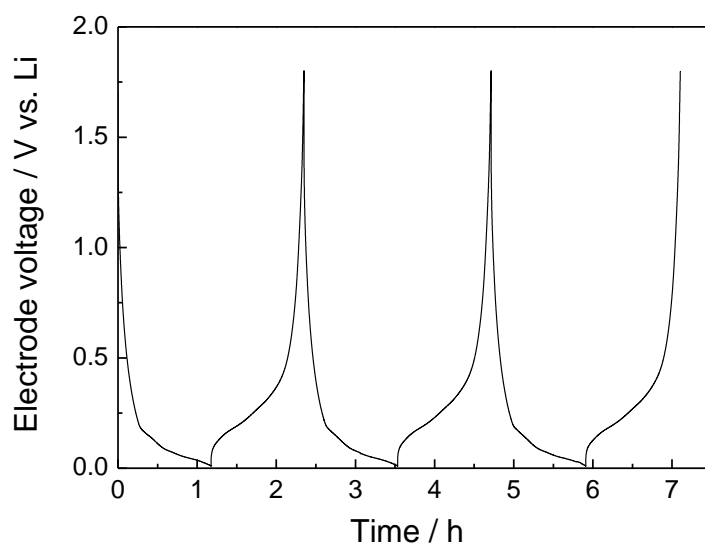


Figure 5.7. Voltage profile of graphite electrode TIM12 at C/3 in 90% PYR₁₄TFSI-LiTFSI 0.4 m + 10% VC electrolyte at 60°C. Cut-off 1.80-0.01 V vs. Li.

5.2 Titanium-based materials

Anode materials based on titanium oxides are promising candidates as alternative materials to carbonaceous anodes, especially due to their advantages in terms of safety. Indeed, the relatively high potential of Li intercalation/deintercalation (>1 V) makes the Ti-based electrodes intrinsically safer under abusive conditions compared to graphite (which has an operating voltage close to Li electroplating potential) and also utilizable in ionic liquid based electrolytes without SEI-forming additives. Two materials have been characterized: TiO_2 and its derivative $\text{Li}_4\text{Ti}_5\text{O}_{12}$.

5.2.1 TiO_2 anode

5.2.2 Chemical-physical properties

Table 5.4 shows some physical and chemical properties of TiO_2 anatase HOMBIFINE N powder (from Sachtleben datasheet).

Table 5.4. Physical and chemical properties of TiO_2 HOMBIFINE N (from Sachtleben datasheet) .

TiO₂	88%
Na	0.5%
Sulfate	0.5%
Iron	0.01%
Modification	anatase
Primary particle size (Scherrer)	< 10 nm
Specific surface area (BET)	$> 300 \text{ m}^2 \text{ g}^{-1}$
Particle size (ultrasonic, Helos, $d_{50,3}$)	~ 1 μm
Bulk density	$300 - 400 \text{ g l}^{-1}$

5.2.3 Electrochemical characterization

Characteristics and testing conditions of the TiO_2 electrodes are reported in Table 5.5. The electrochemical characterization of the TiO_2 electrodes was first carried out in cell

configuration vs. Li in standard electrolyte EC DMC LiPF₆ 1M by conventional deep galvanostatic charge-discharge cycles at C/3; the A2 electrode voltage profiles are shown in Figure 5.8. As expected, the discharge capacity in the first cycles was near to the theoretical one for Li_{0.5}TiO₂, (it was not possible to fully delithiate the TiO₂), which is typical for TiO₂ anatase^{1,11}. Then it was observed a severe capacity fade upon cyclation: at the 100th cycle the electrode delivered only 100 mAh g⁻¹ TiO₂.

Table 5.5. TiO₂ electrodes characteristics and testing conditions.

Electrode	TiO ₂	Binder (PVDF)	Conductive carbon	C-rate	Current	Current density	Electrolyte	Temperature
	mg	mg	mg		mA	mA cm ⁻²		°C
A2	1.26 (70%)	0.36 (20%)	0.18 (10%)	C/3	0.141	0.231	EC DMC LiPF ₆	30
P2*	2.22 (76%)	0.35 (12%)	0.35 (12%)	C/5	0.149	0.244	EC DMC LiPF ₆	30
A5	0.76 (70%)	0.22 (20%)	0.11 (10%)	C/5	0.053	0.087	PYR ₁₄ TFSI- LiTFSI 0.4m	60
A7	1.27 (70%)	0.36 (20%)	0.18 (10%)	C/5	0.085	0.139	PYR ₁₄ TFSI/EC DMC-LiPF ₆ 50%/50 wt.%	30

* Pressed.

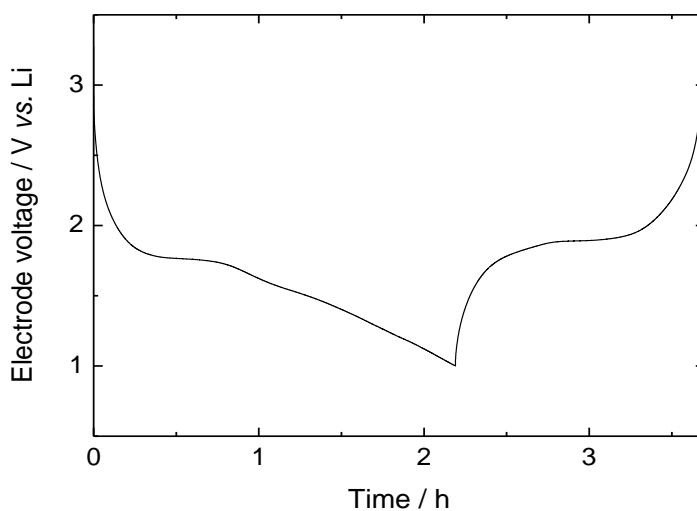


Figure 5.8. Voltage profile of TiO₂ electrode A2 at C/3 in conventional electrolyte at 30°C. Cut-off 3.0-1.0 V vs. Li.

The electrode P2 was pressed before the characterization in standard electrolyte EC DMC LiPF₆ 1M by deep galvanostatic charge-discharge cycles at C/5 at 30°C (Figure 5.9). The performance, in terms of cycling stability, irreversible capacity in the first cycle and efficiency was significantly increased (the electrode still delivered 160 mAh g⁻¹_{TiO₂} at 100th cycle) because of the higher mechanical strength of the electrode.

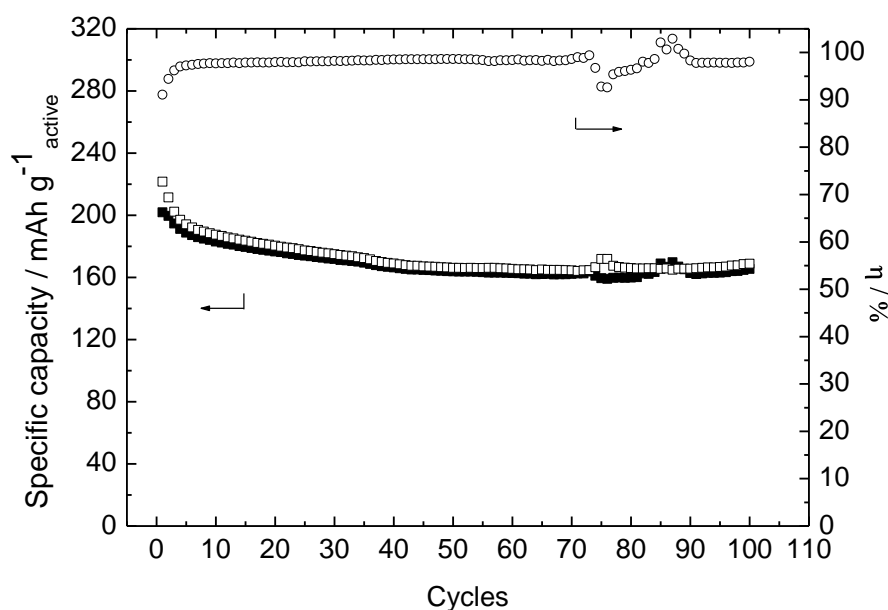


Figure 5.9. Specific discharge capacity and efficiency over cycle number of TiO₂ electrode P2 at C/5 in EC DMC LiPF₆ electrolyte at 30°C; (□) charge, (■) discharge. Cut-off 3.0-1.0 V vs. Li.

TiO₂ electrode A5 was characterized by galvanostatic charge/discharge cycles at C/5 in electrolyte based on ionic liquid PYR₁₄TFSI-LiTFSI 0.4 m at 60°C (Figure 5.10). Specific capacity and cycling performance in this electrolyte are similar to that in conventional electrolyte.

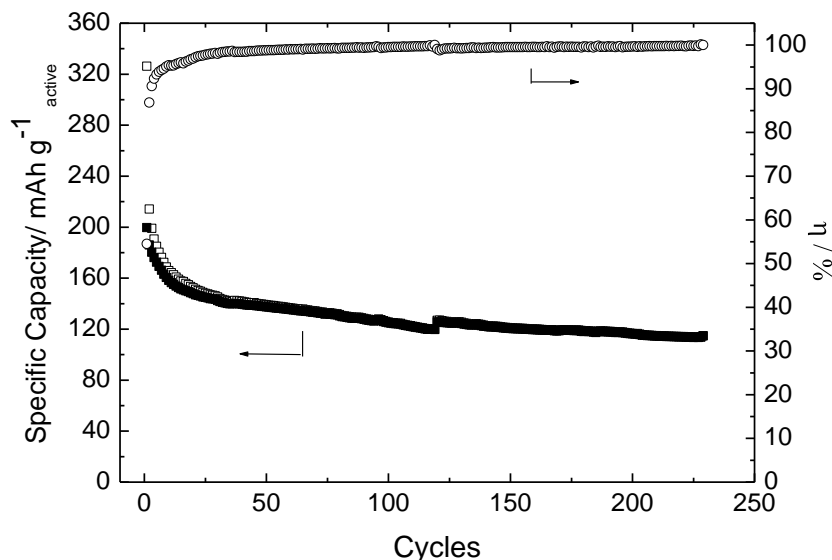


Figure 5.10. Specific discharge capacity and efficiency over cycle number of TiO₂ electrode A5 at C/5 in PYR₁₄TFSI-LiTFSI 0.4 electrolyte at 60°C; (□) charge, (■) discharge. Cut-off 3.0-1.0 V vs. Li.

Furthermore, TiO₂ electrode A7 was characterized by galvanostatic charge/discharge cycles at C/5 in the ionic liquid-conventional electrolyte mixture (PYR₁₄TFSI/EC DMC-LiPF₆ 50%/50 wt.%) at 30°C (Figure 5.11). The performance was similar to that in other electrolytes.

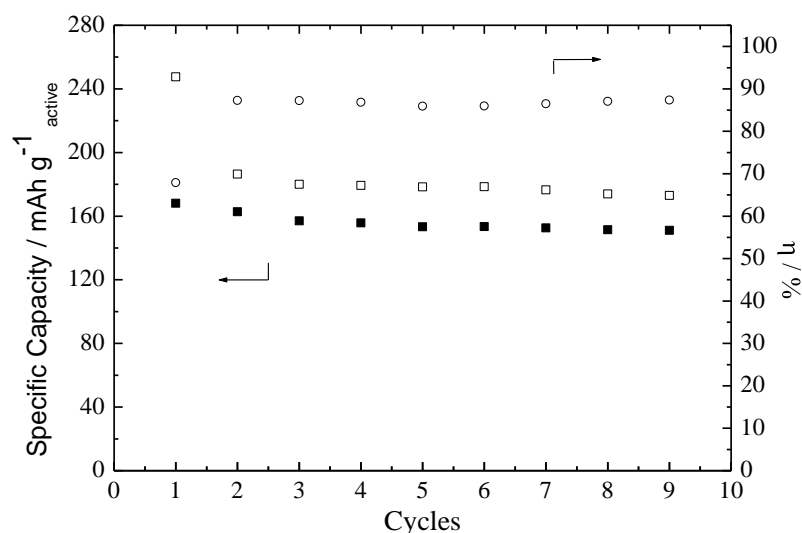


Figure 5.11. Specific discharge capacity and efficiency over cycle number of TiO₂ electrode A7 at C/5 in PYR₁₄TFSI/EC DMC-LiPF₆ 50%/50 wt.% electrolyte at 30°C; (□) charge, (■) discharge. Cut-off 3.0-1.0 V vs. Li.

5.2.4 $\text{Li}_4\text{Ti}_5\text{O}_{12}$

5.2.5 Chemical-physical properties

Table 5.6 shows some physical and chemical properties of $\text{Li}_4\text{Ti}_5\text{O}_{12}$ (from Sigma-Aldrich datasheet). Figure 5.12 shows XRD pattern of the commercial product as received and after some heat treatments: after drying at 200°C under dynamic vacuum overnight and after calcinations at 850°C for 5 hours in air, in order to evaluate the structural effects of these treatments. No particular differences are noticeable. All the peaks are related to $\text{Li}_4\text{Ti}_5\text{O}_{12}$ (with a minor impurity of Li_2TiO_3). The electrochemical characterization was performed on electrodes made from the powder dried 200°C under dynamic vacuum overnight.

Table 5.6. Physical and chemical properties of $\text{Li}_4\text{Ti}_5\text{O}_{12}$ (from Sigma-Aldrich datasheet).

Assay	>99%
Form	nanopowder
Particle size	<100 nm (BET) <100 nm (TEM)
Specific surface area	32.6 m^2/g (BET)

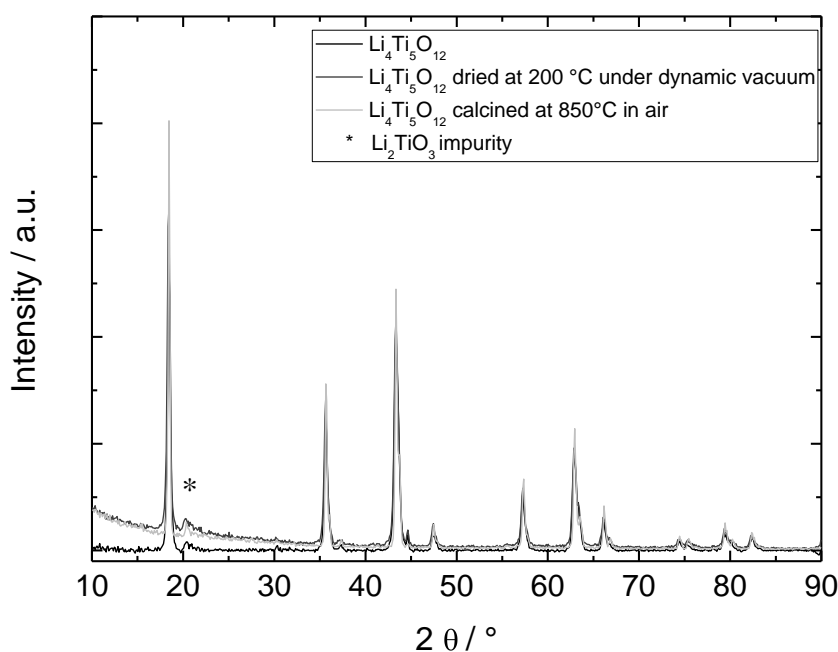


Figure 5.12. XRD pattern of $\text{Li}_4\text{Ti}_5\text{O}_{12}$

5.2.6 Electrochemical characterization

Characteristics and testing conditions of the $\text{Li}_4\text{Ti}_5\text{O}_{12}$ electrodes are reported in Table 5.7. The electrochemical characterization of the $\text{Li}_4\text{Ti}_5\text{O}_{12}$ electrodes was first carried out in cell configuration vs. Li in standard electrolyte EC DMC LiPF_6 1M by conventional deep galvanostatic charge-discharge cycles at C/3, using electrodes with different binders, compositions, with or without pressing.

Table 5.7. $\text{Li}_4\text{Ti}_5\text{O}_{12}$ electrodes characteristics and testing conditions.

Electrode	$\text{Li}_4\text{Ti}_5\text{O}_{12}$	Binder	Conductive carbon	C-rate	Current	Current density	Electrolyte	Temperature
	mg	mg	mg		mA	mA cm^{-2}		$^{\circ}\text{C}$
T21	2.36 (80%)	0.29* (10%)	0.29 (10%)	C/10	0.041	0.068	EC DMC LiPF_6	30
TF1 ⁺	1.51 (70%)	0.43** (20%)	0.21 (10%)	C/3	0.088	0.144	EC DMC LiPF_6	30
TP2 ⁺	1.44 (80%)	0.18** (10%)	0.18 (10%)	C/3	0.084	0.138	EC DMC LiPF_6	30
TP3 ⁺	1.05 (80%)	0.13** (10%)	0.13 (10%)	5C 20C	0.918 3.675	1.505 6.02	EC DMC LiPF_6	30
T12	1.62 (80%)	0.20* (10%)	0.20 (10%)	C/10	0.028	0.046	$\text{PYR}_{14}\text{TFSI}$ - LiTFSI 0.4m	60
TP5 ⁺	1.18 (76%)	0.19** (12%)	0.19 (12%)	1C	0.207	0.339	$\text{PYR}_{14}\text{TFSI}$ - LiTFSI 0.4m	60
TP6 ⁺	1.25 (80%)	0.16** (10%)	0.16 (10%)	1C	0.219	0.359	$\text{PYR}_{14}\text{TFSI/EC}$ DMC- LiPF_6 50%/50 wt. %	30

⁺ Pressed; *Teflon; **PVDF.

Electrode T21 had Teflon binder (10%): the specific discharge capacity and efficiency over cycle number is shown in Figure 5.13. The cycling stability was not satisfactory. Electrode TF1 and TP2 had PVDF binder (20% and 10%, respectively): in Figure 5.14 are shown the voltage profiles of the first galvanostatic charge/discharge cycle

at C/3 in which is possible recognize that the low-binder percentage electrode has a more plateau-like profile, related to a lower electrode resistance. Indeed, as PVDF binder is an electrical insulator, it contributes negatively to the electrode conductance. Moreover, electrode TP2 show good cycling stability for over 150 cycles (Figure 5.15). In conclusion, PVDF binder was more suitable for producing $\text{Li}_4\text{Ti}_5\text{O}_{12}$ -based electrode to be used in EC DMC- LiPF_6 electrolyte.

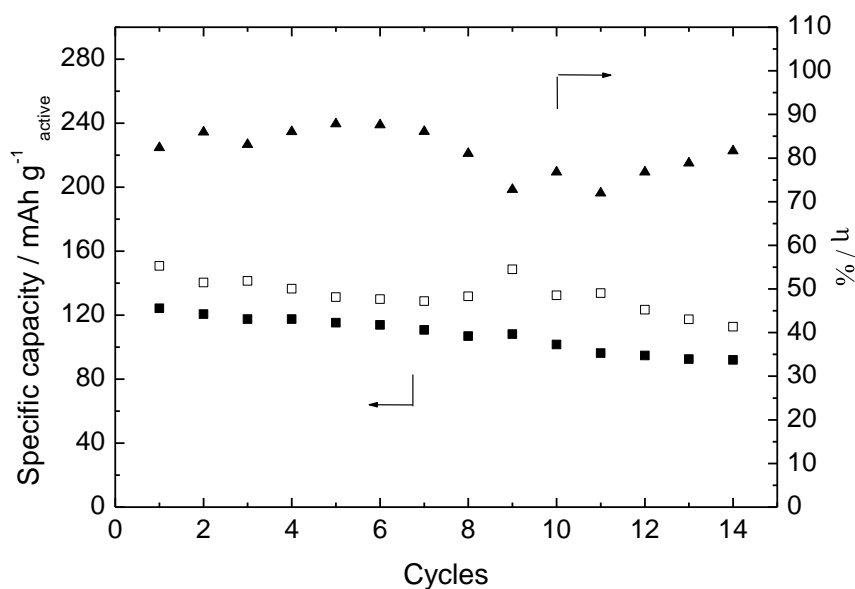


Figure 5.13. Specific discharge capacity and end efficiency over cycle number of $\text{Li}_4\text{Ti}_5\text{O}_{12}$ electrode T21 at C/10 in EC DMC LiPF_6 electrolyte at 30°C; (□) charge, (■) discharge. Cut-off 2.2-1.0 V vs. Li.

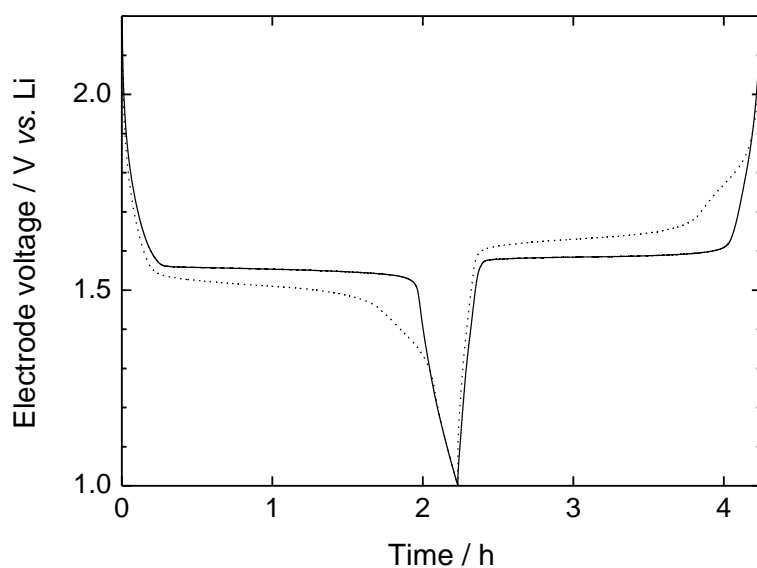


Figure 5.14. Voltage profile of $\text{Li}_4\text{Ti}_5\text{O}_{12}$ electrodes TF1 (···) and TP2 (—) at C/3 in conventional electrolyte at 30°C. Cut-off 2.2-1.0 V vs. Li.

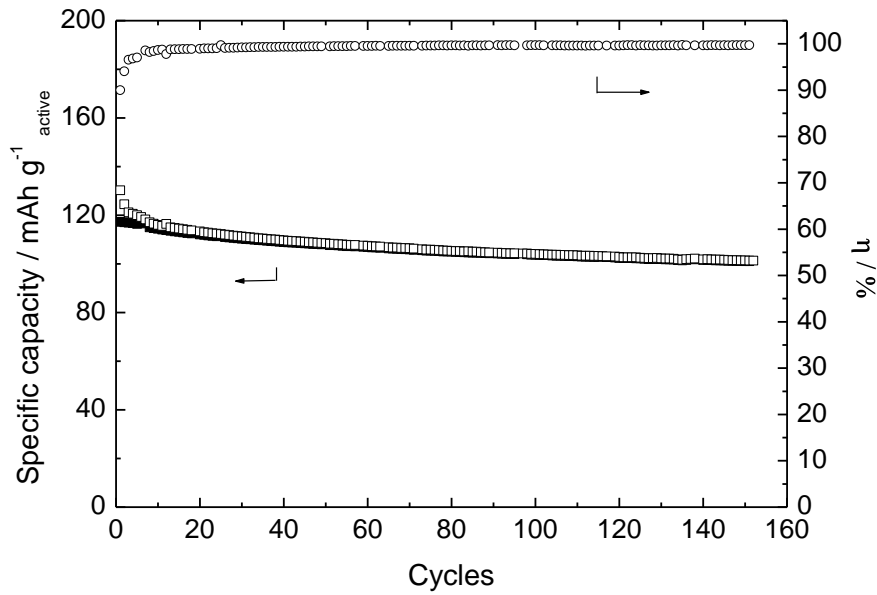


Figure 5.15. Specific discharge capacity end efficiency over cycle number of $\text{Li}_4\text{Ti}_5\text{O}_{12}$ electrode TP2 at C/3 in EC DMC LiPF_6 electrolyte at 30°C ; (\square) charge, (\blacksquare) discharge. Cut-off 2.2-1.0 V vs. Li.

To evaluate the performance of $\text{Li}_4\text{Ti}_5\text{O}_{12}$ at high C-rates, electrode TP3 was tested by deep galvanostatic charge discharge cycles in conventional electrolyte at 5C and 20C: the results are shown in figures 5.16 and 5.17. It worth noting that, even at the high C-rate of 20C, the electrodes cycled stably for about 2250 cycles losing only 20% of capacity and with 100% of efficiency.

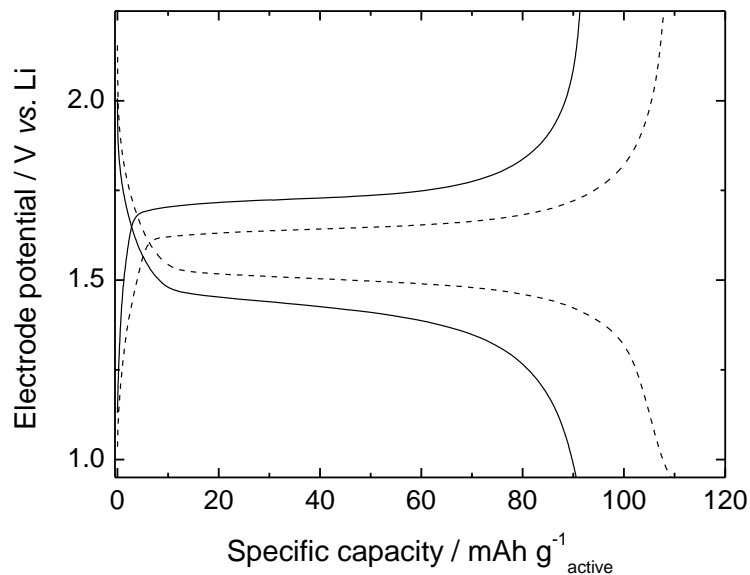


Figure 5.16. Voltage profile of $\text{Li}_4\text{Ti}_5\text{O}_{12}$ electrode TP3 at 5C (---) and 20C (—) in conventional electrolyte at 30°C . Cut-off 2.2-1.0 V vs. Li.

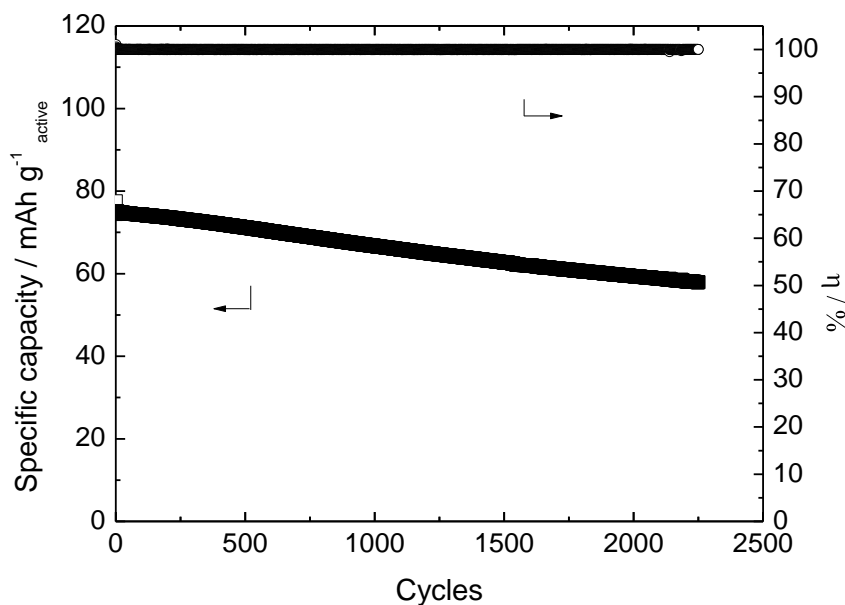


Figure 5.17. Specific discharge capacity end efficiency over cycle number of $\text{Li}_4\text{Ti}_5\text{O}_{12}$ electrode TP3 at 20C in EC DMC LiPF_6 electrolyte at 30°C; (\square) charge, (\blacksquare) discharge. Cut-off 2.2-1.0 V vs. Li.

Electrodes T12 (Teflon binder) and TP5 (PVDF binder) were characterized by galvanostatic charge/discharge cycles at C/10 and 1C, respectively, in electrolyte based on ionic liquid $\text{PYR}_{14}\text{TFSI-LiTFSI}$ 0.4 m at 60°C (figures 5.18 and 5.19). In this electrolyte, specific capacity and cycling performance of electrode made with Teflon binder were better.

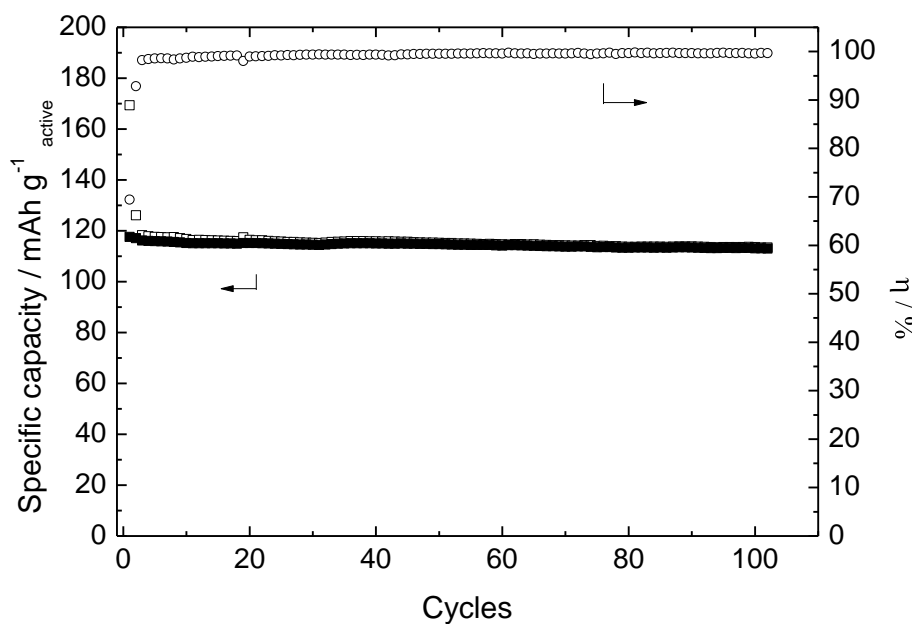


Figure 5.18. Specific discharge capacity end efficiency over cycle number of $\text{Li}_4\text{Ti}_5\text{O}_{12}$ electrode T12 at C/10 in $\text{PYR}_{14}\text{TFSI-LiTFSI}$ 0.4 electrolyte at 60°C; (\square) charge, (\blacksquare) discharge. Cut-off 2.2-1.0 V vs. Li.

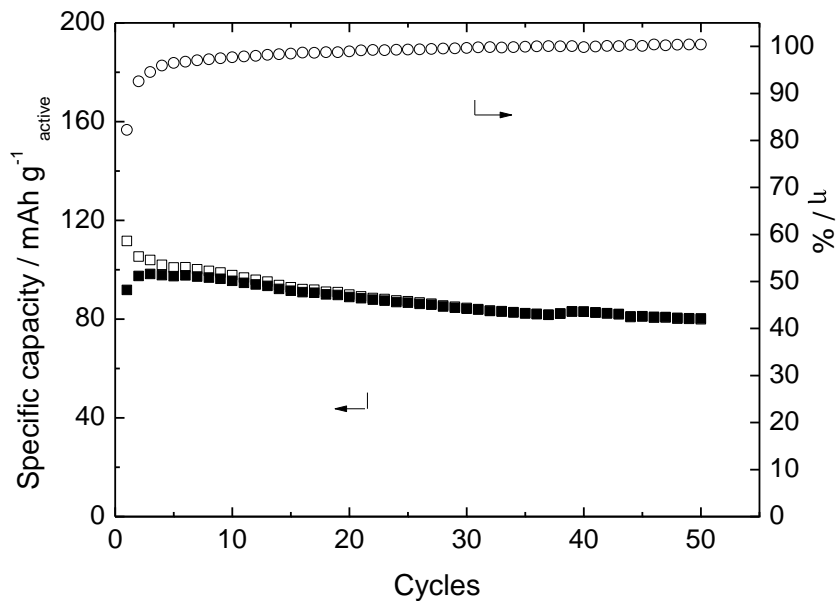


Figure 5.18. Specific discharge capacity and efficiency over cycle number of $\text{Li}_4\text{Ti}_5\text{O}_{12}$ electrode TP5 at 1C in $\text{PYR}_{14}\text{TFSI-LiTFSI}$ 0.4 electrolyte at 60°C ; (\square) charge, (\blacksquare) discharge. Cut-off 2.2-1.0 V vs. Li.

Besides, $\text{Li}_4\text{Ti}_5\text{O}_{12}$ electrode TP6 (PVDF binder) was characterized by galvanostatic charge/discharge cycles at C/5 in the ionic liquid-conventional electrolyte mixture ($\text{PYR}_{14}\text{TFSI/EC DMC-LiPF}_6$ 50%/50 wt.%) at 30°C (Figure 5.19). The performance was good and similar to that in conventional electrolyte.

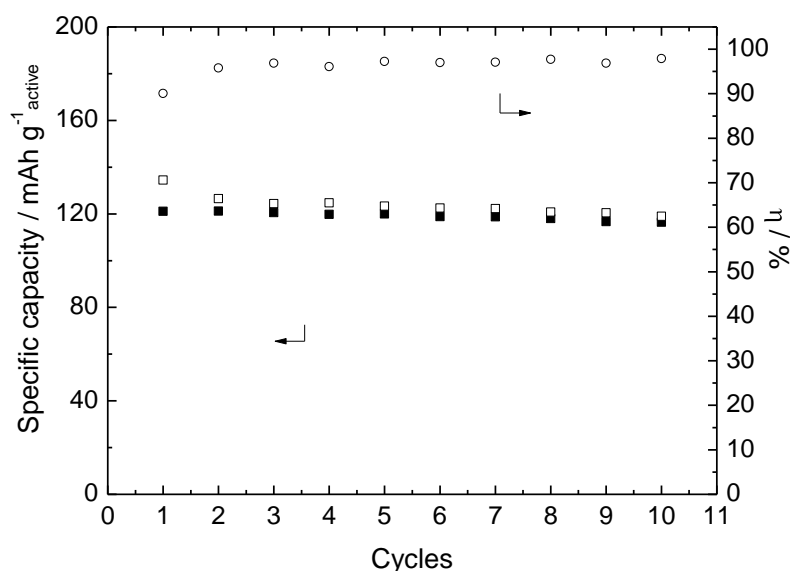


Figure 5.19. Specific discharge capacity and efficiency over cycle number of $\text{Li}_4\text{Ti}_5\text{O}_{12}$ electrode TP6 at 1C in $\text{PYR}_{14}\text{TFSI/EC DMC-LiPF}_6$ 50%/50 wt.% electrolyte at 30°C ; (\square) charge, (\blacksquare) discharge. Cut-off 2.2-1.0 V vs. Li.

5.3 SnCo

The demand to enhance the performance of lithium-ion batteries has stimulated the development of tin-based anode because Sn can intercalate lithium up to Li/Sn atomic ratio of 4.4 with a theoretical specific capacity of 993 mAh g^{-1} , whereas graphite gives 372 mAh g^{-1} . Though tin is very attractive for its high specific capacity, low-cost and availability, the drastic volume change (about 300%) between Sn and $\text{Li}_{4.4}\text{Sn}$ causes electrode pulverization and loss of electric contact that is responsible for poor electrode cycle life. It has also been reported that all-metal structured electrodes manufactured using nanowire technology^{5.6-5.9} or amorphous materials^{5.10} display enhanced performance with respect to conventional electrodes even in terms of cycling stability. So amorphous SnCo nanowire electrodes were synthesized and characterized as anodes. They were also compared with a similar material previously synthesized^{5.11-5.12}.

5.3.1 Synthesis

Amorphous SnCo alloy nanowires (NWs) were grown inside the channels of polycarbonate membranes by potentiostatic codeposition of the two metals, as in Ref. 1.14. Tin-cobalt alloy was electrodeposited inside the channels of a commercially available Whatman Cyclopore™ polycarbonate porous template that is a $20 \mu\text{m}$ thick track etched membrane with cylindrical pores of about 200 nm and a pore density in the order of 10^{12} m^{-2} . A gold film of few nanometers was sputtered on one side of the membrane before electrodeposition in order to make it conductive. The membrane was then glued with conductive paste to a holder specially designed for deposition of the Cu current collector and, hence, the tin-cobalt alloy NWs. The electrodepositions were carried out in a three electrode cell, with a Standard Calomel Electrode (SCE) as reference electrode and a platinum wire as counter electrode. The composition of the aqueous baths for deposition of the Cu current collector (bath 1) and the SnCo alloy (bath 2) was: CuSO_4 $2.0 \times 10^{-1} \text{ M}$ and H_3BO_3 $1.0 \cdot 10^{-1} \text{ M}$ at pH 3.0 (bath 1) and SnSO_4 $2.0 \cdot 10^{-2} \text{ M}$, CoSO_4 $5.0 \cdot 10^{-3} \text{ M}$, Na_2SO_4 $2.0 \cdot 10^{-1} \text{ M}$ and sodium gluconate (chelating agent) $2.0 \cdot 10^{-1} \text{ M}$, at pH 4.6 (bath 2). A $15 \mu\text{m}$ thick Cu current collector was deposited under galvanostatic conditions at 20 mA cm^{-2} for

1 h at room temperature. The deposition of the SnCo alloy was carried out under potentiostatic conditions at -1 V (vs. SCE) and at 60 °C for 1 h; the SnCo NW arrays were washed in water and then in chloroform to completely dissolve the polycarbonate template membrane.

5.3.2 Chemical-physical properties

The results of EDS and ICP analyses of the synthesized SnCo-PM alloy after template chemical dissolution indicate that the Sn molar fraction was 0.76 and the Sn loading per cm^2 of NW array was 1.1 mg. Figure 5.20 shows an XRD pattern of the electrodeposited SnCo-PM after template dissolution. Given that all the intense diffraction peaks are due to the Cu current collector and only two very small, broad peaks at 30.64° and 32.92° are attributable to Sn or to an SnCo phase^{5.13-5.14}, the XRD analysis demonstrates that the electrodeposited SnCo alloy is amorphous.

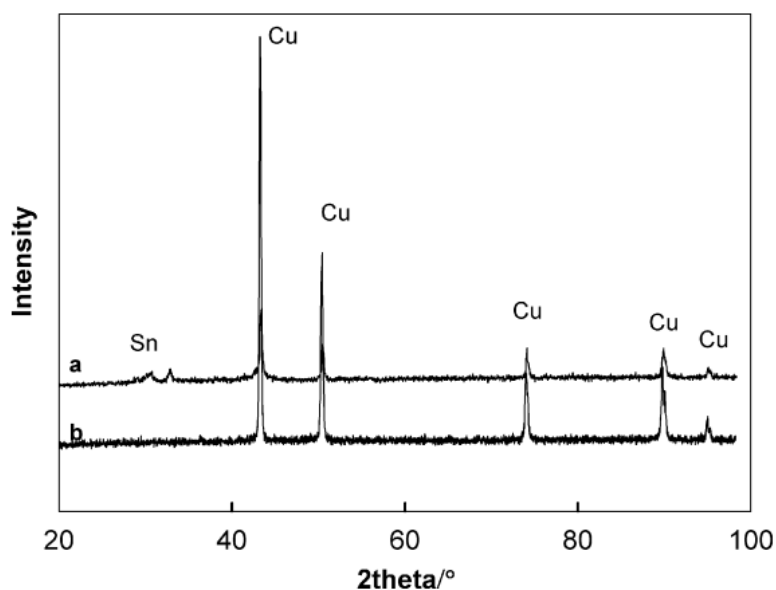


Figure 5.20. Typical XRD pattern of SnCo alloy NWs after template removal (a). The XRD pattern of current collector alone is reported (b).

Figure 5.21 displays the SEM images of the SnCo-PM after template dissolution and shows that the NWs have a diameter of 0.2 μm and are 15 μm high. The population of these SnCo-PM is less dense than that of amorphous SnCo NWs (Sn molar fraction 0.64)

grown inside alumina membranes, where the NWs had a diameter of $0.35\ \mu\text{m}$ and were $3\ \mu\text{m}$ high after template dissolution^{5.11-5.12}. Differences in the template morphology must be carefully considered for application in Li-ion battery of SnCo NWs prepared by the template method; Figure 5.22 shows the SEM image of the SnCo-AM after alumina dissolution for comparison.

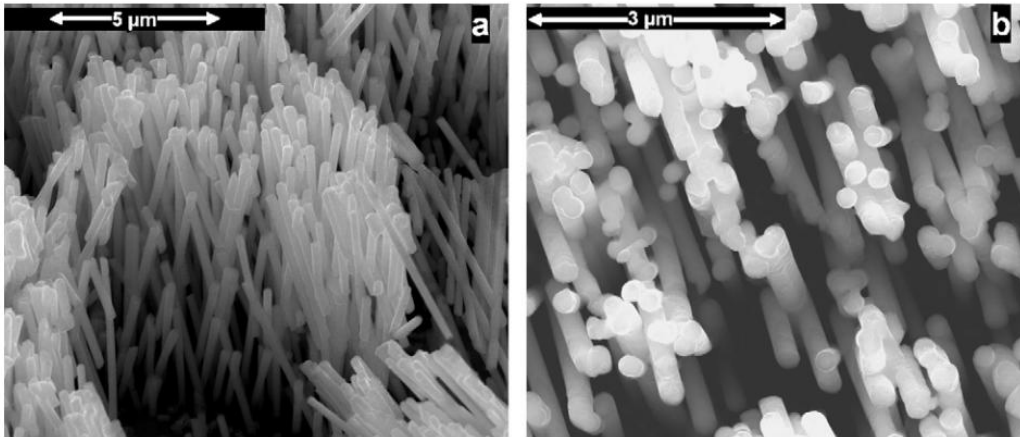


Figure 5.21 SEM images of SnCo-PM after PM template dissolution at different magnifications. (a) Cross-section view, (b) top-down view.

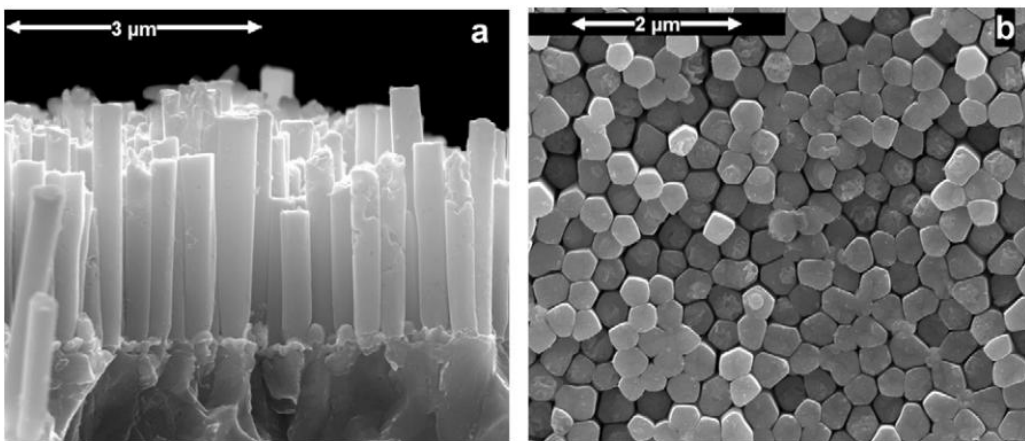


Figure 5.22. SEM images of SnCo-AM after AM template dissolution at different magnifications. (a) Cross-section view, (b) top-down view.

5.3.3 Electrochemical characterization

The electrochemical characterization of the SnCo electrodes was carried out in cell configuration *vs.* Li in standard electrolyte EC DMC LiPF₆ 1M by conventional deep galvanostatic charge-discharge cycles. Figure 5.23 shows charge-discharge voltage profiles of the SnCo-PM electrode tested by deep galvanostatic cycles at 1 C-rate in the potential range 2.00-0.02 V, and Figure 5.24 displays the electrode specific capacity values and cycle efficiency over 35 lithiation-delithiation cycles. The electrode specific capacity referred to the tin mass was almost constant over cycling and approaches the Sn theoretical capacity, indicating that the Li₂₂Sn₅ alloy phase has been formed and that all the tin in the electrode is electrochemically active. Furthermore XRD measurement performed on cycled electrode (not reported here) demonstrated that the amorphous nature of the electrode material was maintained upon cycling. It is worth noting that the SnCo-PM electrode performs significantly better than recently reported tin-based electrodes^{5,15-5,23} both in terms of specific capacity and cycling stability, and that the capacity of this electrode is about 1.0 mAh cm⁻², which is a very high value for nanowire technology^{5,24}. These SnCo-PM electrodes display significantly better cycling stability than the SnCo-AM NW electrodes. Some voltage profiles over 20 galvanostatic lithiation-delithiation cycles at 0.1 C of the latter electrode are reported in Figure 5.25. The figure shows that the SnCo-AM electrode delivers constant values of specific capacity (corresponding to ca. 900 mAh g⁻¹ of Sn) over the first 12 cycles; an abrupt capacity fade occurs in a few cycles after this initial stability.

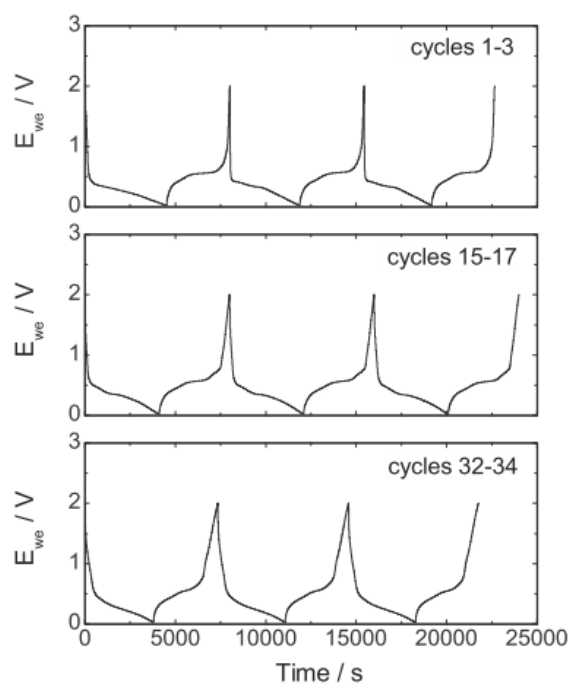


Figure 5.23. Voltage profiles of some representative cycles of a SnCo-PM electrode cycled at 1 C and 30 °C.

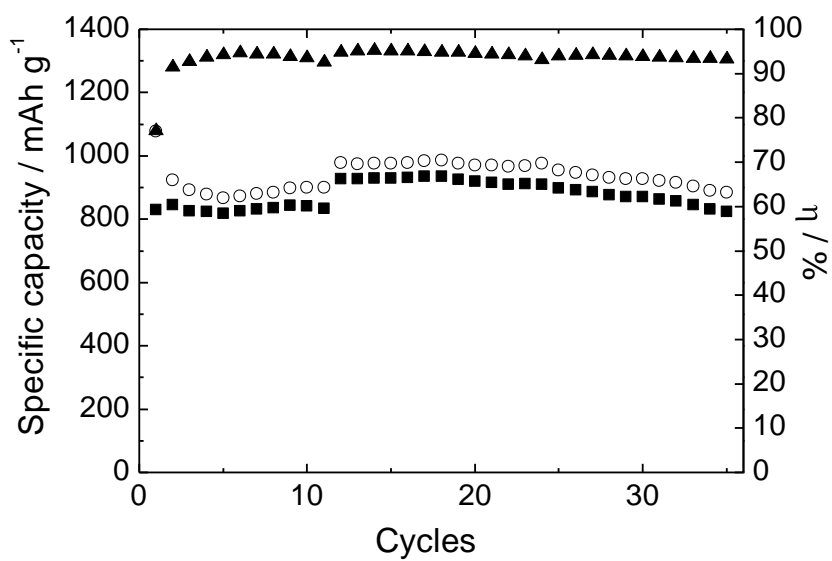


Figure 5.24. Specific capacity and efficiency vs. cycle number of an SnCo-PM electrode cycled at 1C and 30°C. (○) Lithiation, (■) delithiation and (▲) efficiency.

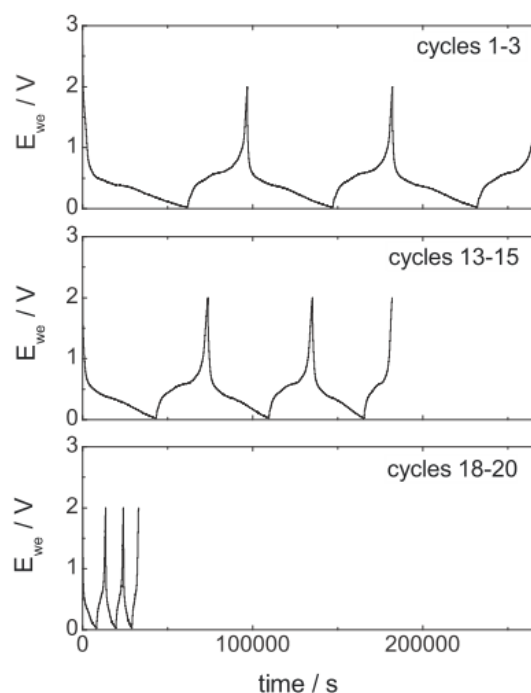


Figure 5.25. Voltage profiles of some representative cycles of an SnCo-AM electrode cycled at 0.1 C, 30°C.

The effect of lithiation/delithiation cycles on the SnCo NW structures is demonstrated by the SEM images of the electrodes after cycling shown in Figures 5.26 and 5.27 for the SnCo-PM and SnCo-AM electrodes, respectively. The nanowire structure of the SnCo-PM NW electrodes, unlike that of the SnCo-AM electrodes, is still recognizable after repeated cycles, thus indicating that the morphology of the SnCo-PM effectively offsets the enormous deformation that occurs in full lithiation of tin (4.4 Li/Sn), even though several wires became a compact mass of deformed porous structures. The SEM magnification in Figure 5.26b gives a view of the deformation process of a single SnCo-PM nanowire. Comparison with the SEM images of the SnCo-AM cycled electrodes demonstrates that NW size and distance are key parameters for durability of these electrode structures. The lack of free space causes the compaction of the nanowires and the increase of the expansion in the axial direction with consequent formation of horizontal cracks that are deleterious for maintaining contact with the current collector and, hence, for the electrochemical cycling stability of the electrode. The zoomed image in Figure 5.27b shows that the SnCo-AM nanowires are deformed with lamellar extrusions caused by the extreme compression of the nanowires. The mechanical stress is not properly absorbed by these NW structures and the electrical contact with the current collector is compromised after a few cycles.

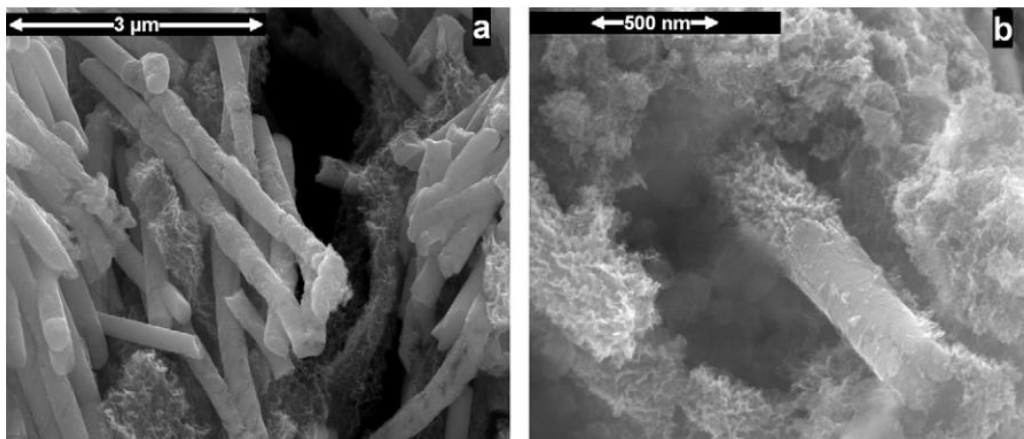


Figure 5.26. SEM images of cycled SnCo-PM electrode at different magnifications.

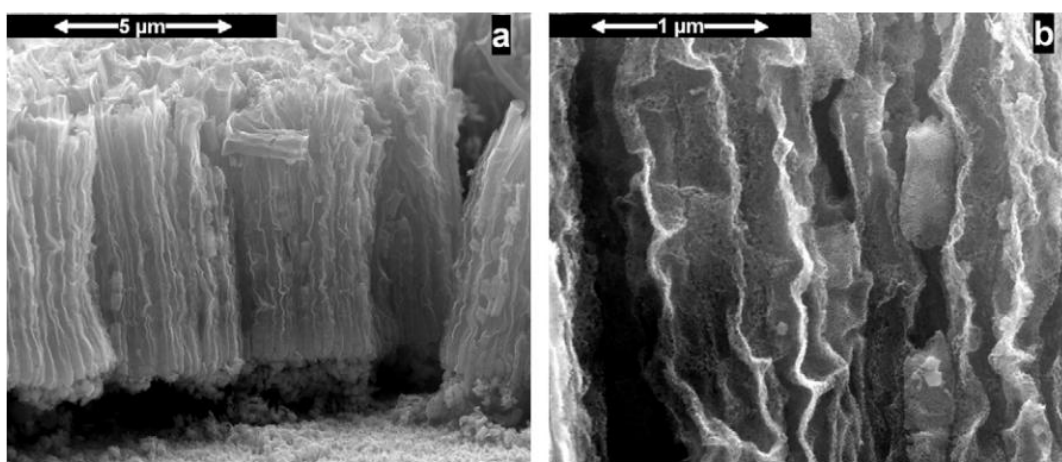


Figure 5.27. SEM images of cycled SnCo-AM electrode at different magnifications.

5.4 Conclusions

In order to assemble lithium-ion batteries with $\text{LiFePO}_4\text{-C}$ cathode, some commercial anode materials were characterized in different electrolytes: titanium-based anodes, with the appropriate binder, appeared usable in all electrolytes, graphite only in conventional electrolyte and 90 wt.% $\text{PYR}_{14}\text{TFSI-LiTFSI}$ 0.4 m + 10 wt.% VC.

Moreover, an array of amorphous SnCo nanowires fabricated by template electrodeposition in polycarbonate membrane template yielded electrodes capable of reversibly intercalating lithium up to $\text{Li}_{22}\text{Sn}_5$ for 35 cycles with an elevated capacity per cm^2 (ca. 1 mAh cm^{-2}) in conventional electrolyte. This promising result is related to a

morphology of the electrode array that features free space among nanowires capable of buffering the mechanical stress of the lithiation–delithiation process.

5.5 References

- 5.1) M. Holzappel, C. Jost, P. Novak, *Chem. Commun.* (2004) 2098
- 5.2) A. Lewandowski, A. Swiderska-Mocek, *Journal of Power Sources* 194 (2009) 502-507
- 5.3) H. Zheng, G. Liu, V. Battaglia, *J. Phys. Chem. C* 114 (2010) 6182–6189
- 5.4) G.B. Appetecchi, M. Montanino, A. Balducci, S. F. Lux, M. Winter, S. Passerini, *Journal of Power Sources* 192 (2009) 599–605
- 5.5) H. Zheng, K. Jiang, T. Abe, Z. Ogumi, *Carbon* 44 (2006) 203.
- 5.6) C.K. Chan, H. Peng, G. Liu, K. McIlwrath, X.F. Zhang, R.A. Huggins, Y. Cui, *Nature Nanotechnology* 3 (2008) 31–35.
- 5.7) J. Hassoun, S. Panero, P. Simon, L. Taberna, B. Scrosati, *Advanced Materials* 19 (2007) 1632–1635.
- 5.8) L. Bazin, S. Mitra, P.L. Taberna, P. Poizot, M. Gressier, M.J. Menu, A. Barnabé, P. Simon, J.-M. Tarascon, *Journal of Power Sources* 188 (2009) 578–582.
- 5.9) J.-H. Kim, S. Khanal, M. Islam, A. Khatri, D. Choi, *Electrochemistry Communications* 10 (2008) 1688–1690.
- 5.10) Information on <http://www.sony.net/SonyInfo/News/Press/200502/05-006E/>.
- 5.11) G. Ferrara, R. Inguanta, S. Piazza, C. Sunseri, *Electrochemical and Solid-State Letters* 12 (2009) K17–K20.
- 5.12) G. Ferrara, R. Inguanta, S. Piazza, C. Sunseri, *Journal of Nanoscience and Nanotechnology* 10 (2010) 8328–8335.
- 5.13) A.D.W. Todd, R.E. Mar, J.R. Dahn, *Journal of The Electrochemical Society* 153 (2006) A1998–A2005.
- 5.14) E. Gómez, E. Guaus, J. Torrent, X. Alcobé, E. Vallés, *Journal of Applied Electrochemistry* 31 (2001) 349–354.
- 5.15) Z. Du, S. Zhang, T. Jiang, Z. Bai, *Electrochimica Acta* 55 (2010) 3537–3541.

- 5.16) C. Li, W. Wei, S. Fang, H. Wang, Y. Zhang, Y. Gui, R. Chen, *Journal of Power Sources* 195 (2010) 2939–2944.
- 5.17) R. Yang, J. Huang, W. Zhao, W. Lai, X. Zhang, J. Zheng, X. Li, *Journal of Power Sources* 195 (2010) 6811–6816
- 5.18) R Yang, Y. Gu, Y. Li, J. Zheng, X. Li, *Acta Materialia* 58 (2010) 866–874.
- 5.19) J. Li, D.-B. Le, P.P. Ferguson, J.R. Dahn, *Electrochimica Acta* 55 (2010) 2991–2995.
- 5.20) B. Liu, Z.P. Guo, G. Du, Y. Nuli, M.F. Hassan, D. Jia, *Journal of Power Sources* 195 (2010) 5382–5386.
- 5.21) X.-Y. Fan, F.-S. Ke, G.-Z. Wei, L. Huang, S.-G. Sun, *Journal of Solid State Electrochemistry* 13 (2009) 1849–1858.
- 5.22) X.-Y. Fan, F.-S. Ke, G.-Z. Wei, L. Huang, S.-G. Sun, *Journal of Alloys and Compounds* 476 (2009) 70–73.
- 5.23) J. He, H. Zhao, M. Wang, X. Jia, *Materials Science and Engineering B* 171 (2010) 35–39.
- 5.24) L. Bazin, S. Mitra, P.L. Taberna, P. Poizot, M. Gressier, M.J. Menu, A. Barnabé, P. Simon, J.-M. Tarascon, *Journal of Power Sources* 188 (2009) 578–582.

Chapter 6

Battery tests for HEV and EV application

6.1 Lithium-ion batteries for application in HEV

6.1.1 Graphite/EC DMC-LiPF₆/LiFePO₄-C

The battery was composed by LiFePO₄-C cathode, graphite anode and conventional electrolyte. The electrodes were balanced: they had the same storage capacity. The electrode area was 0.6 cm². Given that graphite has an irreversible capacity, in the first cycle, significantly higher than lithium iron phosphate, the single electrodes were pre-cycled vs. lithium for a few cycles in order to achieve a high efficiency (i.e. high charge/discharge reversibility), and then they were assembled in the battery. The separator (Whatman) of every electrode was maintained passing from single-electrode cell to battery to facilitate the preservation of the interface electrode-separator (with electrolyte), particularly important for SEI of graphite; thus, the battery had two separators. This could be relevant because the number and the nature of the electrolyte separators influences the internal resistance of the battery because of the alteration of ions mobility. Electrodes characteristic and battery test conditions are shown in Table 6.1.

Table 6.1. Battery electrodes characteristics and testing conditions.

Electrode	Material	Active material	Binder (Teflon)	Conductive carbon	Composite	Battery tests	Currents	Electrolyte	T
		mg	mg	mg	mg		mA		°C
Anode	Graphite	2.60 (88%)	0.21 (7%)	0.15 (5%)	2.96	SCT 1C;	0.73;	EC DMC	30
Cathode	LiFePO ₄ -C	6.54 (74.6%)	0.44 (5%)	1.80 (20.4%)	8.78	HPPC 5C,10C	3.54, 7.09	LiPF ₆	

The FreedomCAR tests of the lithium-ion battery we assembled with LiFePO₄-C cathode and graphite anode were performed by setting the V_{\max} at 4.0 V and the V_{\min} at 2.2 V; the low-current HPPC test was carried out at the protocol discharge rate of 5C and the high-current's at 10C. All the specific parameters evaluated by these tests refer to a total battery mass (w_{battery}) which is twice the total composite mass of the two electrodes. The 1C discharges used for SCT and HPPC tests were effective, i.e. the battery was discharged in one hour (as suggested in the FreedomCAR manual), and 5C and 10C rates used in the pulses of HPPC test were multiple of this 1C. Figure 6.1 shows, according to SCT test, the plots of the battery discharge voltage and of the specific cumulative energy removed during discharge (E_{DOD}) vs. DOD (Deep Of Discharge) at 1 C-rate and 30°C. Figure 6.2a displays the voltage profile of the battery (solid line) and of each electrode vs. Li reference electrode (dashed and dotted lines) along the sequence of the low-current HPPC test at different DOD from 10% to 90%, separated by 10% DOD. The plots also display the profiles during the full battery charge (1C galvanostatic/1 h potentiostatic) and the equilibration time (1 h OCV rest) before the beginning of the test. They further display the repetition of the 10% DOD discharge at 1 C-rate followed by 1 h OCV rest and the HPPC test at each DOD. These HPPC tests include pulse discharge at 5.81 mA cm⁻² (for 0.6 cm² electrode area, $i_{\text{disc}} = 3.54$ mA) for 10 s, 40 s rest to relax to OCV, and regenerative pulse for 10 s at 2.60 mA. Figure 6.2b shows the magnification of the HPPC voltage profile at 10% DOD, as an example, to mark the values V_0 and V_2 , which are the battery potentials just before the discharge and regenerative pulses, respectively, and the values V_1 and V_3 , which are the potentials at the end of these pulses. These potential values were used to calculate at different DOD along the FreedomCAR protocol the 10 s discharge and regenerative pulse resistance, R_{disc} and R_{reg} , respectively, as in Eqs. (1) and (2):

$$R_{\text{disc}} = \frac{(V_0 - V_1)}{i_{\text{disc}}} \quad (1)$$

$$R_{\text{reg}} = \frac{(V_3 - V_2)}{i_{\text{reg}}} \quad (2)$$

The specific discharge (P_{dis}) and regenerative (P_{reg}) pulse power capability at each DOD were then evaluated, as in Eqs. (3) and (4):

$$P_{disc} = \frac{V_{min}(OCV_{disc} - V_{min})}{(R_{disc} w_{battery})} \quad (3)$$

$$P_{reg} = \frac{V_{max}(V_{max} - OCV_{reg})}{(R_{reg} w_{battery})} \quad (4)$$

where OCV_{disc} is the measured open circuit voltage at the end of each HPPC rest-period and OCV_{regen} the interpolated value through the measured data. Similarly, Figure 6.3 displays the voltage profiles along the sequence of the high-current (10C) HPPC test from 10% DOD to 70%, with discharge pulse current of 7.09 mA and regenerative of 5.31 mA. Figure 6.4 shows the resistance values, R_{disc} and R_{reg} , vs. DOD and Figure 6.5 the corresponding pulse power capability values, P_{disc} and P_{reg} , calculated from low-current HPPC test up to 90% DOD and high-current up to 70%. Figure 6.5 also displays the minimum pulse power goal stated by DOE FreedomCAR for power-assist HEV (dashed line) and shows that all the pulse power data go beyond this goal, the only exception being the discharge pulse power at 90% DOD of the low-current HPPC test. We took the lowest power capability plots vs. DOD, i.e. the P_{disc} plots from low- and high-current HPPC tests, and combined each with the plot of cumulative energy (E_{DOD}) vs. DOD from the SCT test to evaluate the available energy vs. pulse power capability of the battery. The results are shown in Figure 6.6, a non-conventional Ragone plot which also reports the DOE goal for power-assist full HEV, and indicate that the graphite/LiFePO₄-C battery surpasses this goal.

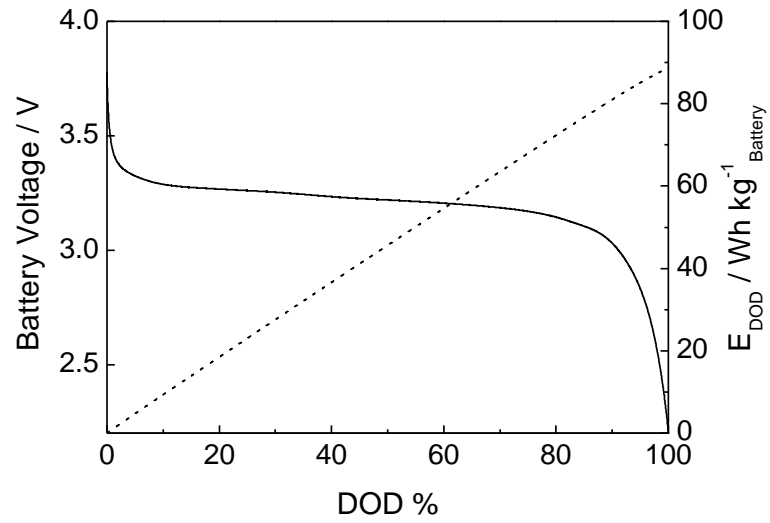


Figure 6.1. Static capacity test (SCT) at 1 C-rate and 30°C on the graphite/LiFePO₄-C battery. Dashed line is the relationship between cumulative energy and DOD.

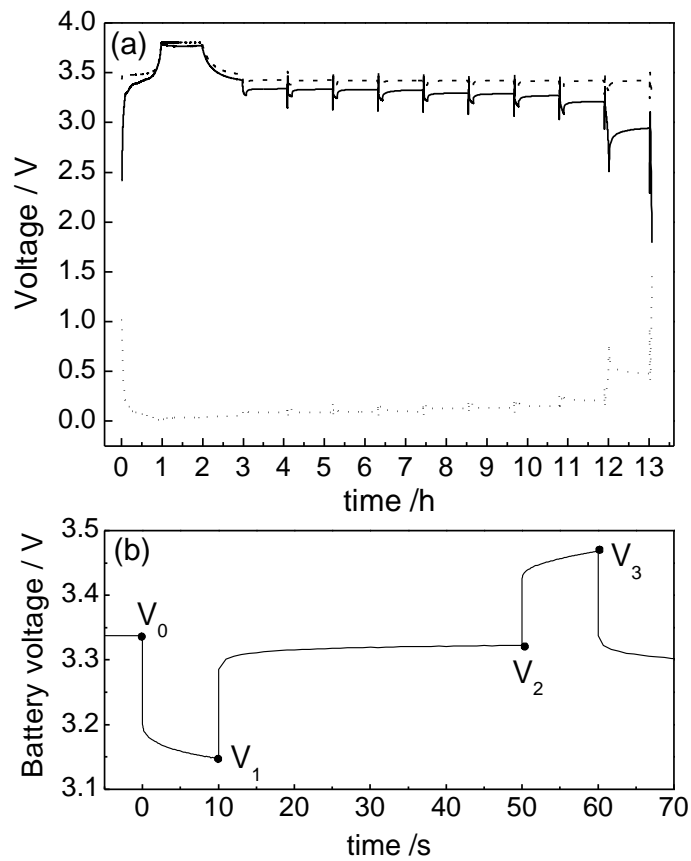


Figure 6.2. (a) Voltage profiles of the low-current HPPC performed on the graphite/LiFePO₄-C battery. (—) Battery voltage, (---) cathode and (···) anode voltages; (b) magnification of one voltage impulse of the battery.

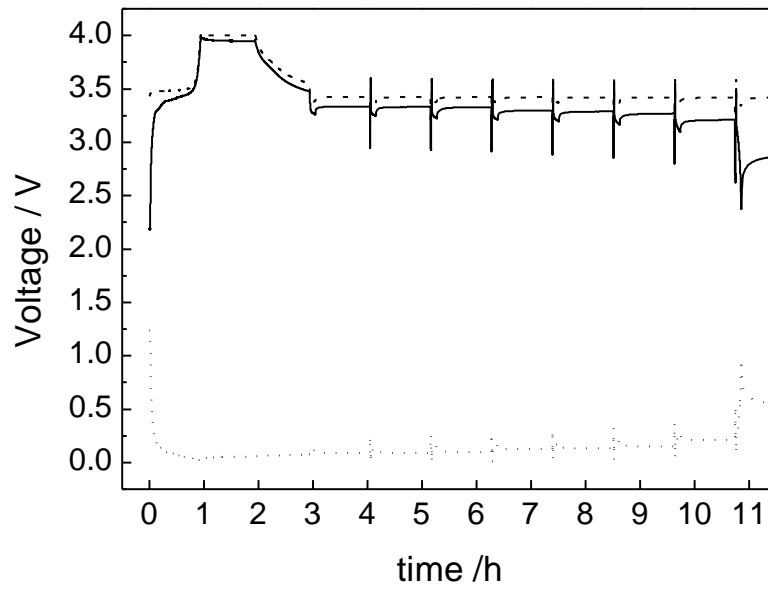


Figure 6.3. Voltage profile of the high-current HPPC performed on the graphite/ $\text{LiFePO}_4\text{-C}$ battery. (—) Battery voltage, (---) cathode and (···) anode voltages.

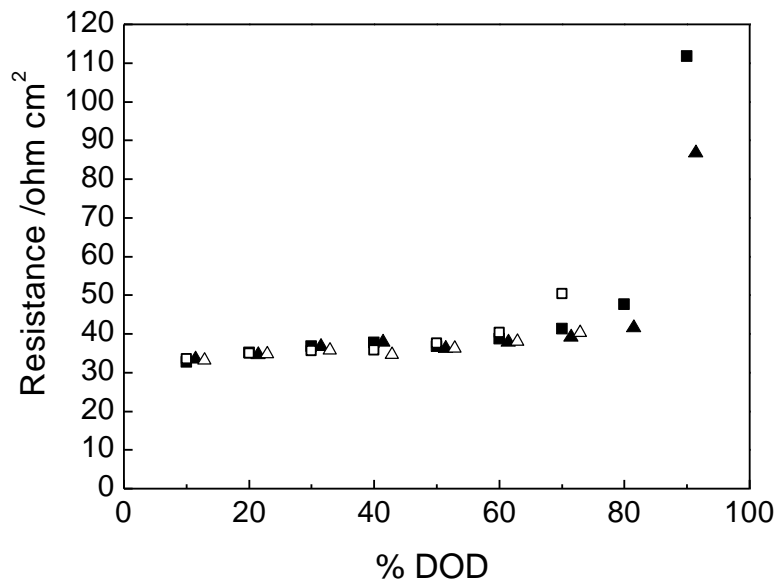


Figure 6.4. Pulse resistances vs. %DOD: (\blacksquare) and (\blacktriangle) are R_{dis} and R_{regen} calculated from the low-current HPPC test; (\square) and (\triangle) are R_{dis} and R_{regen} calculated from the high-current one.

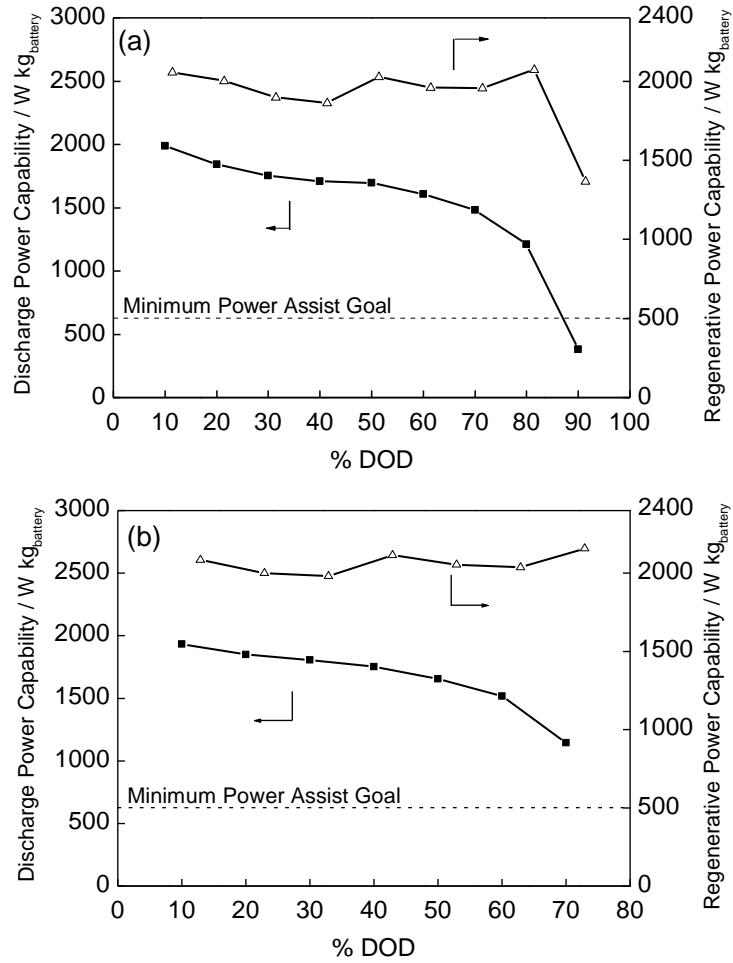


Figure 6.5 Discharge and regenerative pulse-power capability at low (a) and high (b) current HPPC test of graphite/LiFePO₄-C battery.

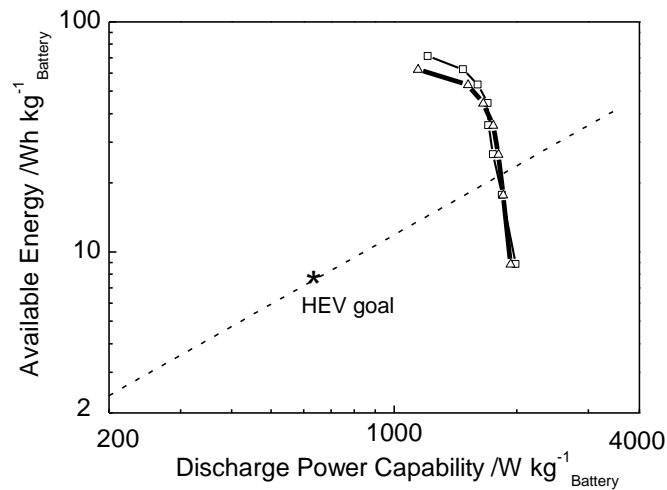


Figure 6.6. Available specific energy vs. specific power capability of battery from HPPC tests: (□) low-current, (Δ) high-current. The diagonal dashed line indicates the optimal P/E ratio for power-assist in HEV. The marker refers to the DOE goal.

6.1.2 Graphite/PYR₁₄TFSI 0.4m LiTFSI with 10% VC/LiFePO₄-C

The battery was composed by LiFePO₄-C cathode, graphite anode and PYR₁₄TFSI 0.4m LiTFSI with 10% VC electrolyte. The electrodes were balanced. The electrode area was 0.61 cm². As in the previous case, the single electrodes were pre-cycled vs. lithium in the same electrolyte at 60°C for a few cycles before the assembly in the battery maintaining the separators (Durieux), thus, the battery had two separators. Electrodes characteristics and testing conditions are reported in Table 6.2.

Table 6.2. Battery electrodes characteristics and testing conditions.

Electrode	Material	Active material	Binder	Conductive carbon	Composite	Battery test	Currents	Electrolyte	T
		mg	mg	mg	mg		mA		°C
Anode	Graphite	2.12 (70%)	0.60** (20%)	0.30 (10%)	3.02	SCT 1C; HPPC 5C	0.236 2.11	90% PYR ₁₄ TFSI 0.4m LiTFSI + 10% VC	60
Cathode	LiFePO ₄ -C	2.48 (74.6%)	0.16* (5%)	0.68 (20.4%)	3.32				

*Teflon; **PVDF.

First, the battery was cycled by deep galvanostatic charge/discharge cycles at 1C for 12 cycles at 60°C (Figure 6.7) before SCT and HPPC test.

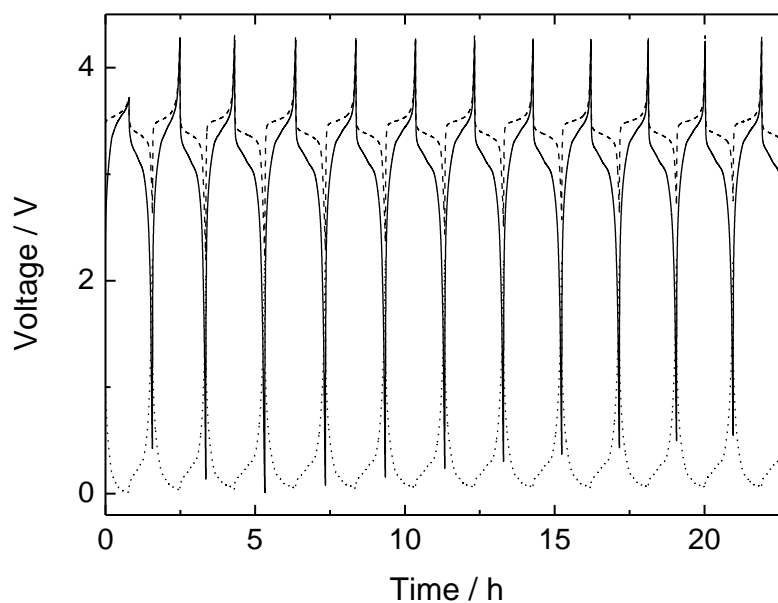


Figure 6.7. Voltage profile of the first galvanostatic cycles performed on the battery. (—) Battery voltage, (---) cathode and (···) anode voltages.

The FreedomCAR HPPC tests of the lithium-ion battery we assembled were performed by setting battery V_{\max} at 3.6 V and V_{\min} at 2.0 V. The 1C discharges used for SCT and HPPC tests were effective, i.e. the battery was discharged in one hour (as suggested in the FreedomCAR manual), while 5C rate used in the pulses of HPPC test referred to theoretic capacity of the cathode. All the tests were performed on the battery at 60°C. Figure 6.8 shows, according to SCT test, the plots of the battery discharge voltage and of the specific cumulative energy removed during discharge (E_{DOD}) vs. DOD at 1 C-rate and 60°C. The battery voltage profile during the HPPC test is shown in figure 6.9 and the calculated pulses resistance and power are reported in Table 6.3. The discharge power capability vs. energy plot, compared with the HEV pulse power target (625 W kg⁻¹ for discharge and 500 W kg⁻¹ for charge), is shown in Figure 6.10, and indicates that the graphite/PYR₁₄TFSI 0.4m LiTFSI with 10% VC/LiFePO₄-C lithium-ion battery surpasses the pulse power goal, in particular in the range 10% - 55% DOD: this is the state of charge in which has to be maintained the battery during the utilization in power-assist mode in HEV. Furthermore, in Figure 6.10 is shown the corresponding available energy calculated at such DOD (as stated in the DOE protocol) that is 25 Wh kg⁻¹_{battery}, well above the DOE target (7.5 Wh kg⁻¹_{battery}). In conclusion, this battery surpasses the DOE goal for power-assist HEV application.

A further representation of the energy and power behavior is represented by the plot Usable Energy vs. Power curve illustrated in Figure 6.11. The usable energy is defined as the amount of energy available between the discharge and charge pulse-power curves for a given pulse-power^{6.1}. It represents the energy (or power) available over the operating region where a specified power (or energy) demand can be met. The resulting available energy at goal power was 25 Wh kg⁻¹_{battery} and the resulting available power at goal energy was 726 W kg⁻¹_{battery}.

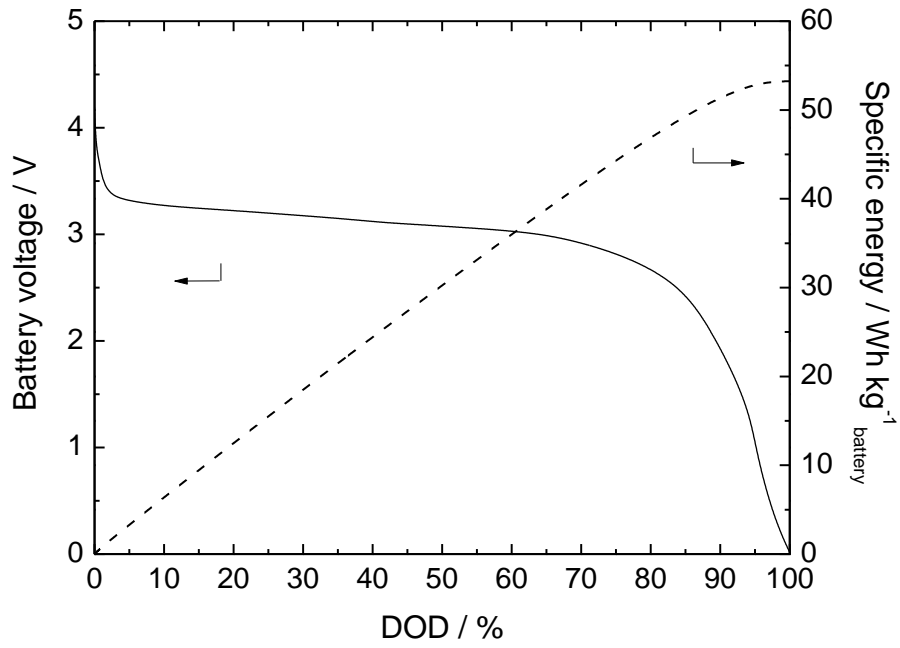


Figure 6.8. Static capacity test (SCT) at 1 C-rate and 60°C on the battery. Dashed line is the relationship between cumulative energy and DOD.

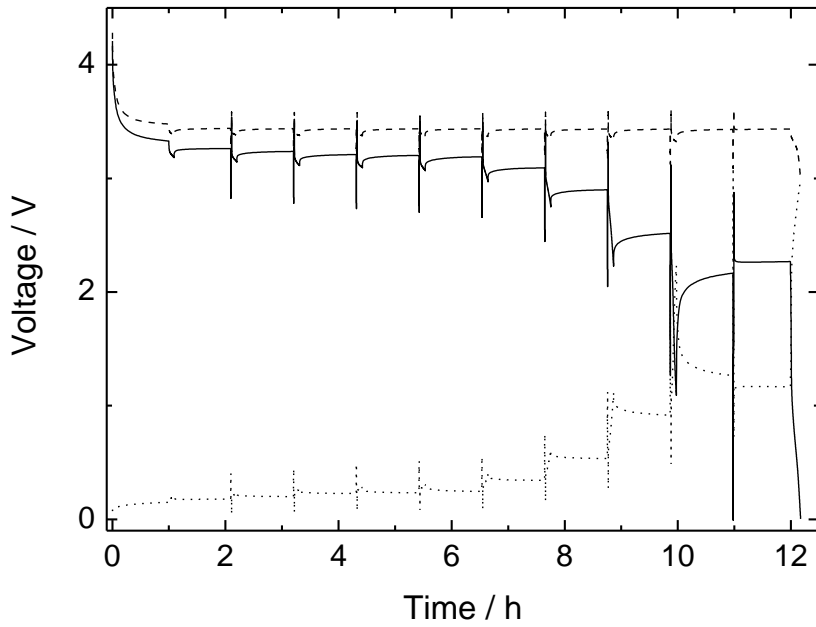


Figure 6.9. Voltage profile of the HPPC at 5C performed on the battery. (—) Battery voltage, (---) cathode and (···) anode voltages.

Table 6.3. Results of HPPC test.

DOD	V ₀	V ₁	V ₂	V ₃	R _{disc}	R _{regen}	R _{disc}	R _{regen}	P _{disc}	P _{regen}
%	V	V	V	V	ohm	ohm	ohm cm ²	ohm cm ²	W kg ⁻¹ battery	W kg ⁻¹ battery
10	3.261	2.824	3.234	3.537	207	192	124	115	960	542
20	3.236	2.78	3.206	3.519	216	198	130	119	902	565
30	3.209	2.735	3.18	3.502	225	204	135	122	849	585
40	3.201	2.701	3.171	3.5	237	208	142	125	799	585
50	3.189	2.658	3.147	3.492	252	218	151	131	745	589
60	3.091	2.445	3.025	3.426	306	254	184	152	562	643
70	2.898	2.048	2.789	3.317	403	334	242	201	352	689
80	2.515	1.274	2.293	3.117	588	522	353	313	138	712
90	2.165	0	1.535	2.875	1026	848	616	509	25	691

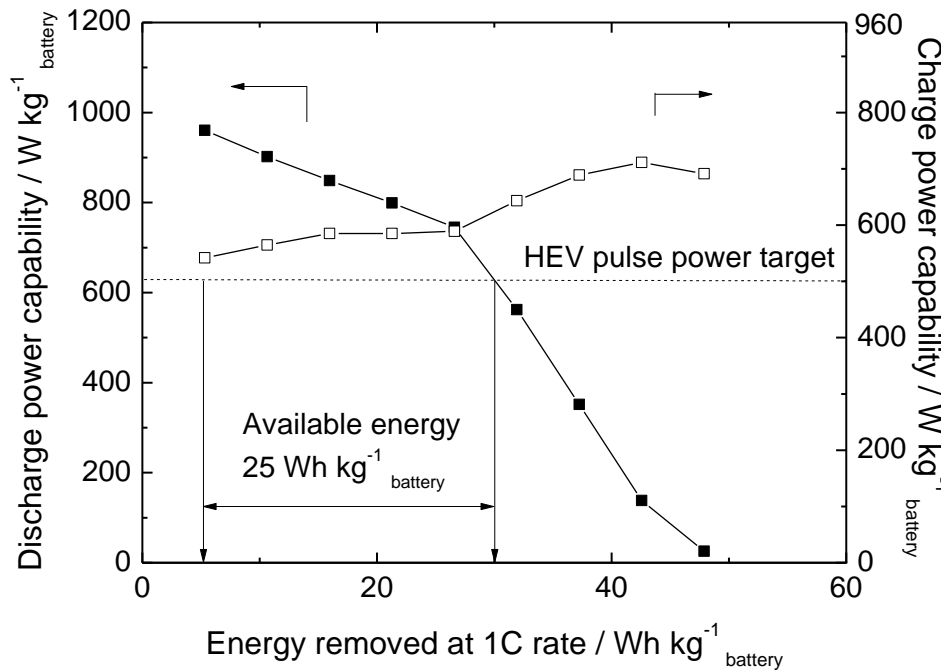


Figure 6.10 Discharge power capability vs. energy removed at 1C rate of battery from HPPC 5C test. The dashed line refers to HEV pulse power target.

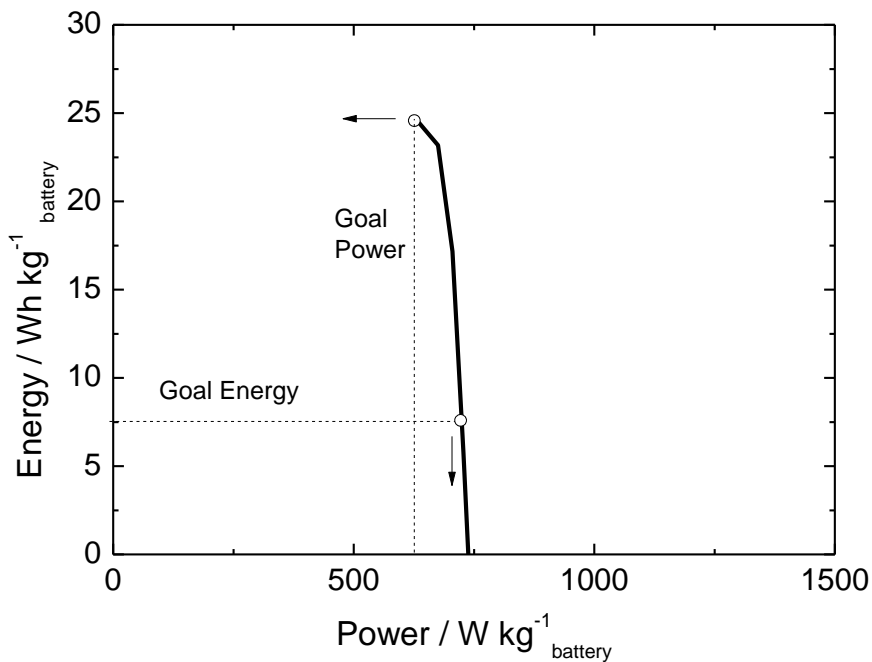


Figure 6.11 Usable energy as a function of discharge pulse-power for the battery. The arrows indicates the resulting available energy/power at goal power/energy.

After the SCT and HPPC tests the battery was cycled again by deep galvanostatic cycles at 1C to evaluate its cycling stability. In figure 6.12 is shown the capacity of the battery over all cycles (even the cycles before SCT and HPPC test are shown) referred to the discharge capacity of the first cycle. Even if there was a capacity fade (50% after 275 cycles) the capacity seems to stabilize in the end. The efficiency values were high.

Then SCT and HPPC tests were performed again on the battery in order to evaluate energy and power fade over cycling. The results are shown in Table 6.4, Figures 6.13 (Discharge power capability vs. energy removed at 1C rate) and 6.14 (Usable energy vs. pulse-power). In particular, the Figure 6.13 demonstrates that the battery still satisfied the DOE energy and power targets for application on HEV. It worth noting that the battery cycling decreases more the available energy than the available power of the battery.

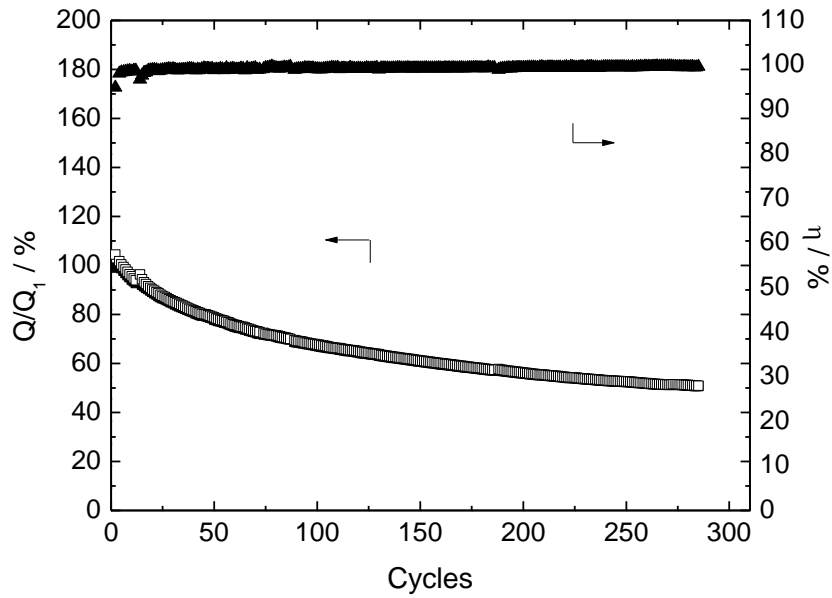


Figure 6.12. Battery capacity (normalized to capacity of the first cycle) vs. cycle number of the battery cycled at 1C and 60°C. (\square) charge and (\blacksquare) discharge.

Table 6.4. Results of HPPC test on cycled cell.

DOD	V₀	V₁	V₂	V₃	R_{disc}	R_{regen}	R_{disc}	R_{regen}	P_{disc}	P_{regen}
%	V	V	V	V	ohm	ohm	ohm cm²	ohm cm²	W kg⁻¹	W kg⁻¹
									battery	battery
10	3.208	2.742	3.18	3.518	221	214	135	130	863	557
20	3.202	2.726	3.172	3.51	226	214	138	130	840	568
30	3.189	2.683	3.142	3.497	240	225	146	137	782	579
40	3.134	2.574	3.075	3.457	265	242	162	147	674	617
50	3.057	2.425	2.983	3.407	300	268	183	164	557	653
60	2.951	2.21	2.854	3.342	351	309	214	188	427	686

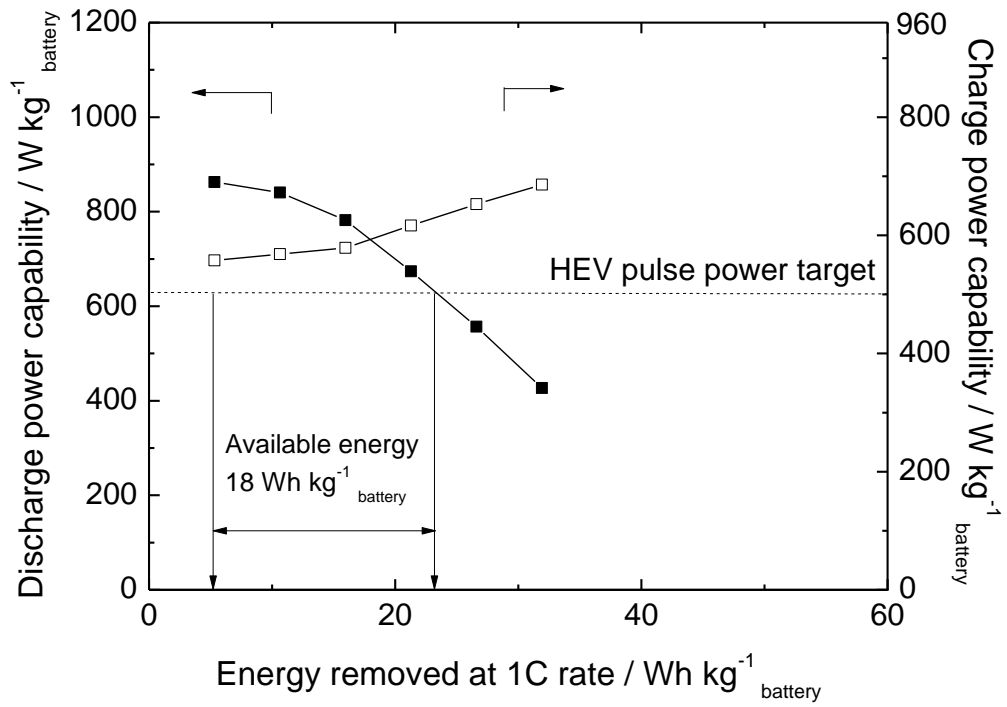


Figure 6.13 Discharge power capability vs. energy removed at 1C rate of cycled battery from HPPC 5C test.
The dashed line refers to HEV pulse power target.

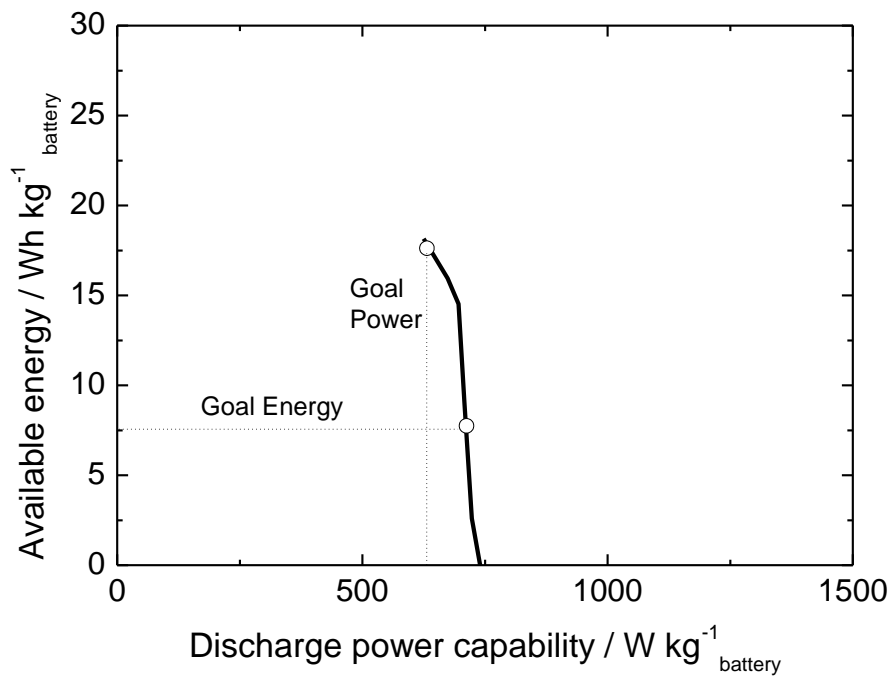


Figure 6.14 Usable energy as a function of discharge pulse-power for the cycled battery.

6.1.3 TiO₂/PYR₁₄TFSI 0.4m LiTFSI/LiFePO₄-C

The battery was composed by LiFePO₄-C cathode, TiO₂ anode and PYR₁₄TFSI 0.4m LiTFSI electrolyte. The electrodes were balanced. The electrodes area was 0.6 cm². As in the previous case, the single electrodes were pre-cycled *vs.* lithium in the same electrolyte at 60°C for a few cycles before the assembly in the battery maintaining the separators (Durieux), thus, the battery had two separators. . Electrodes characteristics and testing conditions are reported in Table 6.5.

Table 6.5. Battery electrodes characteristics and testing conditions.

Electrode	Material	Active material	Binder	Conductive carbon	Composite	Battery test	Currents	Electrolyte	T
		mg	mg	mg	mg		mA		°C
Anode	TiO ₂	1.76 (70%)	0.50** (20%)	0.25 (10%)	2.51	SCT 1C; HPPC 2C	0.16 0.80	PYR ₁₄ TFSI 0.4m LiTFSI	60
Cathode	LiFePO ₄ -C	2.15 (74.6%)	0.15* (5%)	0.59 (20.4%)	2.89				

*Teflon; **PVDF.

First, the battery was cycled by deep galvanostatic charge/discharge cycles at C/10 for 3 cycles at 60°C (Figure 6.15) before SCT and HPPC test.

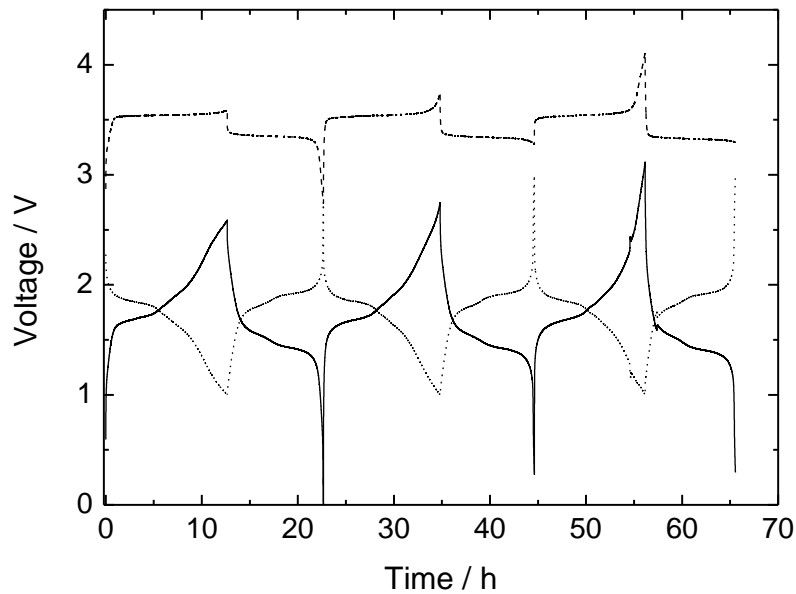


Figure 6.15. Voltage profile of the first galvanostatic cycles at C/10 performed on the battery. (—) Battery voltage, (---) cathode and (···) anode voltages.

The FreedomCAR HPPC test of the lithium-ion battery we assembled were performed by setting battery V_{\max} at 2.5 V and V_{\min} at 1.0 V. The 1C discharges used for SCT and HPPC tests were effective, i.e. the battery was discharged in one hour, while 2C rate used in the pulses of HPPC test referred to theoretic capacity of the cathode. All the tests were performed at 60°C. Figure 6.16 shows, according to SCT test, the plots of the battery discharge voltage and of the specific cumulative energy removed during discharge (E_{DOD}) vs. DOD at 1 C-rate and 60°C. The battery voltage profile during the HPPC test is shown in figure 6.17; the resistance and power results are shown in Table 6.6, in which we can see that the $\text{TiO}_2/\text{PYR}_{14}\text{TFSI}$ 0.4m $\text{LiTFSI}/\text{LiFePO}_4\text{-C}$ lithium-ion battery does not surpass the discharge pulse power goal, because of the high resistances during pulses. This was probably due to non-optimal TiO_2 anode, not pressed and with a high percentage of non-conductive binder. However, it worth noting that this battery showed very high stability (no capacity fade) over cycling, as demonstrated by deep galvanostatic charge/discharge cycles at C/3 performed after the FreedomCAR tests (Figure 6.18).

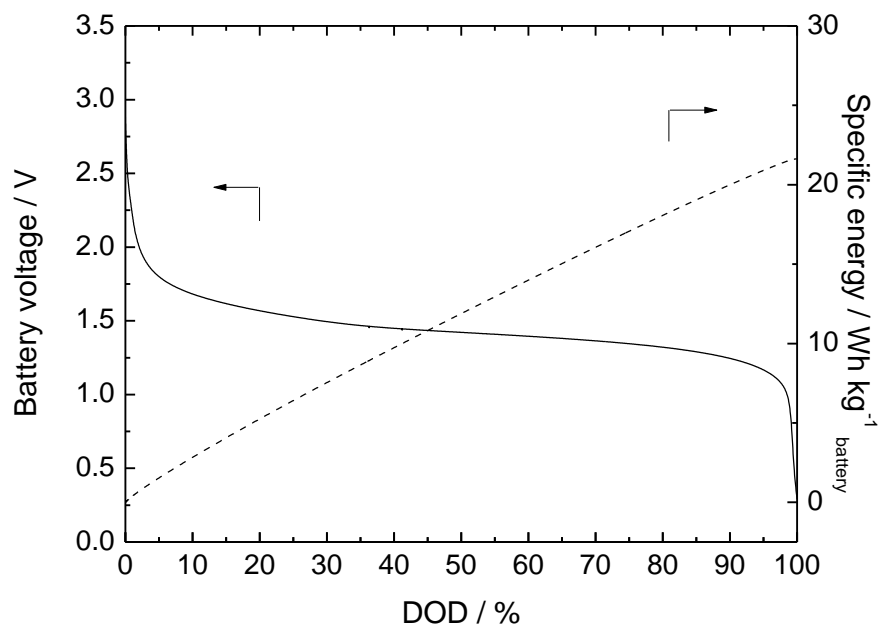


Figure 6.16. Static capacity test (SCT) at 1 C-rate and 60°C on the battery. Dashed line is the relationship between cumulative energy and DOD.

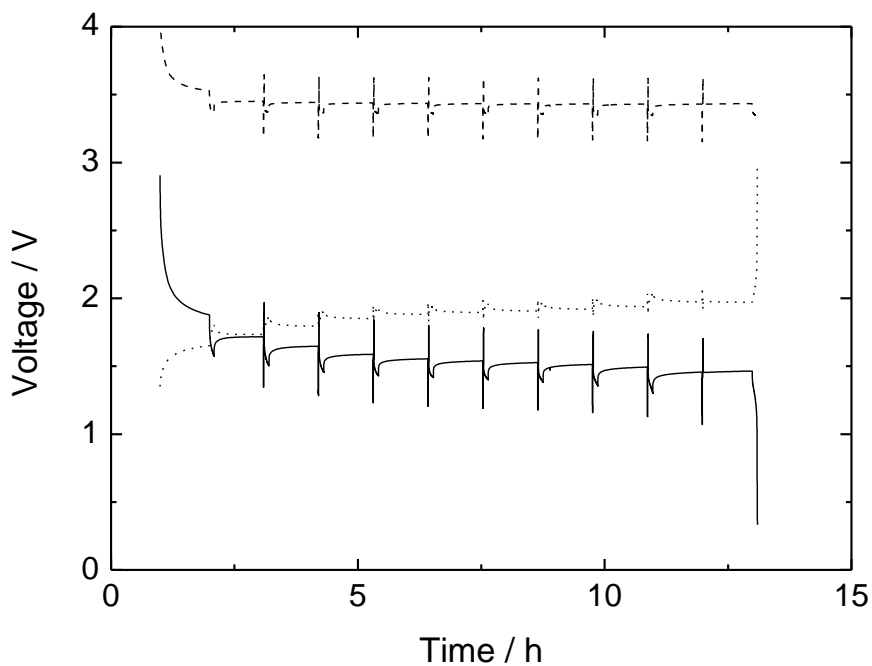


Figure 6.17. Voltage profile of the HPPC at 5C performed on the battery. (—) Battery voltage, (---) cathode and (···) anode voltages.

Table 6.6. Results of HPPC test.

DOD	V ₀	V ₁	V ₂	V ₃	R _{disc}	R _{regen}	R _{disc}	R _{regen}	P _{disc}	P _{regen}
%	V	V	V	V	ohm	ohm	ohm cm ²	ohm cm ²	W kg ⁻¹ battery	W kg ⁻¹ battery
10	1,715	1,346	1,674	1,968	460	489	281	298	144	391
20	1,646	1,284	1,612	1,895	451	471	275	287	133	437
30	1,586	1,23	1,56	1,835	444	458	271	279	122	476
40	1,553	1,204	1,533	1,799	435	443	265	270	118	506
50	1,538	1,191	1,519	1,781	433	436	264	266	115	521
60	1,526	1,178	1,507	1,768	434	434	265	265	112	529
70	1,512	1,159	1,493	1,754	440	434	268	265	108	537
80	1,493	1,129	1,47	1,736	454	443	277	270	101	539
90	1,456	1,07	1,426	1,702	481	459	293	280	88	541

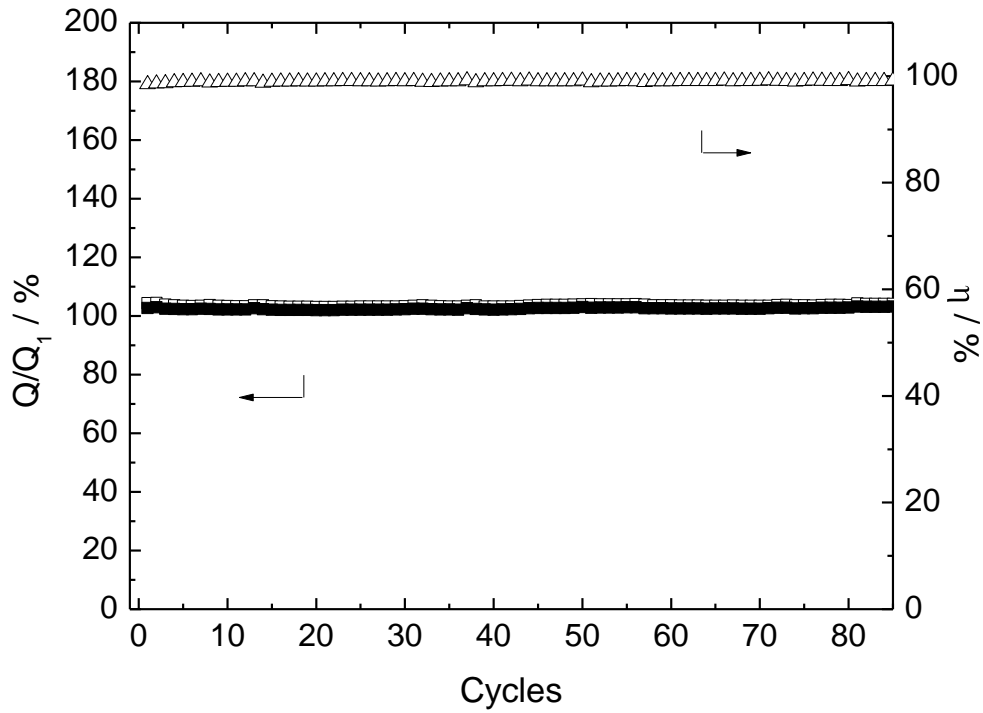


Figure 6.18. Battery capacity (normalized to capacity of 80 mAh g⁻¹ LiFePO₄ of the first cycle) vs. cycle number of the battery cycled at C/3 and 60°C. (□) charge and (■) discharge.

6.1.4 Li₄Ti₅O₁₂/ PYR₁₄TFSI 0.4m LiTFSI/LiFePO₄-C

The battery was composed by LiFePO₄-C cathode, Li₄Ti₅O₁₂ anode and PYR₁₄TFSI 0.4m LiTFSI electrolyte. The electrodes were balanced. The electrodes area was 0.4 cm². The single electrodes were pre-cycled vs. lithium in the same electrolyte at 60°C for a few cycles before the assembly in the battery maintaining the separators (Durieux), thus, the battery had two separators. Electrodes characteristics and testing conditions are reported in Table 6.7.

Table 6.7. Battery electrodes characteristics and testing conditions.

Electrode	Material	Active material	Binder	Conductive carbon	Composite	Battery tests	Currents	Electrolyte	T
		mg	mg	mg	mg		mA		°C
Anode ⁺	Li ₄ Ti ₅ O ₁₂	1.52 (80%)	0.19** (10%)	0.19 (10%)	1.90	SCT 1C; HPPC 5C	0.12 1.09	PYR ₁₄ TFSI 0.4m LiTFSI	60
Cathode	LiFePO ₄ -C	1.28 (74.6%)	0.09* (5%)	0.35 (20.4%)	1.72				

⁺Pressed, *Teflon; **PVDF.

First, the battery was cycled by deep galvanostatic charge/discharge cycles at C/10 for 3 cycles at 60°C (Figure 6.19) before SCT and HPPC test.

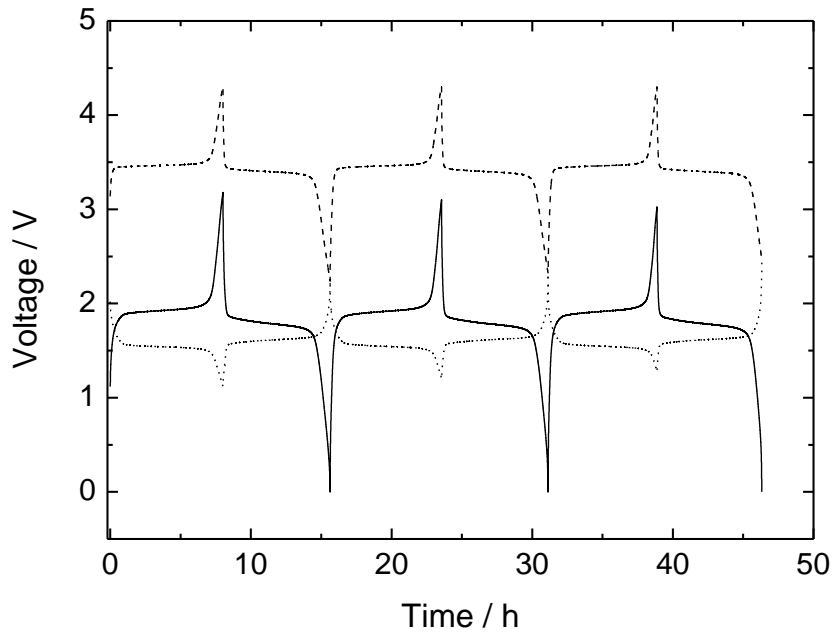


Figure 6.19. Voltage profile of the first galvanostatic cycles at C/10 performed on the battery. (—) Battery voltage, (---) cathode and (...) anode voltages.

The FreedomCAR HPPC test of the lithium-ion battery we assembled were performed by setting battery V_{\max} at 2.5 V and V_{\min} at 1.0 V. The 1C discharges used for SCT and HPPC tests were effective, i.e. the battery was discharged in one hour, while 5C rate used in the pulses of HPPC test referred to theoretic capacity of the cathode. All the test were performed at 60°C. Figure 6.20 shows, according to SCT test, the plots of the battery discharge voltage and of the specific cumulative energy removed during discharge (E_{DOD}) vs. DOD at 1 C-rate and 60°C. The battery voltage profile during the HPPC test at 5C is shown in Figure 6.21; the resistance and power results are shown in Table 6.8, where we can see that the $\text{Li}_4\text{Ti}_5\text{O}_{12}/\text{PYR}_{14}\text{TFSI}$ 0.4m $\text{LiTFSI}/\text{LiFePO}_4\text{-C}$ lithium-ion battery does not surpass the discharge pulse power goal, even if the values of resistances are lower and pulses power are higher than previous battery. This $\text{Li}_4\text{Ti}_5\text{O}_{12}/\text{LiFePO}_4$ battery has some main advantages in respect to $\text{TiO}_2/\text{LiFePO}_4$ battery: an higher OCV voltage (i.e., higher energy) and lower resistances, thanks to the $\text{Li}_4\text{Ti}_5\text{O}_{12}$ anode that was pressed and with a low amount of non-conductive binder. Furthermore, the battery was galvanostatically cycled at C/3 after FreedomCAR tests demonstrating good stability for 12 cycles.

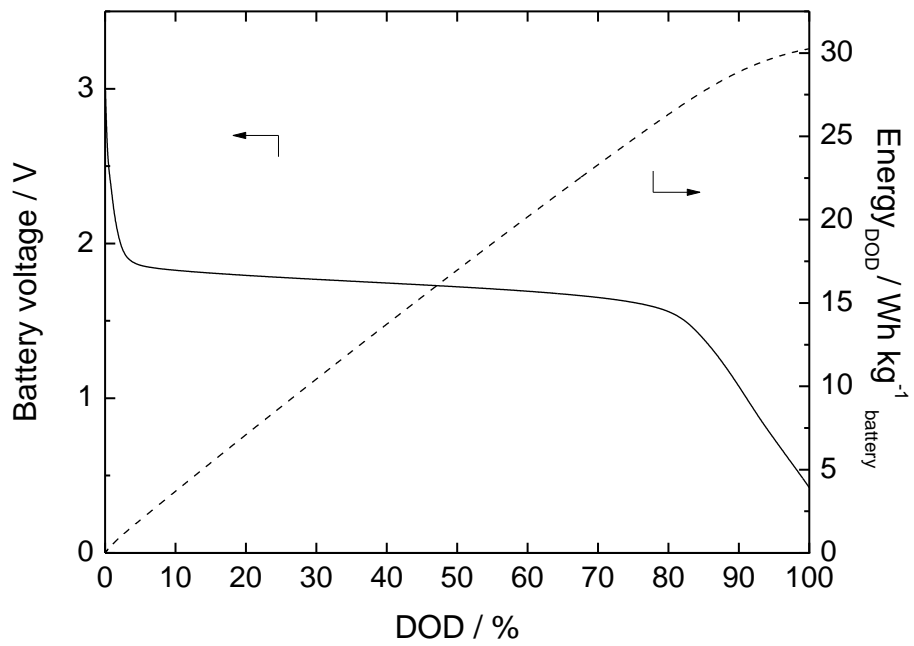


Figure 6.20. Static capacity test (SCT) at 1 C-rate and 60°C on the battery. Dashed line is the relationship between cumulative energy and DOD.

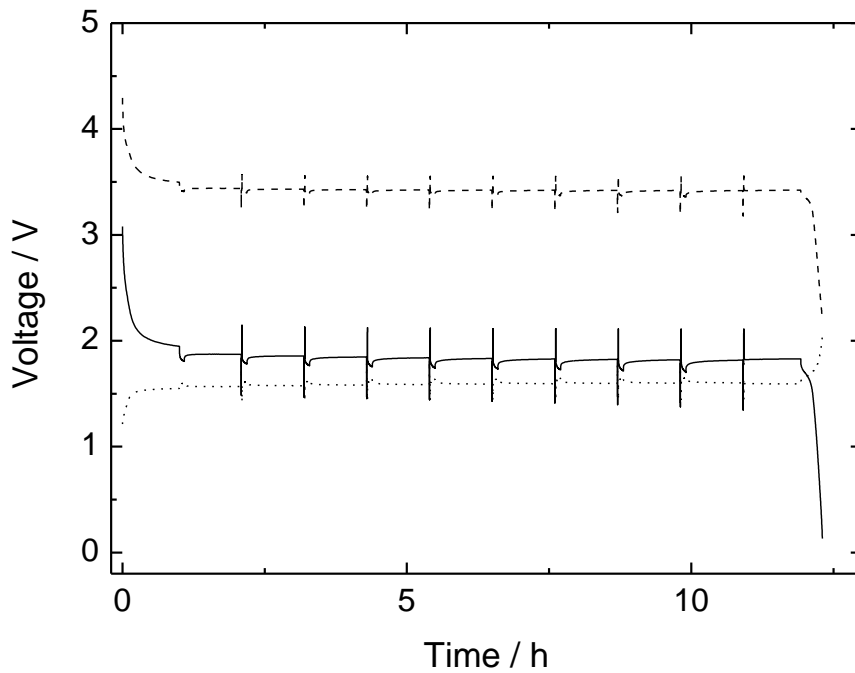


Figure 6.21. Voltage profile of the HPPC at 5C performed on the battery. (—) Battery voltage, (---) cathode and (···) anode voltages.

Table 6.8. Results of HPPC test.

DOD	V₀	V₁	V₂	V₃	R_{disc}	R_{regen}	R_{disc}	R_{regen}	P_{disc}	P_{regen}
%	V	V	V	V	ohm	ohm	ohm cm²	ohm cm²	W kg⁻¹ battery	W kg⁻¹ battery
10	1.870	1.487	1.848	2.146	352	365	141	146	342	797
20	1.855	1.467	1.834	2.131	356	364	142	146	332	817
30	1.846	1.453	1.825	2.122	361	364	144	146	324	828
40	1.838	1.441	1.818	2.118	364	368	146	147	318	828
50	1.833	1.427	1.811	2.115	373	373	149	149	309	826
60	1.827	1.413	1.804	2.113	380	379	152	151	301	821
70	1.823	1.395	1.797	2.112	393	386	157	154	289	813
80	1.82	1.375	1.789	2.11	408	393	163	157	277	807
90	1.816	1.347	1.781	2.11	430	403	172	161	262	796

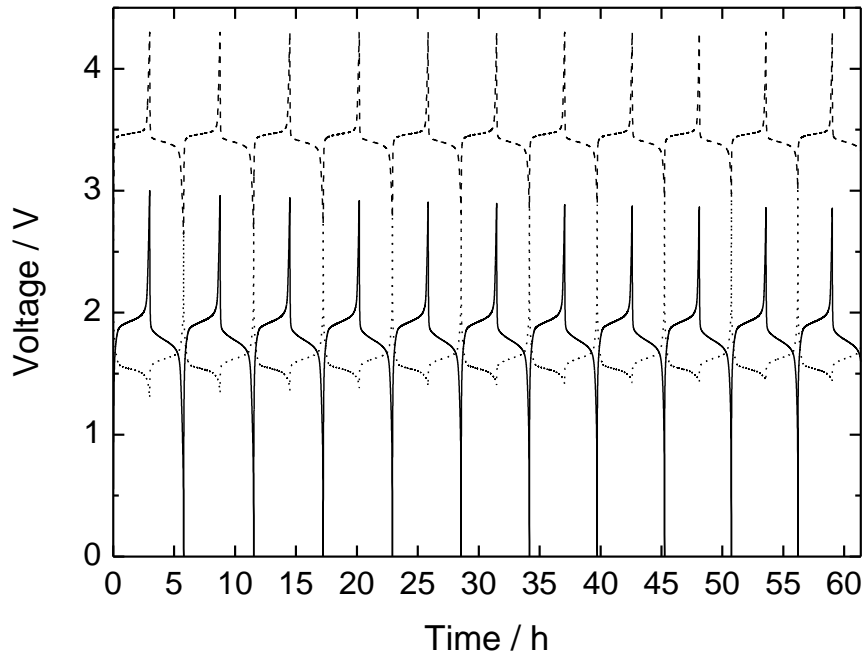


Figure 6.22. Voltage profile of the galvanostatic cycles at C/3 performed on the battery after FreedomCAR tests. (—) Battery voltage, (---) cathode and (···) anode voltages.

6.1.5 TiO₂ / PYR₁₄TFSI-EC DMC LiPF₆ 50:50/ LiFePO₄-C

The battery was composed by LiFePO₄-C cathode, TiO₂ anode and PYR₁₄TFSI-EC DMC LiPF₆ 50:50 mixture electrolyte. The electrodes were balanced. The electrodes area was 0.6 cm². The single electrodes were pre-cycled vs. lithium in the same electrolyte at 30°C for a few cycles before the assembly in the battery maintaining the separators (Whatman), thus, the battery had two separators. Electrodes characteristics and testing conditions are reported in Table 6.9.

Table 6.9. Battery electrodes characteristics and testing conditions.

Electrode	Material	Active material	Binder	Conductive carbon	Composite	Battery tests	Currents	Electrolyte	T
		mg	mg	mg	mg		mA		°C
Anode	TiO ₂	1.28 (70%)	0.36** (20%)	0.18 (10%)	1.82	SCT 1C; HPPC	0.15; 1.55	PYR ₁₄ TFSI- EC DMC LiPF ₆ 50:50	30
Cathode	LiFePO ₄ -C	1.82 (74.6%)	0.12* (5%)	0.50 (20.4%)	2.44	5C			

*Teflon; **PVDF.

First, the battery was cycled by deep galvanostatic charge/discharge cycles at C/3 for one cycle at 30°C (Figure 6.22).

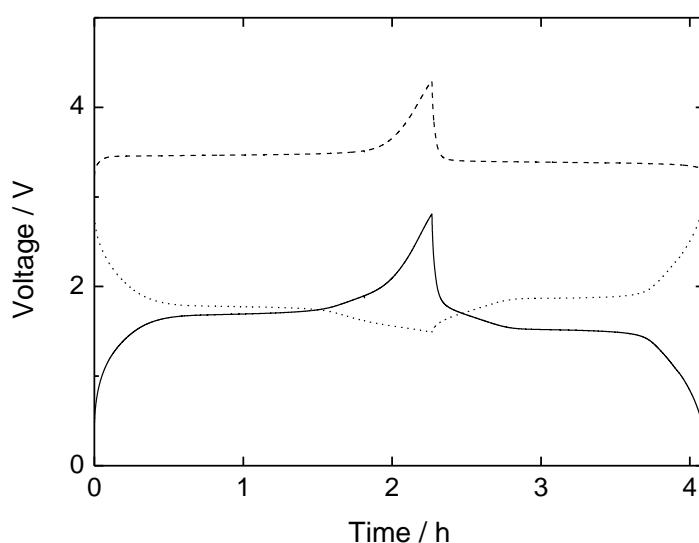


Figure 6.22. Voltage profile of the first galvanostatic cycle at C/3 performed on the battery. (—) Battery voltage, (---) cathode and (···) anode voltages.

The FreedomCAR HPPC test of the lithium-ion battery we assembled were performed by setting battery V_{\max} at 2.0 V and V_{\min} at 1.0 V. The 1C discharges used for SCT and HPPC tests were effective, i.e. the battery was discharged in one hour, while 5C rate used in the pulses of HPPC test referred to theoretic capacity of the cathode. All the tests were performed at 30°C. Figure 6.23 shows, according to SCT test, the plots of the battery discharge voltage and of the specific cumulative energy removed during discharge (E_{DOD}) vs. DOD at 1 C-rate and 60°C. The battery voltage profile during the HPPC test is shown in figure 6.24; the resistance and power results are shown in Table 6.10, where we can see that the $\text{TiO}_2/\text{PYR}_{14}\text{TFSI-EC DMC LiPF}_6$ 50:50/ $\text{LiFePO}_4\text{-C}$ lithium-ion battery do not surpasses the discharge pulse power goal, even if the resistances values during pulses were lower than pure-ionic liquid battery, thanks to the higher conductivity of the electrolyte. Furthermore, in the last part of HPPC test the anode appeared no more balanced with the cathode.

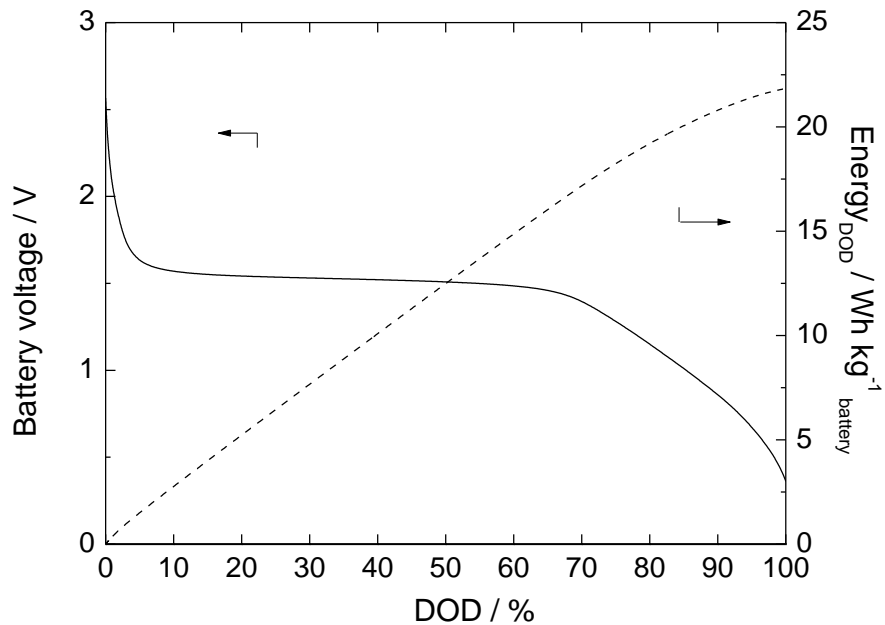


Figure 6.23. Static capacity test (SCT) performed at 1 C-rate and 30°C on the battery. Dashed line is the relationship between cumulative energy and DOD.

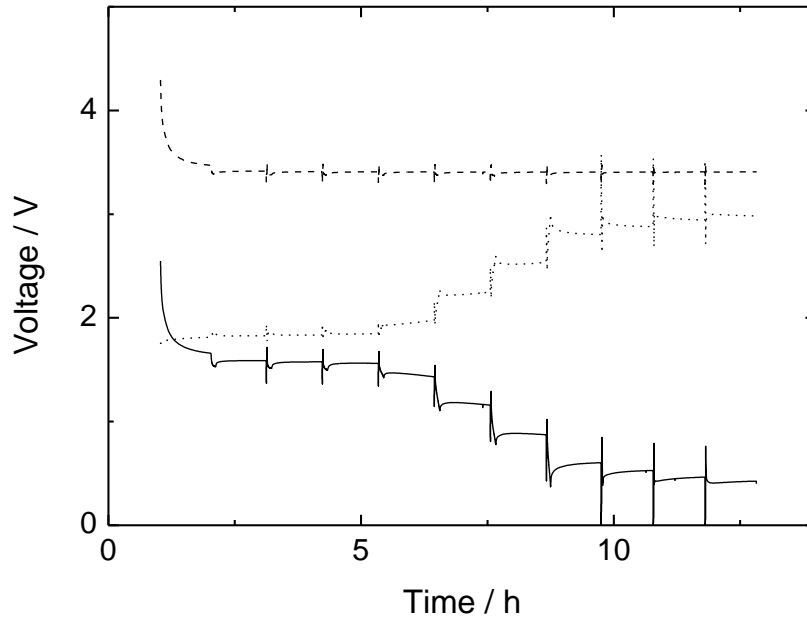


Figure 6.24. Voltage profile of the HPPC at 5C performed on the battery. (—) Battery voltage, (---) cathode and (···) anode voltages.

Table 6.10. Results of HPPC test.

DOD	V₀	V₁	V₂	V₃	R_{disc}	R_{regen}	R_{disc}	R_{regen}	P_{disc}	P_{regen}
%	V	V	V	V	ohm	ohm	ohm cm²	ohm cm²	W kg⁻¹ battery	W kg⁻¹ battery
10	1.587	1.37	1.544	1.714	140	146	84	88	491	731
20	1.575	1.363	1.533	1.696	137	140	82	84	492	781
30	1.561	1.344	1.509	1.675	140	143	84	86	469	806
40	1.431	1.145	1.315	1.541	185	195	111	117	273	826

6.1.6 Li₄Ti₅O₁₂/ PYR₁₄TFSI-EC DMC LiPF₆ 50:50w/ LiFePO₄-C

The battery was composed by LiFePO₄-C cathode, anode Li₄Ti₅O₁₂ and PYR₁₄TFSI-EC DMC LiPF₆ 50:50 mixture electrolyte. The electrodes were balanced. The electrodes area was 0.6 cm². In this case, the electrodes were not pre-cycled given that the irreversible capacity in the first cycle is very similar for Li₄Ti₅O₁₂ and LiFePO₄, thus, the battery had only one separator (Durieux). Electrodes characteristics and testing conditions are reported in Table 6.11.

Table 6.11. Battery electrodes characteristics and testing conditions.

Electrode	Material	Active material	Binder	Conductive carbon	Composite	Battery tests	Currents	Electrolyte	T
		mg	mg	mg	mg		mA		°C
Anode ⁺	Li ₄ Ti ₅ O ₁₂	1.37 (76%)	0.21** (12%)	0.21 (12%)	1.79	SCT 1C; HPPC	0.15; 1.26	PYR ₁₄ TFSI- EC DMC LiPF ₆ 50:50	30
Cathode	LiFePO ₄ -C	1.49 (74.6%)	0.10* (5%)	0.40 (20.4%)	1.99	5C			

⁺ Pressed, *Teflon; **PVDF

The battery was first cycled by deep galvanostatic charge/discharge cycles at 1C for 9 cycles at 30°C (Figure 6.25).

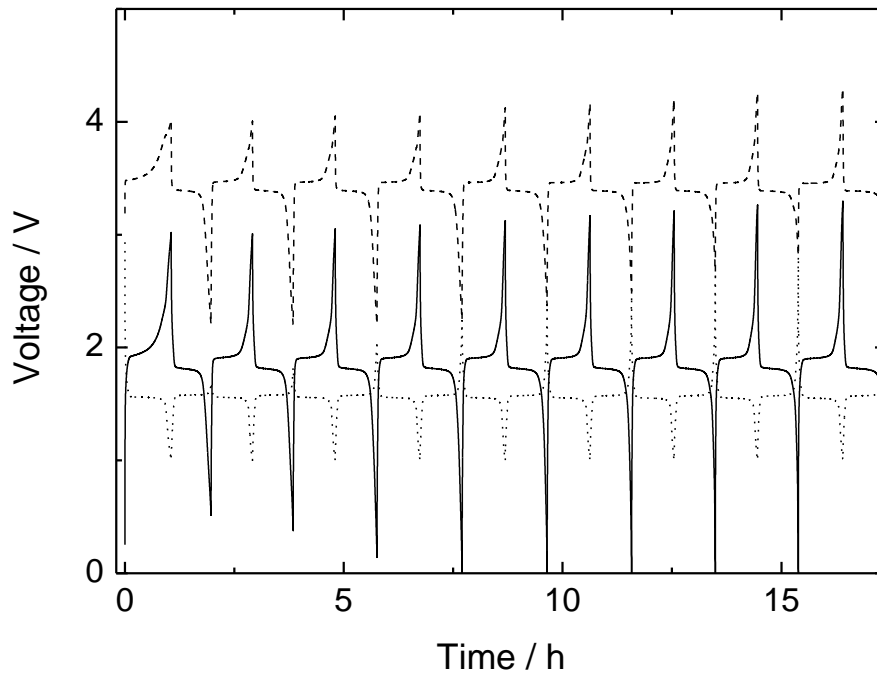


Figure 6.25. Voltage profile of the first galvanostatic cycles at 1C performed on the battery. (—) Battery voltage, (---) cathode and (···) anode voltages.

The FreedomCAR HPPC test of the lithium-ion battery we assembled were performed by setting battery V_{\max} at 2.13 V and V_{\min} at 1.3 V. The 1C discharges used for SCT and HPPC tests were effective, i.e. the battery was discharged in one hour, while 5C rate used in the pulses of HPPC test referred to theoretic capacity of the cathode. All the test were performed at 30°C. Figure 6.26 shows, according to SCT test, the plots of the battery discharge voltage and of the specific cumulative energy removed during discharge (E_{DOD}) vs. DOD at 1 C-rate and 30°C. The battery voltage profile during the HPPC test is shown in figure 6.27; and the calculated pulse resistance and power are reported in Table 6.12. The discharge power capability vs. energy plot, compared with the HEV pulse power target ($625 \text{ W kg}^{-1}_{\text{battery}}$ for discharge and 500 W kg^{-1} for charge), is shown in Figure 6.28, and indicates that the $\text{Li}_4\text{Ti}_5\text{O}_{12}/\text{PYR}_{14}\text{TFSI-EC DMC LiPF}_6 \text{ 50:50/LiFePO}_4\text{-C}$ lithium-ion battery surpasses the pulse power goal, in particular in the range 10% - 61% DOD: this is the state of charge in which have to be maintained the battery during the utilization in power-assist mode in HEV. Moreover, the figure 6.29 shown the corresponding available energy calculated at such DOD (as stated in the DOE protocol) that is $18 \text{ Wh kg}^{-1}_{\text{battery}}$, above the DOE target (7.5 Wh kg^{-1}). In conclusion, this battery surpasses the DOE goal for power-assist HEV application. In particular, resistance values were very lower than

previous Ti-based anode cells, thanks to the use of a pressed anode electrode and only one separator.

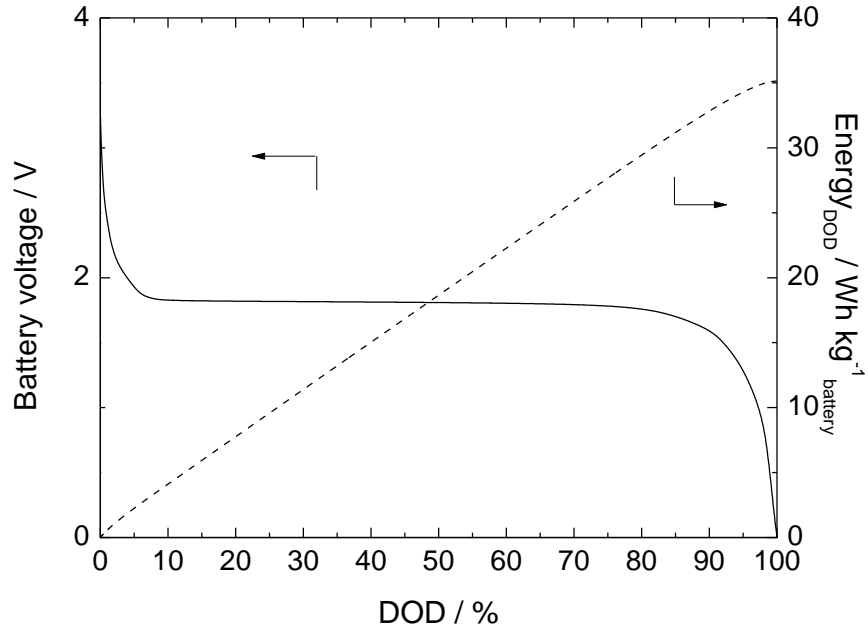


Figure 6.26. Static capacity test (SCT) performed at 1 C-rate and 30°C on the battery. Dashed line is the relationship between cumulative energy and DOD.

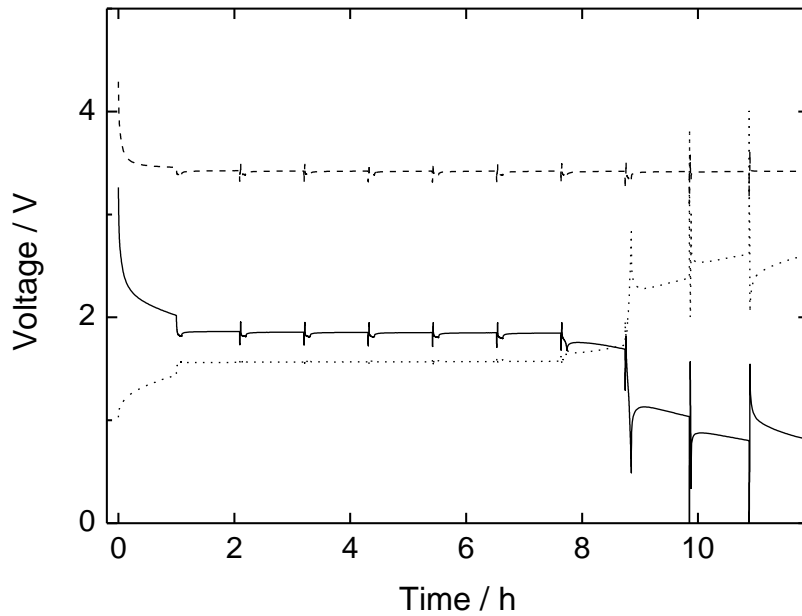


Figure 6.27. Voltage profile of the HPPC test at 5C performed on the battery. (—) Battery voltage, (---) cathode and (···) anode voltages.

Table 6.12. Results of HPPC test.

DOD	V ₀	V ₁	V ₂	V ₃	R _{disc}	R _{regen}	R _{disc}	R _{regen}	P _{disc}	P _{regen}
%	V	V	V	V	ohm	ohm	ohm cm ²	ohm cm ²	W kg ⁻¹ battery	W kg ⁻¹ battery
10	1.862	1.735	1.844	1.954	107	123	64	74	908	656
20	1.857	1.73	1.842	1.95	107	121	64	73	900	673
30	1.854	1.725	1.84	1.948	108	121	65	73	881	677
40	1.852	1.718	1.838	1.948	113	123	68	74	845	670
50	1.85	1.707	1.835	1.949	120	128	72	77	789	653
60	1.847	1.682	1.825	1.949	139	139	83	83	680	620
70	1.69	1.293	1.53	1.817	334	321	200	193	202	527

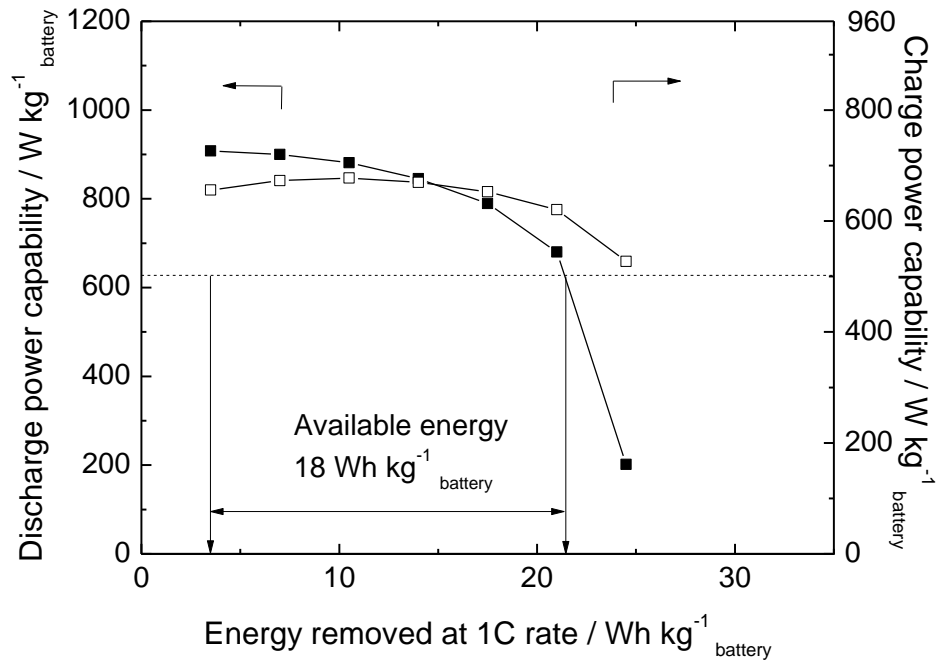


Figure 6.28. Discharge power capability vs. energy removed at 1C rate of cycled battery from HPPC 5C test.

The dashed line refers to HEV pulse power target.

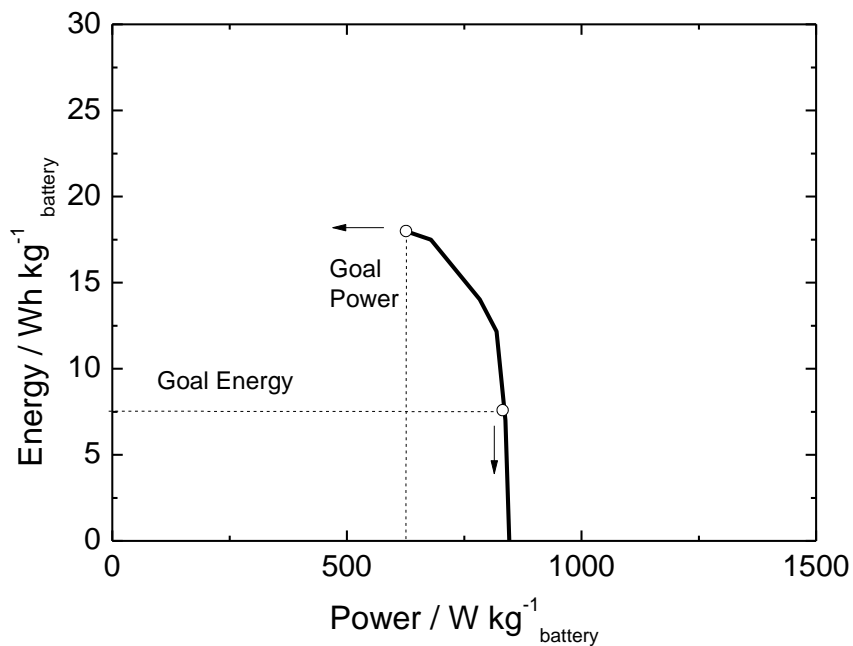


Figure 6.29 Usable energy as a function of discharge pulse-power for the battery.

Unfortunately, after the FreedomCAR tests, the battery underwent severe capacity fade and was not possible to repeat the tests on cycled cell. The problem was probably the $\text{Li}_4\text{Ti}_5\text{O}_{12}$ anode that showed the rise of an irreversible capacity, not present in the first cycles, that is also visible at the end of the HPPC test where the anode voltage rose prematurely after 60% DOD. However, this battery demonstrated that is possible to satisfy the DOE targets for HEV application using $\text{Li}_4\text{Ti}_5\text{O}_{12}$ and $\text{LiFePO}_4\text{-C}$ electrodes and $\text{PYR}_{14}\text{TFSI-EC DMC LiPF}_6$ 50:50 electrolyte, with a lot of margin in terms of available energy that, in presence of a optimized anode and electrolyte, would satisfy the targets even after long cycling.

6.2 Lithium battery for application in EV

6.2.1 Li/PEO₂₀-LiCF₃SO₃ + 10%ZrO₂/LiFePO₄/C lithium polymer battery

The battery was composed by LiFePO₄-C cathode, lithium metal anode in excess and PEO₂₀-LiCF₃SO₃+10%ZrO₂ polymeric electrolyte. The geometric electrode area was 0.384 cm². Cathode characteristics and battery testing conditions are shown in Table 6.13.

Table 6.13. Cathode characteristics and testing conditions.

Electrode	Material	Active material	Binder (Teflon)	Conductive carbon	Composite	Battery test	Currents	Electrolyte	T
		mg	mg	mg	mg		mA		°C
Cathode	LiFePO ₄ -C	1.06 (74.6%)	0.07 (5%)	0.30 (20.4%)	1.43	CCDT C/3; PPT 1C, 2C	0.044; 0.130, 0.260	PEO ₂₀ - LiCF ₃ SO ₃ + 10%ZrO ₂	100

All the tests were performed by setting a cut-off voltage of 4.0 V for the charge and of 2.2 V for the discharge. The currents for the C-rates ranging from 2C to C/10 varied from 0.677 to 0.034 mA cm⁻². Specific lithium polymer battery (LPB) parameters like energy and power were evaluated in reference to both electrode mass of 4.1 mg cm⁻², which is the sum of the cathode electrode composite mass and three times the stoichiometric amount of lithium as anode. Figure 6.30 shows the voltage profiles of the constant current discharge tests (CCDT) at different C-rates. The discharge curves of three successive charge/discharge cycles at C/3, shown in Figure 6.31, which delivered constant capacity values within 2% (123 ± 1 Ah kg⁻¹ LiFePO₄), were used to calculate specific energy of the LPB of 275 Wh kg⁻¹_{battery}.

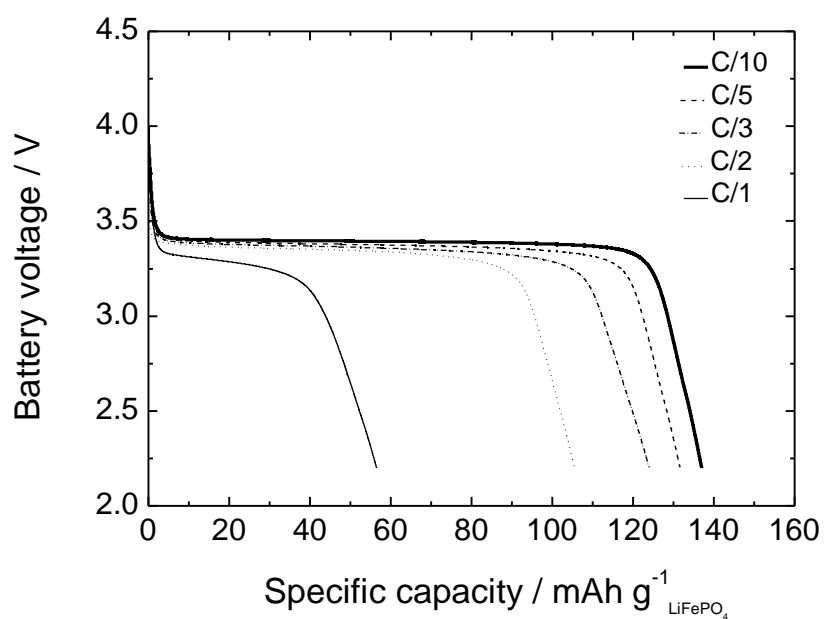


Figure 6.30. Discharge profiles of the Li/PEO₂₀-LiCF₃SO₃+10%ZrO₂/LiFePO₄-C LPB at different C-rates. Cut-off 4.0–2.2 V. 100°C.

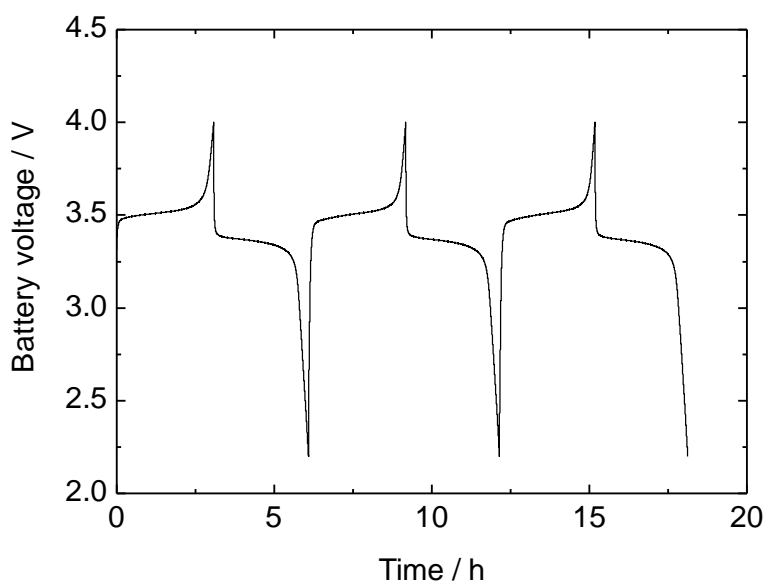


Figure 6.31. Voltage profiles of three subsequent charge/discharge cycles at C/3 at 100°C of the LPB battery.

The PPTs were performed, starting from a fully charged LPB at $C/3$ at 10 depths of discharge ranging from 0% DOD to 90% DOD in 10% intervals in the course of a single discharge at a $C/3$ rate. At each DOD the LPB was discharged by a 30 s current pulse, and the pulse currents corresponded to $1C$ for the low-current and to $2C$ for the high-current tests; maximum pulse C-rate of $2C$ was selected to avoid lithium diffusion limitation in the thick PEO separator. It is worth noting here that, before applying the first (0% DOD) discharge pulse, the LPB was discharged for 30 s at the base discharge rate ($C/3$) and that after the last current pulse at 90% DOD the cell was discharged at $C/3$ to 100% of its rated capacity. Figures 6.32 and 6.33, which show the voltage profiles of low and high-current PPTs performed on a fresh LPB, clearly demonstrate that in both tests the battery always remained above the discharge voltage limit of 2.2 V.

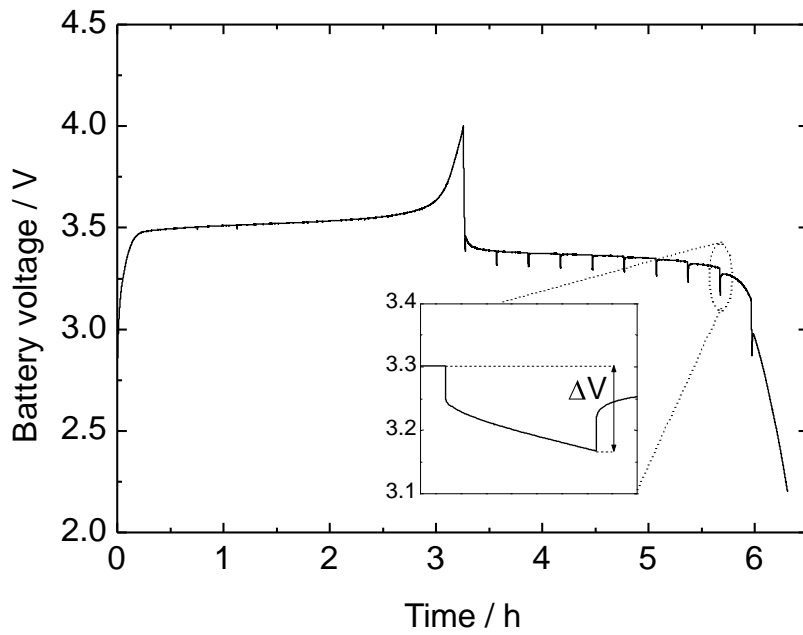


Figure 6.32. Voltage profile of fresh LPB battery under the low-current ($1C$ pulse) PPT at 100°C . The inset shows the pulse voltage profile at 80% DOD.

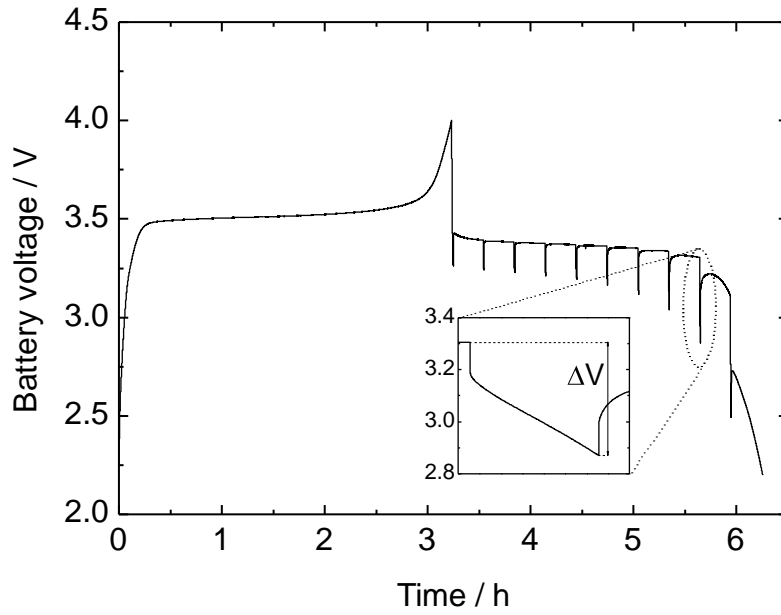


Figure 6.33. Voltage profile of fresh LPB battery under the high-current (2C pulse) PPT at 100°C. The inset shows the pulse voltage profile at 80% DOD.

The peak power capability of this LPB was calculated at each DOD by deriving the battery resistance and equivalent IR-free voltage from measured changes in battery voltage and current. The voltage values for ΔV calculations were measured just prior to (V_1) and then near the end (V_2) of each pulse discharge current step. The ΔI current values were taken either as the difference between the base current at C/3 and the pulse current at 1C for the low-current test, or as the pulse current at 2C for the high-current tests. Accordingly, cell resistance R and the IR-free voltage were computed as

$$\text{battery resistance : } R = \Delta V / \Delta I \quad (1)$$

$$\text{cell IR-free voltage (before the pulse) : } V_{\text{IRFree}} = V - IR \quad (2)$$

The peak power capability was calculated by Eq. (3) as:

$$\text{peak power capability} = I_{\text{Pulse}} \cdot (V_{\text{IRFree}} + RI_{\text{Pulse}}) \quad (3)$$

As suggested in the manual, this equation was selected because it yields the lowest value of peak power capability at 80% DOD. The low- and high-pulse current tests were performed

twice on the same fresh battery and the results were highly reproducible. Table 6.14 displays (first two rows) the results of the low and high PPTs at 80% DOD for V1 and V2 voltage, resistance, IR-free voltage and peak power values; Table 6.15 (first column) shows the specific power from high-current PPT and the specific energy from the Constant Current Discharge test at C/3. The comparison of the specific power and energy of the LPB with the USABC-DOE EV minimum and long-term targets reported in the last two columns of Table 6.15 demonstrates that the Li/PEO₂₀-LiCF₃SO₃+10%ZrO₂/LiFePO₄-C battery surpasses these targets. In calculating the specific values of this LPB, the weight of the current collector and of the polymer separator were not included because they were not optimized as in a commercial battery^{6,2}. However, even assuming a total battery weight twice that of the electrode materials, this LPB technology appears capable of approaching USABC targets.

Table 6.14. PPT results at 100°C and 80% DOD for fresh and cycled LPB battery.

	V ₁	V ₂	Resistance	IR-free voltage	Peak Power
	V	V	ohm cm ²	(V)	(mW)
Low-current pulse test (1C), fresh cell	3.30	3.17	572	3.24	0.45
High-current pulse test (2C), fresh cell	3.31	2.90	702	3.24	0.97
High-current pulse test (2C), cycled cell	3.30	2.85	864	3.22	0.86

Table 6.15. Specific power and specific energy of fresh and cycled LPB battery the targets set by the USABC-DOE for EV application.

	fresh cell	cycled cell	USABC minimum goal	USABC long term goal
Specific Power – Discharge, 80% DOD/30s (W kg ⁻¹)	615	550	300	400
Specific Energy – C/3 discharge rate (Wh kg ⁻¹)	275	240	150	200

This LPB was then galvanostatically cycled at C/3 and 100°C for more than 375 deep cycles and Figure 6.34, which displays the delivered capacity over cycles, shows the electrochemical stability of this LPB as well as its mechanical stability over more than 3 months at 100°C. Cell response under thermal interruption was also investigated. The test was run by lowering temperature from 100°C to room temperature in the course of the 200th cycle and the LPB was cycled for 300 cycles at the same current and voltage cut-off used for the tests at 100°C. Thereafter the temperature was raised again to 100°C and the galvanostatic cycling at C/3 was restarted: no capacity loss was observed, as shown in Figure 6.34, and this clearly demonstrates the mechanical stability of the battery. Battery performance in terms of specific energy and power after 375 deep cycles at 100°C was evaluated by constant current discharge test at C/3 and high-current PPT at 2C. The results of the PPT on this cycled cell are in the last row of Table 6.14 and the specific power and energy values are reported in the second column of Table 6.15. A comparison of the specific values of the cycled cell with those of the fresh battery shows that the decay is ca. 10%, clearly indicating that the DOE targets are still met even by this long-cycled LPB.

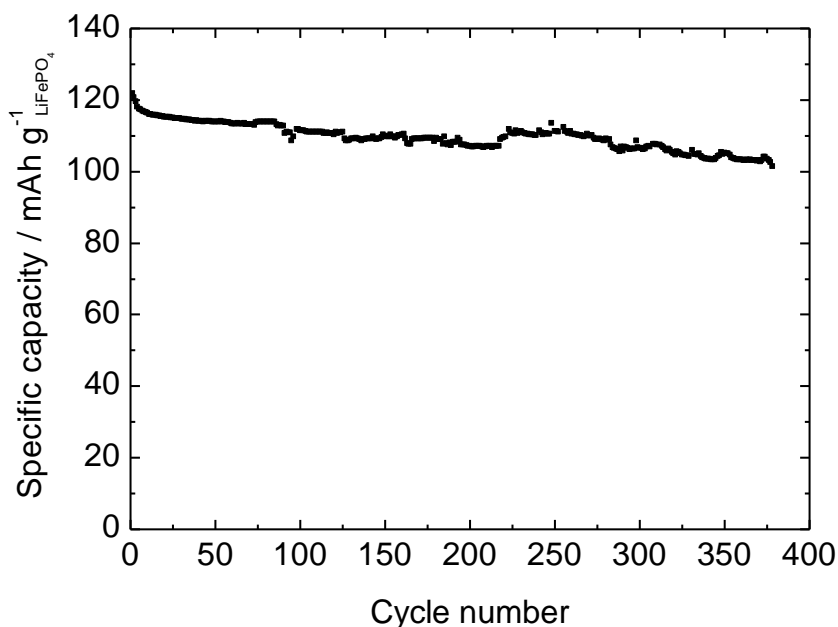


Figure 6.34. Delivered specific discharge capacity at C/3 and 100°C by LPB battery vs. cycle number.

6.3 Conclusions

Different types of battery were assembled and studied. As concerns lithium-ion batteries, graphite/EC DMC-LiPF₆/LiFePO₄-C and graphite/PYR₁₄TFSI 0.4m LiTFSI with 10% VC/LiFePO₄-C batteries were able to surpass the DOE targets for application in power-assist HEV at the beginning of life and even after long cycling. Li₄Ti₅O₁₂/PYR₁₄TFSI-EC DMC LiPF₆ 50:50w/ LiFePO₄-C battery surpassed DOE targets only at the beginning of life because of some problems related to anode in 50:50 electrolyte. Finally, as concern lithium battery, Li/PEO₂₀-LiCF₃SO₃ + 10%ZrO₂/LiFePO₄-C lithium polymer battery demonstrated to surpass the DOE targets for EV application even after 275 deep charge/discharge cycles.

6.4 References

- 6.1) P. Albertus, J. Coutts, V. Srinivasan, J. Newman, Journal of Power Sources 183 (2008) 771–782
- 6.2) R.C. Agrawal, G.P. Pandey, J. Phys. D: Appl. Phys. 41 (2008) 223001.

Chapter 7

Conclusions

This thesis work, starting from the characterization of single electrode materials vs. lithium in different electrolytes and concluding with battery tests following USA DOE protocol for HEV and EV application, demonstrated that batteries with safe electrode materials and electrolytes are capable to satisfy the targets for automotive applications.

Given that the electrolyte is the main critical point of a battery, in particular in large-format modules, we studied an innovative electrolyte based on ionic liquid (PYR₁₄TFSI with 0.4 m LiTFSI) that is characterized by high boiling/decomposition points, thermal and electrochemical stability, appreciable conductivity above RT: this unique combination of favorable properties make this ionic liquid very appealing as stable and safe electrolyte media in lithium-ion batteries. Moreover, recent studies highlight that even mixtures of ionic liquid and conventional electrolyte lead to high conductivity and low flammability electrolytes, hence, PYR₁₄TFSI/EC DMC-LiPF₆ 50%/50 wt.% mixture was also used.

In this PhD research work much effort was focused on the development and characterization of electrode materials in view of the application in complete lithium-ion and lithium batteries. In particular, carbon-coated lithium iron phosphate (LiFePO₄-C) was select as cathode material because is the most promising one for safe, non-toxic, thermally stable, high power batteries. LiFePO₄-C of high purity grade was successfully synthesized by microwave accelerated sol-gel synthesis and showed excellent electrochemical performance in terms of specific capacity and stability.

Among anode materials, graphite was characterized since is the most used active material for the anode production, due to its unique characteristics in terms of capacity, cyclability, low voltage of the lithium insertion/deinsertion process and cheapness; alternative safer materials based on titanium oxides (TiO₂ and Li₄Ti₅O₁₂) were also characterized, in particular in ionic liquid based electrolytes, due to fact that they do not show problems related to SEI formation. Tin-based high-capacity electrodes, derived from an array of amorphous SnCo nanowires fabricated by template electrodeposition in polycarbonate membrane template, yielded electrodes capable of reversibly intercalating lithium for 35 cycles with an elevated capacity per cm².

Finally, different battery types, based on LiFePO₄-C, graphite and titanium-based electrode materials, and conventional and innovative electrolytes, were assembled and characterized by benchmark tests for HEV application. As concerns lithium-ion batteries, graphite/ LiFePO₄-C battery surpassed the DOE target for application in power-assist HEV and it worth noting that this is the first time that practical data (not simulated) of the dynamic functioning of this lithium-ion battery are reported. Graphite/LiFePO₄-C battery with the innovative electrolyte PYR₁₄TFSI 0.4m LiTFSI with 10% vinylene carbonate additive, added as SEI-forming component, was also able to surpass the HEV targets at the beginning of life and even after long cycling. Dealing with batteries with titanium-based anodes in IL based electrolytes, Li₄Ti₅O₁₂/ PYR₁₄TFSI-EC DMC LiPF₆ 50:50w/ LiFePO₄-C battery met DOE targets at the beginning of life. Li/ LiFePO₄-C lithium battery with polymer electrolyte PEO₂₀-LiCF₃SO₃+10%ZrO₂ was also assembled and characterized by specific tests for EV and demonstrated to surpass the DOE targets for this application even after 275 deep charge/discharge cycles.

Further improvement of these lithium-ion batteries based on safe components may be achieved by optimizing electrode composition by lowering binder and conductive carbon amount and pressing the electrodes. Hence, the use of optimized electrodes and battery geometry will lead to batteries with even higher performance.

Acknowledgements

First of all, I wish to thank my supervisor, Prof. Marina Mastragostino for the opportunity of pursuing PhD studies and for her scientific support during this thesis project. I also wish to acknowledge all my colleagues of the Laboratorio di Elettrochimica dei Materiali (LEM) of the University of Bologna for their friendship.

Finally, I acknowledge the financial support provided by the MIUR (Italy) PRIN 2007 Project “Lithium ironphosphate as cathode material for lithium-ion batteries for HEV and for charge storage from renewable intermittent sources”. In particular, I wish to thank Prof. Bruno Scrosati’s, Prof. Roberto Marassi’s and Prof. Carmelo Sunseri’s groups for the fruitful discussions and collaborations.

List of Presentation to Conferences

All solid-state rechargeable Li/LiFePO₄ polymer battery for electric vehicle application

L. Damen, J. Hassoun, M. Mastragostino, B. Scrosati

The 15th International Meeting on Lithium Batteries IMLB 27/06-2/07/2010 (Montreal, Canada)

SnCo nanowire-based anodes for lithium-ion batteries

C. Arbizzani, L. Damen, G. Ferrara, R. Inguanta, S. Piazza, C. Sunseri, M. Mastragostino

GEI- ERA 2010 Giornate dell'Elettrochimica Italiana (Modena, Italy, 5-10 Sept. 2010)

Lithium and lithium-ion batteries for automotive applications

L. Damen and M. Mastragostino

GEI- ERA 2010 Giornate dell'Elettrochimica Italiana (Modena, Italy 5-10 Sept. 2010)

Template electrosynthesis of SnCo nanowire arrays for lithium-ion batteries

G. Ferrara, L. Damen, C. Arbizzani, R. Inguanta, S. Piazza, C. Sunseri, M. Mastragostino

The 61st Annual Meeting of the International Society of electrochemistry 26/09-01/10/2010, Nice (France)

Fast synthesized LiFePO₄/C cathode material for high power application in lithium-ion batteries for HEV

C. Arbizzani, S. Beninati, L. Damen, M. Mastragostino

216th Meeting of the Electrochemical Society (Vienna, Austria, 4-9/10/09)

Batteries and supercapacitors for renewable energy plants and sustainable transportation

M. Mastragostino, C. Arbizzani, S. Beninati, L. Damen, M. Lazzari, F. Soavi

XXIII Congresso Nazionale della Società Chimica Italiana (Sorrento, Italy, 5-10/07/09)

List of Publications

Fast sol–gel synthesis of LiFePO_4/C for high power lithium-ion batteries for hybrid electric vehicle application

S. Beninati, L. Damen, M. Mastragostino,

Journal of Power Sources, 194 (2009) 1094-1098

Solid-state, rechargeable $\text{Li}/\text{LiFePO}_4$ polymer battery for electric vehicle application

L. Damen, J. Hassoun, M. Mastragostino, B. Scrosati,

Journal of Power Sources 195 (2010) 6902–6904

SnCo nanowire array as negative electrode for lithium-ion batteries

G. Ferrara, L. Damen, C. Arbizzani, R. Inguanta, S. Piazza, C. Sunseri, M. Mastragostino,

Journal of Power Sources 196 (2011) 1469–1473

Nanostructured anode material for Li-ion batteries

G. Ferrara, L. Damen, C. Arbizzani, R. Inguanta, S. Piazza, C. Sunseri, M. Mastragostino

Advances in Science and Technology Vol. 72 (2010) 320-324 [ISSN 1662-0356]

